

INAUGURAL-DISSERTATION
zur
Erlangung der Doktorwürde
der
Naturwissenschaftlich-Mathematischen Gesamtfakultät
der
Ruprecht-Karls-Universität Heidelberg

vorgelegt von
Yifan Yang
aus Dujiangyan, China

Tag der mündlichen Prüfung:

Mathematical Modeling and Simulation of the Evolution of Plaques in Blood Vessels

Gutachter: Prof. Dr. Dr. h. c. mult. Willi Jäger

Gutachter:

Abstract

The formation of plaques is one of the main causes for the blockage of arteries. This can lead to ischaemic brain or myocardial infarctions as well as other cardiovascular diseases. Possible biochemical and biomechanical processes contribute to the development of plaque growth and rupture. The main biochemical processes are the penetration of monocytes and the accumulation of foam cells in the vessel wall, leading to the formation and growth of plaques. The biomechanical forces can be measured by observing stresses in the blood flow and the vessel wall, which may lead to the rupture of plaques.

In this thesis, we formulate an appropriate model to describe the evolution of plaques. The model consists of both the interaction between the blood flow and the vessel wall, and the growth of plaques due to the penetration of monocytes from the blood flow into the vessel wall. The Navier-Stokes equations and the elastic structure equations are used to describe the dynamics of fluid (blood flow) and the mechanics of structure (vessel wall). The motion of monocytes is described by the convection-diffusion-reaction equation, coupled with an equation for the accumulation of foam cells. Finally the metric of growth is introduced to accurately determine the stress tensor, and its evolution equation is derived. The variational formulation of the model is transformed into the ALE (Arbitrary Lagrangian-Eulerian) formulation, and all the equations are rewritten in the fixed domain. Temporal discretization is achieved with finite differences and spatial discretization is based on the Galerkin finite element method. The nonlinear systems are linearized and solved by the Newton method.

Based on the model and the numerical methods above, numerical simulations are performed by using the software Gascoigne. The obtained numerical results make an agreement with the observation, and support the assumption that the penetration of monocytes and the accumulation of foam cells lead to the formation and growth of plaques, and that the evolution of plaques induces the increase of stresses in the vessel wall, which is an indicator of plaque rupture.

Zusammenfassung

Die Entwicklung von Plaques ist eine Hauptursache für die Verstopfung von Schlagadern. Sie kann zu ischämischen Schlaganfällen oder Herzinfarkten sowie zu anderen kardiovaskulären Erkrankungen führen. Mögliche biochemische und biomechanische Prozesse tragen zur Entwicklung von Wachstum und Bruch der Plaques bei. Die wichtigsten biochemischen Prozesse, welche zur Bildung und zum Wachstum von Plaques führen, sind das Eindringen von Monozyten und die Akkumulation von Schaumzellen in die Gefäßwand. Die biomechanischen Kräfte können durch die Beobachtung von Spannungen der Blutströmung und der Gefäßwand bestimmt werden und können zum Bruch von Plaques führen.

In dieser Arbeit formulieren wir ein geeignetes Modell zur Beschreibung der Entwicklung von Plaques. Das Modell besteht sowohl aus der Interaktion zwischen dem Blutstrom und der Gefäßwand, als auch dem Wachstum von Plaques durch das Eindringen von Monozyten aus dem Blutstrom in die Gefäßwand. Die Navier-Stokes Gleichungen und die elastische Strukturgleichungen werden zur Beschreibung der Dynamik der Flüssigkeit (Blut) und der Mechanik der Struktur (Gefäßwand) verwendet. Die Bewegung der Monozyten wird durch eine Konvektions-Diffusions-Reaktionsgleichung, zusammen mit einer Gleichung zur Beschreibung der Akkumulation von Schaumzellen beschrieben. Schließlich wird eine Wachstumsmetrik eingeführt, um den Spannungstensor richtig bestimmen zu können, und die Gleichung ihrer Entwicklung wird abgeleitet. Die variationelle Formulierung des Modells wird hierfür in ALE-Form (Arbitrary Lagrangian-Eulerian) umgewandelt, so dass alle Gleichungen auf festen Gebieten gegeben sind. Die zeitliche Diskretisierung erfolgt mit Finiten Differenzen, und die räumliche Diskretisierung basiert auf der Galerkin Finite Elemente Methode. Die nicht-linearen Systeme müssen linearisiert und mit Hilfe des Newton-Verfahrens gelöst werden.

Basierend auf diesem Modell und den numerischen Methoden werden numerische Simulationen mit der Software Gascoigne durchgeführt. Die erzielten numerischen Ergebnisse stimmen gut mit den Beobachtungen überein. Sie unterstützen die Vermutung, dass das Eindringen von Monozyten und die Akkumulation von Schaumzellen zur Bildung und zum Wachstum von Plaques führen, und dass die Entwicklung von Plaques zu einer Zunahme

von Spannungen in der Gefäßwand führt. Diese Zunahme von Spannungen kann als Indikator für den Bruch von Plaques dienen.

Contents

Introduction	1
1 Biological Background	5
1.1 Inducing factors of atherosclerosis	5
1.2 Evolution of the rupture-prone atherosclerotic plaque	7
1.3 Main components of a plaque	8
1.4 Plaque rupture and thrombotic response	10
2 Mathematical Model	13
2.1 Overview of existing results	14
2.2 Processes to be modeled	15
2.3 Kinematics of continuum media	18
2.4 Fluid dynamics	22
2.4.1 Conservation equations	22
2.4.2 Incompressible flows	24
2.5 Structural mechanics	27
2.5.1 Conservation equations with growth function	27
2.5.2 Piola transformation	28
2.6 Chemical processes	33
2.6.1 Convection-diffusion equation	33
2.6.2 Convection-diffusion-reaction equation	35
2.7 Stress tensor modeling	38
2.7.1 Decomposition of deformation gradient	38
2.7.2 Metric of growth	41
2.7.3 Constitutive equations	43
2.8 Final model	51
3 Variational Formulation	57
3.1 General variational formulation	58
3.2 Variational formulation in the ALE framework	63
3.2.1 ALE formulation in the fluid domain	63

3.2.2	Construction of the ALE mapping	69
3.2.3	Final ALE formulation	72
3.3	Theoretical results	76
4	Numerical Simulation	87
4.1	Numerical methods	88
4.1.1	Temporal discretization	88
4.1.2	Spatial discretization	89
4.1.3	Linearization	92
4.1.4	Introduction of Gascoigne	93
4.2	Numerical results	94
4.2.1	Example I	95
4.2.2	Example II	111
5	Conclusions and outlook	125
	Acknowledgments	129
	List of Figures	131
	List of Tables	133
	Bibliography	135

Introduction

The topic of this thesis is related to the study of the vascular disease atherosclerosis, which is one of the main causes of ischaemic brain infarction, and is associated with the formation and rupture of plaques. Atherosclerosis without thrombosis is generally a benign disease. However, it is plaque rupture with superimposed thrombus that may turn a stable disease to a life-threatening condition and induce the blockage of a main artery, which can lead to ischaemic brain or myocardial infarctions as well as other cardiovascular diseases^[15;42;52]; on the other hand, plaque rupture can also let some material of thrombus be taken away by the blood flow, and may induce the blockage in another part of the artery, turning a local problem to a global one. Possible contributors to the development of atherosclerosis can be categorized as either biochemical or biomechanical^[73]. The main biochemical processes associated with atherosclerosis start with the penetration of monocytes from the blood flow into the vessel wall. Through several chemical reactions, monocytes are converted to foam cells and accumulate in the vessel wall, leading to the formation and growth of plaques. Plaques are formed primarily in the innermost layer of the vessel wall called the intima, while the other two layers are called the media and adventitia. The biomechanical forces can be measured by observing stresses in the blood flow and the vessel wall. The growth of plaques induces the increase of stresses applied on them and can possibly cause them to rupture.

Concerning different processes of atherosclerosis, different mathematical models have been developed. Some previous mathematical models concentrate alternatively on biochemical processes^[2;13;31;41;43] or biomechanics^[67-70;82]. In these models the plaque growth is not considered, so the interface between the blood flow and the vessel wall is normally in a fixed state. The free boundary problem is also used in some similar problems, e.g. the modeling of thrombus formation^[74], but this model only considers the fluid dynamics of the blood flow without the structural mechanics of the vessel wall. In our model, we consider both the biochemical reactions leading to plaque growth,

and the interaction between the blood flow and the vessel wall with a free interface.

The main goal of this thesis is to derive a model to describe how plaques are formed and growing in healthy tissue due to the biochemical reactions related to monocytes and foam cells, and also how stresses are distributed in the long-term evolution of plaques, which may lead to plaque rupture. The processes requiring investigation and modeling are:

- The adhesion and penetration of monocytes from the blood flow into the vessel wall
- The accumulation of foam cells in the vessel wall, leading to plaque growth
- Changing of the mechanical properties of the vessel wall due to the influence of foam cells
- The interaction between the blood flow and the vessel wall

The domain we are considering consists of two parts: a fluid part representing the part occupied by the blood flow, and a solid part representing the part occupied by the vessel wall. The interface between the fluid and solid part moves according to the plaque growth and the fluid-structure interaction. The Navier-Stokes equations are used to describe the dynamics of fluid (blood flow) whereas in the solid part (vessel wall) the equations for structural mechanics are considered. In addition, the motion of monocytes is described by the convection-diffusion-reaction equation, coupled with an equation for the accumulation of foam cells. The transmission conditions are also given on the interface.

There is a problem, however, which is that the deformation in the solid part is induced by both mechanics and the growth of plaques, so one cannot use the general approach to derive the stress tensor in the equations for structural mechanics. To overcome this problem, we introduce a new variable called the metric of growth. Given that the growth not only increases the mass but also changes the geometry, the metric of growth is used to define the deformation induced only by mechanics, and also to accurately measure the stress tensor with the constitutive equations^[11]. For the constitutive equations, two models are taken into account: the incompressible Neo-Hookean(INH), and the incompressible Mooney-Rivlin material laws^[25]. In addition, the concentration of foam cells is also related to the growth modeling of the solid part by

influencing the mechanical properties.

Here follows an introduction of the numerical approaches of our model in detail. Similar to the general fluid-structure interaction problem, the variational formulation of our model is formulated in a monolithic framework, where the coupled equations in the fluid and solid domains are solved simultaneously^[53;78]. Typically, the variational form in the fluid domain is formulated in the Eulerian framework, where the domain is movable due to the movement of the interface, and the form in the solid domain is given in the Lagrangian framework, where the domain is fixed. For numerical simulations we need different meshes in different subdomains and as well as in different time steps. To treat this problem we employ the Arbitrary Lagrangian-Eulerian (ALE) framework, which is a well-known monolithic approach for fluid-structure interaction problem. In this method, the fluid domain is transformed to a fixed one by the ALE mapping, and all the equations are rewritten in the fixed domain. Different mesh models are used to define the ALE mapping. The main advantage of the ALE method is that both of the subdomains are fixed in the ALE framework, so a common mesh can be used for the problem in numerical simulations in each time step. The energy estimate of the model is also investigated to obtain numerical stability. The main numerical methods we use in this thesis are the finite difference method for temporal discretization, the Galerkin finite element method for spatial discretization and the Newton method for linearization.

Numerical simulations are performed by using the finite element library Gascoigne, and numerical results are presented in two examples. Example I is a test case to show whether the behavior of plaque formation can be well observed, and has a simple configuration. Example II has a configuration which is much closer to a real artery, from which the model can provide a more realistic description of plaque formation. Both examples are in two-dimensional space, and all the parameters are from the literature in the fields of medicine, biodynamics and cardiovascular mathematics^[4;20;36;48;60;70;86]. In numerical simulations, we perform the steps listed below:

- Different time step sizes and mesh refinement levels are tried to investigate the convergence of numerical solutions.
- Some special techniques, e.g. the local mesh refinement and adding artificial stabilization terms, are also tested to reveal their necessity.
- Numerical results in both of these two examples represent the motion of the interface and the distributions of important quantities in the model

at different time points to show the evolution of the whole process.

The obtained results show the formation and growth of plaques, the penetration of monocytes, the accumulation of foam cells, the increase of stresses and their interactions, which is the starting point of this problem^[84;85]. Many interesting questions are still open in numerical, theoretical and modeling fields, and both the modeling and simulation approaches obtained in this thesis can be improved not only to bring the model closer to the reality of plaque formation, but also to apply it to other investigations related to the interaction of reactive flow with solid phase^[83].

Outline of this thesis

- Chapter 1 provides the biological background about the whole physiological process, including the inducing factors of plaque formation, the key steps of plaque evolution, the main components a mature plaque, and the thrombotic response to plaque rupture.
- In Chapter 2 we give a review of some existing mathematical models related to plaques, determine the processes we are interested in modeling, and derive the model step by step with a complicated system.
- In Chapter 3 the variational formulation of the model is given and the ALE framework is used to overcome numerical difficulties.
- Chapter 4 lists the numerical methods we use and presents the numerical results we obtain.
- In Chapter 5 we summarize the conclusions and provide an outlook for future development.

Chapter 1

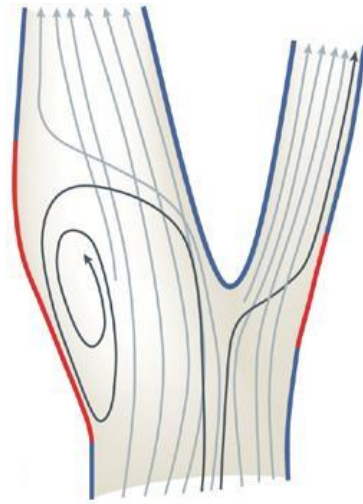
Biological Background

The formation of plaques is one of the main biological processes associated with atherosclerosis, and plays a key role in atherosclerotic lesions in blood vessels. Atherosclerotic plaques are formed primarily in the intima, the innermost layer of the vessel wall, while the other two layers are called the media and adventitia. Their formation is initiated by endothelial dysfunction, and followed by penetration of leukocytes such as monocytes from the blood flow into the vessel wall, inducing the growth of plaques. As plaques become vulnerable, their rupture may be triggered by stresses applied on them, with thrombosis superimposed. The thrombus formation after plaque rupture is one of the main causes for the blockage of a main artery and can lead to ischaemic or myocardial infarctions as well as other cardiovascular diseases.

In this chapter we aim to give a short introduction about the biological background of plaque formation. We start with the inducing factors of atherosclerosis in Section 1.1, and in Section 1.2 we identify the main steps leading from a normal vessel wall to a rupture-prone atherosclerotic plaque. After introducing the main components of a mature plaque, which are closely related to the vulnerability of plaques in Section 1.3, we finally explain the thrombotic response to plaque rupture in Section 1.4.

1.1 Inducing factors of atherosclerosis

The initiation and growth of atherosclerotic plaques are the results of a hemodynamic interaction between the blood flow and the vessel wall, involving several pathologic processes^[15;23;52;61]. In straight regions of blood vessels, e.g. the blue segments in Figure 1.1, the blood flow is always in the same



Nature Reviews | Molecular Cell Biology

Figure 1.1: Vascular bifurcation and flow patterns. From C. Hahn and M. A. Schwartz^[23].

direction and *flow patterns* are laminar, even though the rate of blood flow changes during the cardiac cycle. However if blood vessels divide or curve sharply, there are regions where the blood flow is reduced and can even reverse its direction during the cardiac cycle, like the red segments in Figure 1.1. In regions of high laminar flow patterns, *endothelial cells* are aligned in the direction of flow, having a low level of permeability and low rates of proliferation and death. In these regions atherosclerosis can not appear. By contrast, in regions of atherogenic flow patterns, including low flow, flow separation, flow reversal and other types of disturbed flow, endothelial cells have high rates of proliferation and death, high permeability of solutes and failure to align in the direction of flow^[23]. This endothelial dysfunction can also be caused by several different sources^[73], and appears to be the initial event in atherosclerosis leading to the migration of macromolecules into the intima. The infiltration and retention of excess *low-density lipoproteins* (LDLs) in the intima initiate an inflammatory response in the vessel wall, and the modification of LDLs through oxidation or enzymatic attack in the intima induces endothelial cells to express adhesion receptors to attract leukocytes, especially *monocytes*^[24]. The disturbed flow patterns in atherosclerosis susceptible regions can increase the expression of adhesion receptors by endothelial cells. Therefore, hemodynamic flow patterns and modified LDLs may initiate an inflammatory process in the vessel wall, and the next steps of atherosclerotic plaque formation will be introduced in Section 1.2.

1.2 Evolution of the rupture-prone atherosclerotic plaque

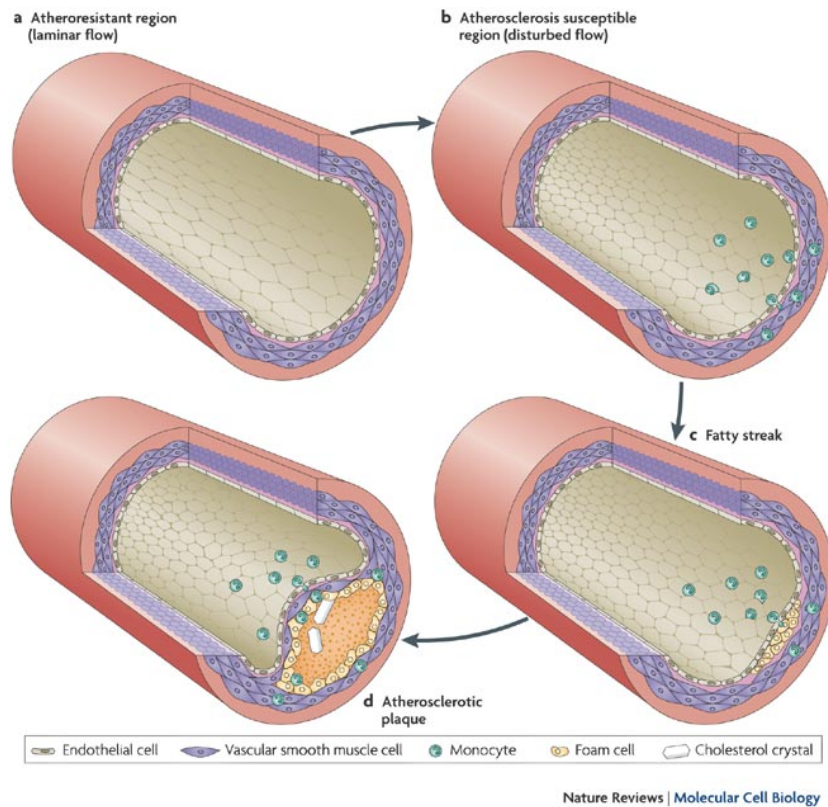


Figure 1.2: Formation of an atherosclerotic plaque. From C. Hahn and M. A. Schwartz^[23].

Figure 1.2 shows the key steps of atherosclerotic plaque formation, which consist of complicated biochemical processes. As we mentioned in Section 1.1, the modification of LDLs to oxidized LDLs let endothelial cells be activated and express leukocyte adhesion receptors, such as E-selectin, vascular cell adhesion molecule 1 (VCAM 1) and intercellular adhesion molecule (ICAM 1); increased numbers of monocytes are attracted and migrate into the vessel wall^[23;24;52](see Figure 1.2, part b). After induced by a cytokine produced in the inflamed intima, the macrophage colony-stimulating factor, monocytes entering the vessel wall differentiate into *macrophages*. This is a critical step for the development of atherosclerosis, because these immune cells take up LDLs, which carry cholesterol and triglycerides to the tissues. And they also produce pro-inflammatory cytokines which make endothelial

cells attract more monocytes into the vessel wall^[41]. Finally macrophages are transformed into *foam cells* which are engorged of lipid, and the accumulation of these cells can thicken the smooth muscle cell layer and form fatty streaks (see Figure 1.2, part c).

Fatty streaks are prevalent in all individuals, including children and healthy young adults. They don't cause symptoms but may eventually progress to more inflamed lesions called atherosclerotic plaques^[24]. The rate of this progression is determined by some risk factors such as levels of plasma lipoproteins, oxidants from smoking or other sources, elevated blood glucose, circulating inflammatory mediators and lack of exercise^[23]. In the center of an atherosclerotic plaque, foam cells and extracellular lipid droplets form a *lipid core* surrounded by a cap of smooth muscle cells and a collagen-rich matrix. This core usually contains cholesterol crystals which fatty streaks rarely contain, and more foam cells will accumulate in this region to let the plaque grow^[64](see Figure 1.2, part d). On the other hand, fatty streaks may also reach an equilibrium and stabilize at that morphology without progressing further, and when risk factors change favorably, they can even regress and disappear. In this case *high density lipoproteins* (HDLs) play a positive role to carry lipids away from macrophages and oppose the effects of LDLs^[23]. Generally speaking in Figure 1.2, the progressions from part a to part b and from part b to part c start in children and can be inverted, while the progression from a healthy vessel wall to part d is not invertible and can finally lead to the formation a rupture-prone atherosclerotic plaque after a long time of evolution.

1.3 Main components of a plaque

As the name "athero-sclerosis" implies, a mature plaque typically consists of two main components: the soft, lipid-rich atheromatous core and the hard, collagen-rich sclerotic tissue^[42]. The atheromatous core is rich in extracellular lipids, cholesterol and its esters^[63]. It is generally believed that the death of foam cells plays an important role in lipid accumulation and core formation, while LDLs retained within the extracellular space, without being taken up and subsequently released by macrophages, may also contribute to them. With the formation and growth of lipid core, smooth muscle cells migrate from the media into the intima, and then elaborate the extracellular matrix. In later stages, a sclerotic tissue called *fibrous cap*, composed primarily of extracellular matrix proteins, is formed over the lipid core^[87]. From Figure 1.3 we can see that the lipid core is separated from the vessel lumen (region

1.3. MAIN COMPONENTS OF A PLAQUE

with the letter L) by the fibrous cap which is formed by connective tissue and smooth muscle cells.



Figure 1.3: Histology of an eccentric, fatty, coronary plaque. From A. Sambola et al.^[62].

The atheromatous core is the most dangerous component, because the soft lipid in the core with local inflammatory process destabilizes plaques and makes them vulnerable to rupture with high risk of subsequent thrombus formation. In contrast, the sclerotic tissue is a relatively benign component, since collagen secreted by smooth muscle cells stabilizes plaques and protects them against disruption. Therefore both of these two components are major determinants of a plaque's vulnerability to rupture^[42]. The size of the atheromatous core is critical for the stability of plaques. The larger area a core occupies in the plaque, the more vulnerable the plaque is. The consistency of the core, depending on temperature and lipid composition, is probably also important for the stability of plaques. For instance, if temperature increases, like with inflammation, the core will become softer. And lipid in the form of cholesterol esters soften the core while cholesterol crystals have the opposite effect^[63]. On the other hand, the mechanical strength of the fibrous cap is a vital component of plaque stability, so cap thinning, reduced collagen content and a decline in smooth muscle cell density can lead to the increase of a plaque's vulnerability to rupture. In addition, the cap inflammation, e.g. the infiltration of macrophages, may locally weaken the fibrous cap and is particularly associated with plaque rupture^[35].

1.4 Plaque rupture and thrombotic response

As an inducement of ischaemic or myocardial infarctions as well as other cardiovascular diseases, the blockage of a main artery was previously thought to be caused by progressive luminal stenosis from continued plaque growth. However angiographic studies have identified that it is plaque rupture rather than stenosis precipitating ischemia and infarct^[24]. When the plaque becomes vulnerable with a large core and a thin cap, its rupture may happen and will be followed by *thrombus* formation, causing a rapid growth of the lesion. Plaque rupture often occurs where the cap is thinnest and most heavily infiltrated by macrophages and therefore weakest. These regions are called the cap's shoulders^[15;42], and they are also points where biomechanical forces acting on plaques may be at a critical value. So the risk of plaque rupture is related to both intrinsic plaque vulnerability and extrinsic stresses applied on plaques. The former feature is a prerequisite for plaque rupture, and the latter forces, including stresses in the blood flow and the vessel wall, may trigger the rupture of vulnerable plaques.

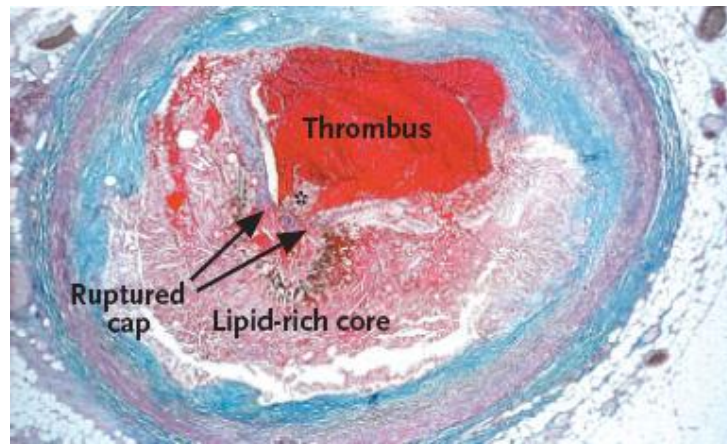


Figure 1.4: A thrombus superimposed on a lipid-rich atherosclerotic plaque. From G. K. Hansson^[24].

Figure 1.4 is a cross-sectioned coronary artery from a patient dying of a massive myocardial infarction^[24]. We can see that there is an occlusive thrombus superimposed on a lipid-rich atherosclerotic plaque. Plaque rupture has happened on the fibrous cap covering the lipid-rich core, and thrombogenic material is exposed to the flowing blood. Platelets in the blood flow adhere to the rupture region and form an aggregate to stem blood loss^[74], however this aggregation causes flow obstruction and thrombosis superimposed on the plaque rapidly. Finally an occluding thrombus is formed on the surface of

1.4. PLAQUE RUPTURE AND THROMBOTIC RESPONSE

the plaque to block the artery and causes myocardial infarction and sudden death.

In another situation, some material of thrombus may also be taken away by the blood flow when plaque rupture happens. It becomes an embolus and moves in the blood flow to a different location of the cardiovascular system. This embolus can induce the blockage in another part of the artery. Since an embolus arises from somewhere, and blocks the artery in another place, the blockage is a sudden onset, and symptoms are usually maximal in the beginning. The problem becomes global, which is solved only temporarily by local therapy, so it is important to identify the source of the embolus. In addition, symptoms may also decrease or disappear as the embolus is partially resorbed and moves to another different location or totally dissipates.

CHAPTER 1. BIOLOGICAL BACKGROUND

Chapter 2

Mathematical Model

In order to demonstrate a quantitative understanding of the physiological processes mentioned in Chapter 1, an appropriate mathematical model to describe the formation of plaques is derived in this chapter. In Section 2.1 we give a review of some existing mathematical models for the biochemical reactions in atherosclerosis and the mechanics of a mature plaque; our model concentrates on both of them. The processes to be modeled are listed in Section 2.2, where the computational domain and main variables are also given. From Section 2.3 to Section 2.7, we go step by step through the complicated modeling procedure and provide the final model in the last section, Section 2.8.

In this model, both the interaction between the blood flow and the vessel wall, and the growth of plaques due to the penetration of monocytes from the blood flow into the vessel wall are considered. The domain we are considering consists of two parts, a fluid part representing the part occupied by the blood flow, and a solid part representing the part occupied by the vessel wall. The interface between the fluid and the solid part moves due to plaque growth and the fluid-structure interaction. The Navier-Stokes equations are used to describe the dynamics of fluid (blood flow) whereas in the solid part (vessel wall) the equations for structural mechanics are considered. Additionally, the motion of monocytes is described by the convection-diffusion-reaction equation, coupled with an equation for the accumulation of foam cells. The transmission conditions are also given on the interface. The concentration of foam cells is also related to the growth modeling of the solid part by influencing its mechanical properties. Finally, the metric of growth is introduced to measure the stress tensor in a right way, and its evolution equation is derived.

2.1 Overview of existing results

Mathematical modeling can play a significant role in helping to understand the development of atherosclerosis^[41]. Since possible contributors to the development of atherosclerosis can be categorized as biochemical or biomechanical^[73], there have also been different mathematical models developed for different objectives.

Models for biochemical processes

The atherosclerosis lesion consists of complicated biochemical processes, and the development involves complex interactions between cholesterol, immune cells, smooth muscle cells and other components. Some experimental results show that cholesterol may not be as influential in the progression of the disease as previously thought^[41;81]. And the macrophages, into which the monocytes differentiate, are a major player in the inflammatory process of atherosclerosis^[31;66]. Some mathematical models, based on partial differential equations (PDE) or ordinary differential equations (ODE), have been devised to study the role of the biochemical reactions in the formation of atherosclerotic lesion.

In the model of Ibragimov et al.^[31], a system of six PDEs is used to describe the chemotactic activity of immune cells (primarily macrophages), smooth muscle cells, chemoattractant and low density lipoproteins (LDL); numerical simulations are performed to demonstrate that this model captures certain observed features of cardiovascular disease such as the localization of immune cells, the build-up of lipids and the isolation of a lesion by smooth muscle cells. On the other hand, the model of Ougrinovskaia et al.^[41] is reduced to a spatially independent ODE, which focuses on how the macrophages take up LDL, and this model's results indicate that it is macrophage proliferation and constant signalling to the endothelial cells, rather than an increase in influx of LDL, that drives lesion instability. And there are also some mathematical models for the transport of LDL from the blood flow into the arterial wall^[2;13;43], a process which plays an important role in the process of atherogenesis. In these models, the biochemical processes are either in the early stage when plaques have not begun to grow or in the stage when the artery is already stenosed, so the computational domain is always fixed and the growth of diseased tissue is not considered.

Models for biomechanics

The biomechanical forces are given by stresses in the blood flow and the vessel wall; they may lead to the rupture of plaques if they are at a critical value. Since the plaque is a component of the vessel wall, its mechanical properties should be similar to the other soft biological tissues, and there are a lot of relevant constitutive models developed to derive the stress^[25-27;34]. The vessel wall is highly elastic and deformed under the blood flow, so the fluid-structure interaction problem is considered^[45;53]. On the interface, the velocity of the blood flow and the displacement of the vessel wall have continuous transmission conditions, and the forces in both of them are also balanced.

In the model of Tang et al., the nonlinear modified Mooney-Rivlin model is used to describe the material properties of the vessel wall and plaque components^[5;70], and the fluid-structure interaction problem is used to perform stress value which may be related to plaque rupture. Different coefficients of the constitutive model are used to distinguish the mechanical properties of different components in the vessel wall and plaque tissue, and the fibrous structure of the cap and the liquid property of the core are not considered. The results indicate that the stress values from both the blood flow and the vessel wall are affected by many factors such as stenosis severity, lipid core size, plaque cap thickness, and fluid-structure interactions^[67]; they may also contribute to continued plaque progression^[69]. The anisotropic material property is also considered to improve the accuracies of plaque stress predictions^[68;82]. The stress distributions obtained by the simulation of the model are used for possible plaque rupture predictions, so in this kind of model the plaque has already been formed, and the growth of the plaque due to biochemical reactions is also neglected.

2.2 Processes to be modeled

In this thesis, the goal is to derive a model to describe the whole evolution process from healthy tissue to a mature plaque which could rupture in the long term, and the model is based on the framework that the adhesion and penetration of monocytes lead to the formation and growth of atherosclerotic plaques. Compared to the existing model by Zohdi et al.^[87], our model concentrates not only on how biochemical processes lead to plaque growth, but also on continuum mechanics of the blood flow and the vessel wall. The processes we are interested in modeling are listed as follows:

1. Adhesion and penetration of monocytes into the vessel wall

The chemical dynamics in the blood flow and interaction with the vessel wall are important aspects relevant both for the physiology of the blood vessels and for the development of certain vascular diseases^[45]. In particular, the adhesion and penetration of monocytes from the blood flow into the vessel wall is highly related to the development of atherosclerosis. So the motion of monocytes both in the blood flow and in the vessel wall is taken into account in our model. This process is described by the convection-diffusion equation, which is also used to describe the motion of platelet, oxygen and other similar particles or solutes in human body^[17;48;74–76].

2. Accumulation of foam cells in the vessel wall, leading to plaque growth

After migrating into the vessel wall, the monocytes first differentiate into macrophages, take up lipoproteins and then become foam cells, leading to the formation of atherosclerotic plaques. Plaque growth strongly depends upon the accumulation of foam cells, which can be considered as the source of growth. Since the mass of the diseased vessel wall increases with an increase in the concentration of foam cells, the mechanics of the vessel wall with a rising mass should be considered^[3;11;37].

3. Changing of the mechanical properties of the vessel wall due to the influence of foam cells

In a completely formed plaque there are different components which are mentioned in Chapter 1, and the mechanical properties are quite different in different parts^[70]. For example the calcification is much stiffer than the fibrous cap and the non-diseased tissue, and the lipid core is much softer^[28;68]. As the plaque is formed and growing, the mechanical properties of the vessel wall are also changed. Since plaque formation is induced by the accumulation of foam cells, in our model the mechanical properties of the vessel wall are positioned to be dependent on the concentration of foam cells.

4. Interaction between the blood flow and the vessel wall

Like some other models for the biomechanics of a mature plaque^[36;67–70;82], the continuum mechanics of both the blood flow and the vessel wall are considered in our model, and the *fluid-structure interaction (FSI) problem* is used to describe their coupled dynamics. The FSI problem is a two-way coupled system. The vessel wall is deformed by the blood flow, and the blood flow is also influenced by the deformation of the vessel wall^[45;53]. The interaction between fluid and structure is given by the continuity of velocity and

2.2. PROCESSES TO BE MODELED

the balance of force^[12;16;18;32;38;45;53;78]. Via the coupled system of FSI the stress value, one of the factors leading to plaque rupture, can be computed.

Based on the processes to be modeled above, the computational domain and principal quantities are determined in the following. Figure 2.1 sketches the situation that the lumen of the blood vessel is already stenosed by plaque growth. It consists of two parts, the fluid part Ω_f^t representing the part occupied by the blood flow, and the solid part Ω_s^t representing the part occupied by the vessel wall. $\Gamma_{f,in}$ represents the inlet and $\Gamma_{f,out}$ represents the outlet of the blood vessel. The interface $\Gamma_1^t \cup \Gamma_2^t$ moves due to plaque growth and the fluid-structure interaction. The difference between Γ_1^t and Γ_2^t is that Γ_1^t is the diseased part of the vessel wall and is permeable for the monocytes, so its displacement is larger than Γ_2^t because the monocytes migrate through Γ_1^t into the vessel wall and lead to plaque growth. $\Gamma_{f,wall}$ is also the interface between the blood flow and the vessel wall, and since the vessel wall at the side of $\Gamma_{f,wall}$ is healthy, its displacement is much smaller than the other side with plaque growth and we assume that $\Gamma_{f,wall}$ is a fixed boundary compared to the large deformation of $\Gamma_1^t \cup \Gamma_2^t$. In addition, $\Gamma_{s,wall}$ denotes the interface between the vessel wall and the tissue around the blood vessel, and $\Gamma_{s,in} \cup \Gamma_{s,out}$ denotes the boundaries of the considered segment of the vessel wall. They are all assumed to be fixed.

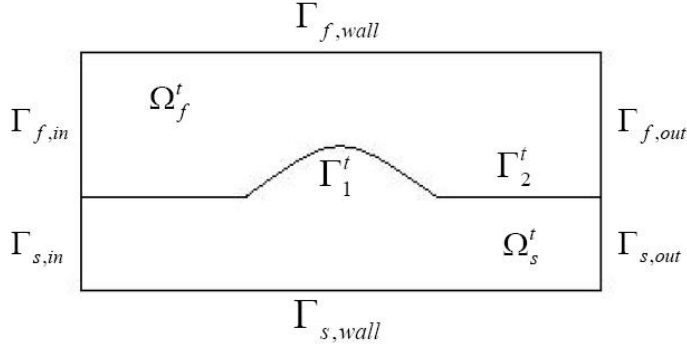


Figure 2.1: Computational domain

The principal quantities describing the blood flow in Ω_f^t are the velocity v_f and the pressure p_f ; the displacement of the vessel wall u_s in Ω_s^t due to plaque growth and the fluid-structure interaction is another quantity of relevance^[45]. The convection-diffusion process of monocytes is an important aspect of the blood flow, so the concentration of monocytes c_f in Ω_f^t is also the principal quantity. When the monocytes migrate into the vessel wall Ω_s^t and finally differentiate into foam cells, the relevant quantities are the concentration of

monocytes c_s and the concentration of foam cells c_s^* . Since the vessel wall is growing due to the accumulation of foam cells, the density of the vessel wall ρ_s is another quantity, which will increase for plaque growth. All the equations of these main variables will be derived in the next five sections and the final model will be given in Section 2.8.

2.3 Kinematics of continuum media

In order to derive the differential equations governing the *fluid dynamics* of the blood flow and the *structural mechanics* of the vessel wall, we need to introduce the concepts about *kinematics* at first^[9;16;25;30;45;51;53;59]. Let there be given a bounded, open, connected subset Ω_0 of \mathbb{R}^d with a sufficiently smooth boundary, filled by a continuum medium. d is the dimension of the space we consider. We define a smooth one-to-one mapping:

$$x(\cdot, t) : \Omega_0 \rightarrow \Omega_t, \quad X \mapsto x = x(X, t)$$

This mapping is called the *deformation*, which implies that the material particle X is moved to a new position x after some time $t \in I = [0, T]$, and has the inverse mapping $X(x, t)$. We call Ω_0 the *reference configuration*, and Ω_t the *current (or deformed) configuration*. A quantity associated with the medium can be described as a function of either the variables (x, t) or (X, t) . The first couple is called the *Eulerian* variables, and the function $\phi(x, t)$ is defined in the current configuration, denoting the quantity in the space point x at time t . The second one is called the *Lagrangian* variables, and to make the difference, we mark the function $\hat{\phi}(X, t)$ with the hat symbol. This function is defined in the reference configuration and denotes the quantity of the material particle X at time t . So there are two different frameworks and to treat different problems, we use Eulerian or Lagrangian frameworks to define a quantity expressed as a function. For example, the vector quantity

$$u(x, t) = x - X(x, t) = \hat{u}(X, t) = x(X, t) - X, \quad x = x(X, t) \in \Omega_t, X \in \Omega_0, t \in I$$

is called the *displacement*, which is a major kinematic quantity of our problem. Another important quantity of kinematics is the *velocity*. In the Lagrangian framework it is expressed by the vector field $\hat{v} = \hat{v}(X, t)$ defined as

$$\hat{v}(X, t) = \frac{\partial}{\partial t} x(X, t) = \frac{\partial}{\partial t} \hat{u}(X, t), \quad X \in \Omega_0, t \in I$$

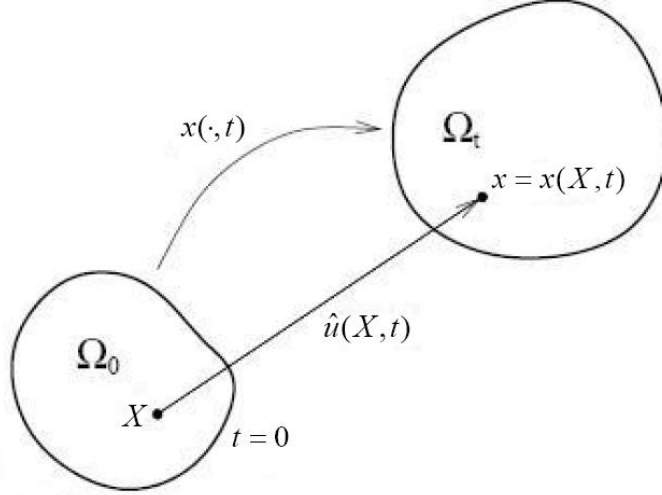


Figure 2.2: Deformation and displacement in the Lagrangian framework. Modified from A. Quarteroni and L. Formaggia^[45].

In the Eulerian framework, since the variable x is dependent on time t , the velocity is defined as

$$\begin{aligned} v(x, t) &= \frac{d}{dt}u(x, t) = \frac{\partial}{\partial t}u(x, t) + \frac{dx}{dt} \cdot \frac{\partial}{\partial x}u(x, t) \\ &= \frac{\partial}{\partial t}u(x, t) + v(x, t) \cdot \nabla u(x, t), \quad x \in \Omega_t, t \in I \end{aligned}$$

Here we use the symbol ∇ to indicate the gradient with respect to the Eulerian variables (x, t) , and the symbol $\frac{d}{dt}$ is called the *material derivative*. If we consider some other quantities in kinematics, its time derivative $\frac{\partial}{\partial t}$ in the Lagrangian framework should also be changed to material derivative $\frac{d}{dt}$ in the Eulerian framework.

We can also use $\hat{\nabla}$ to indicate the gradient with respect to the Lagrangian variables (X, t) . Then the *deformation gradient* \hat{F} is defined as

$$\hat{F} = \frac{\partial}{\partial X}x(X, t) = \hat{\nabla}x(X, t) = I + \hat{\nabla}\hat{u}(X, t), \quad X \in \Omega_0, t \in I$$

Each component of this $d \times d$ matrix is given as

$$\hat{F}_{ij} = \frac{\partial}{\partial X_j} x_i(X, t), \quad i, j = 1, 2, 3, \dots, d, \quad X \in \Omega_0, t \in I$$

Since the deformation is smooth, injective and *orientation preserving*, the deformation gradient \hat{F} is invertible and its determinant $\hat{J} = \det \hat{F}$ is everywhere strictly positive^[9].

The material derivative and the deformation gradient are both crucial concepts for the derivation of our mathematical model. The material derivative indicates the change of a quantity for a certain material particle X which is at the position $x=x(X,t)$ at time t , and the deformation gradient is clearly linked to the rule which transforms integrals from the current to the reference configuration. Here are two lemmas related to them.

Lemma 2.3.1. *Let V_t be a subdomain of Ω_t and let us consider the function: $\phi(\cdot, t) : V_t \rightarrow \mathbb{R}^d$. Let $V_0 = \{X \in \Omega_0 : x(X, t) \in V_t\}$. $\hat{\phi}(X, t) = \phi(x(X, t), t)$ and ϕ is integrable in V_t . Then the transformation formulas for integrals are satisfied as follows:*

$$\int_{V_t} \phi(x, t) dx = \int_{V_0} \hat{\phi}(X, t) \hat{J} dX \quad (2.1)$$

$$\int_{\partial V_t} \phi(x, t) \cdot nda = \int_{\partial V_0} \hat{\phi}(X, t) \cdot \hat{J} \hat{F}^{-T} \cdot NdA \quad (2.2)$$

Here ∂V_t and ∂V_0 are the boundaries of V_t and V_0 , and n and N are the unit outer normal vectors of ∂V_t and ∂V_0 .

Proof. The proof of formula (2.1) is obvious and given in literatures^[16;25;30]. By using (2.1) and divergence theorem, the proof of (2.2) is obtained as

$$\begin{aligned} \int_{\partial V_t} \phi \cdot nda &= \int_{V_t} \operatorname{div} \phi dx = \int_{V_0} \widehat{\operatorname{div}} \hat{\phi} \hat{J} dX = \int_{V_0} \hat{\nabla} \hat{\phi} : (\nabla X)^T \hat{J} dX \\ &= \int_{V_0} \hat{\nabla} \hat{\phi} : \hat{J} \hat{F}^{-T} dX = \int_{\partial V_0} \hat{\phi} \cdot \hat{J} \hat{F}^{-T} \cdot NdA - \int_{V_0} \hat{\phi} \cdot \widehat{\operatorname{div}}(\hat{J} \hat{F}^{-T}) dX \end{aligned}$$

Here the inner product of matrix $A : B = \sum_{i,j=1}^d A_{ij} B_{ij}$. div and $\widehat{\operatorname{div}}$ indicate the divergences with respect to x and X . Since the cofactor matrix of \hat{F} is $\operatorname{Cof} \hat{F} = \hat{J} \hat{F}^{-T}$, and the fact $\widehat{\operatorname{div}}(\operatorname{Cof} \hat{F}) = 0$ is proved^[9], the result $\widehat{\operatorname{div}}(\hat{J} \hat{F}^{-T}) = 0$ is achieved. So (2.2) is proved. □

Lemma 2.3.2. *Let F denote the deformation gradient in the Eulerian framework, $F(x, t) = \hat{F}(X(x, t), t)$ and $J = \det F$. Then*

$$\frac{dJ}{dt} = J \operatorname{div} v \quad (2.3)$$

Proof. First we note that

$$\frac{dF}{dt} = \frac{d}{dt} \left(\frac{\partial x}{\partial X} \right) = \frac{\partial}{\partial X} \left(\frac{dx}{dt} \right) = \frac{\partial}{\partial X} \left(\frac{du}{dt} \right) = \frac{\partial v}{\partial X} = \frac{\partial v}{\partial x} \cdot \frac{\partial x}{\partial X} = \nabla v \cdot F$$

Combine the above formula with the below one^[25]:

$$\frac{\partial J}{\partial F} = J F^{-T}$$

and we can achieve (2.3) as follows:

$$\frac{dJ}{dt} = \frac{\partial J}{\partial F} : \frac{dF}{dt} = (J F^{-T}) : (\nabla v \cdot F) = J \operatorname{tr}(\nabla v \cdot F \cdot F^{-1}) = J \operatorname{tr}(\nabla v) = J \operatorname{div} v$$

Here tr denotes the trace of a matrix: $\operatorname{tr} A = \sum_{i=1}^d A_{ii}$. □

Based on the above two lemmas, we can achieve the *Reynolds transport theorem*, which plays a key role in the derivation of conservation equations in continuum mechanics^[45;51;53;59]. In the sequel of this section, V_0 is a subdomain of Ω_0 , and V_t is its image under the deformation in Ω_t .

Theorem 2.3.3 (Reynolds transport theorem). *Let $\phi = \phi(x, t) : \Omega_t \times I \rightarrow \mathbb{R}$ be a smooth scalar function with respect to both variables x and t . Then*

$$\frac{d}{dt} \int_{V_t} \phi dx = \int_{V_t} \left\{ \frac{d\phi}{dt} + \phi \operatorname{div} v \right\} dx = \int_{V_t} \left\{ \frac{\partial \phi}{\partial t} + \operatorname{div}(\phi v) \right\} dx \quad (2.4)$$

Proof. By using formula (2.1) and (2.3), we can get

$$\begin{aligned} \frac{d}{dt} \int_{V_t} \phi dx &= \frac{\partial}{\partial t} \int_{V_0} \hat{\phi} \hat{J} dX = \int_{V_0} \left\{ \frac{\partial \hat{\phi}}{\partial t} \hat{J} + \hat{\phi} \frac{\partial \hat{J}}{\partial t} \right\} dX = \int_{V_t} \left\{ \frac{d\phi}{dt} + \phi \frac{dJ}{dt} J^{-1} \right\} dx \\ &= \int_{V_t} \left\{ \frac{d\phi}{dt} + \phi \operatorname{div} v \right\} dx = \int_{V_t} \left\{ \frac{\partial \phi}{\partial t} + v \cdot \nabla \phi + \phi \operatorname{div} v \right\} dx = \int_{V_t} \left\{ \frac{\partial \phi}{\partial t} + \operatorname{div}(\phi v) \right\} dx \end{aligned}$$

□

For a function with

$$\frac{d}{dt} \int_{V_t} \phi dx = 0$$

By using the divergence theorem we can get the formula from (2.4) that

$$\frac{d}{dt} \int_{V_t} \phi dx = \int_{V_t} \frac{\partial \phi}{\partial t} dx + \int_{\partial V_t} \phi v \cdot nda \Rightarrow \int_{V_t} \frac{\partial \phi}{\partial t} dx = - \int_{\partial V_t} \phi v \cdot nda$$

This formula gives the fact that the change of the value ϕ in V_t over time equals the negative outflux over the boundary of V_t .

2.4 Fluid dynamics

2.4.1 Conservation equations

With the help of Reynolds transport theorem, we can derive the *conservation equations* of mass and momentum in fluids (like the blood flow). Since the fluid is modeled by describing its properties in the space point x , its conservation equations are derived in the Eulerian framework. Let the material in Ω_t has certain distributed quantities like the *density* $\rho(x, t) : \Omega_t \times I \rightarrow \mathbb{R}$ and the momentum ρv , where $v(x, t) : \Omega_t \times I \rightarrow \mathbb{R}^d$ denotes the velocity. So the mass of the volume $V_t \subset \Omega_t$ can be defined as

$$m(V_t) = \int_{V_t} \rho dx$$

The fundamental principle of physics states that mass is neither created nor destroyed during the motion, so the mathematical statement of this principle is given as

$$\frac{d}{dt} m(V_t) = 0$$

Combining it with Reynolds transport theorem, we obtain

$$\int_{V_t} \left\{ \frac{\partial \rho}{\partial t} + \text{div}(\rho v) \right\} dx = 0$$

Since this formula holds for every volume V_t , we can get the *conservation equation of mass*:

$$\frac{\partial \rho}{\partial t} + \operatorname{div}(\rho v) = 0 \quad \text{in } \Omega_t \quad (2.5)$$

The momentum of the volume V_t is defined similarly as

$$M(V_t) = \int_{V_t} \rho v dx$$

and to derive the conservation equations of momentum, the force applied on the volume V_t should also be given. In general case it has two parts and has the form as

$$F(V_t) = \int_{V_t} \rho f^b dx + \int_{\partial V_t} t da$$

Here $f^b(x, t) : \Omega_t \times I \rightarrow \mathbb{R}^d$ is called the *body (or volume) forces*, such as gravity and electromagnetic forces, which act on all material particles in the body without physical contact. The other kind of forces is called the *surface forces*, including pressure and frictional forces, which act with physical contact on the surface of the body. By Cauchy principle^[9;45], they are described by the vector

$$t = t(x, t, n) : \Omega_t \times I \times S_1 \rightarrow \mathbb{R}^d$$

with

$$S_1 = \{n \in \mathbb{R}^d : |n| = 1\}$$

The Cauchy stress tensor theorem^[9;45] shows the fact that there exists a smooth symmetric tensor $\sigma = \sigma(x, t) : \Omega_t \times I \rightarrow \mathbb{R}^d \times \mathbb{R}^d$, such that the force acting on a surface with unit normal vector n is given by $\sigma \cdot n$. σ is called the *Cauchy stress tensor* (p.s.: the symmetry of the Cauchy stress tensor is derived from the conservation equations of angular momentum^[9;45]). Then $t(x, t, n) = \sigma(x, t) \cdot n$, and

$$F(V_t) = \int_{V_t} \rho f^b dx + \int_{\partial V_t} \sigma \cdot n da = \int_{V_t} \{\rho f^b + \operatorname{div} \sigma\} dx$$

Newton's law tells that the change of momentum over time is equal to the acting forces, so

$$\frac{d}{dt}M(V_t) = F(V_t) \quad \Rightarrow \quad \frac{d}{dt} \int_{V_t} \rho v dx = \int_{V_t} \{\rho f^b + \text{div} \sigma\} dx$$

Combining it with Reynolds transport theorem and the conservation equation of mass (2.5), we obtain the *conservation equations of momentum* as

$$\rho \frac{\partial v}{\partial t} + \rho v \cdot \nabla v = \rho f^b + \text{div} \sigma \quad \text{in } \Omega_t \quad (2.6)$$

In addition, the material (including both the blood flow and the vessel wall) in volume V_t is assumed to be in *isothermal conditions*, so the conservation equation of energy and the entropy inequality can be neglected.

2.4.2 Incompressible flows

Concerning the conservation equation of mass (2.5), we now let the material in Ω_f^t be fluid, and use the lower index "f" to denote that all the quantities are related to fluids, so the set of conservation equations is now written as

$$\begin{aligned} \frac{\partial \rho_f}{\partial t} + \text{div}(\rho_f v_f) &= 0 \quad \text{in } \Omega_f^t \\ \rho_f \frac{\partial v_f}{\partial t} + \rho_f v_f \cdot \nabla v_f &= \rho_f f_f^b + \text{div} \sigma_f \quad \text{in } \Omega_f^t \end{aligned} \quad (2.7)$$

If the density ρ_f is constant (e.g. the blood flow), it is obtained that

$$\text{div} v_f = 0$$

For (2.3), it is equivalent to

$$\frac{d}{dt} J_f = 0$$

which is called the *incompressibility constraint*. If the flow satisfies the incompressibility constraint, it is called the *incompressible flow*. From the above derivation we can get the following implication:

constant density fluid \Rightarrow incompressible flow

whereas the converse is not true in general^[45]. By employing Reynolds transport theorem (2.4) with $\phi = 1$ we can note that the incompressibility constraint is equivalent to

$$\frac{d}{dt} \int_{V_f^t} dx = 0$$

for every volume $V_f^t \subset \Omega_f^t$. So the incompressible flow preserves the fluid volume, which nearly does not change in time.

The conservation equations are derived from very basic principles and can be used to describe the mechanics of many different materials. Since the blood flow is typically a kind of incompressible flows, if we use the set of equations (2.7) to describe the dynamics of the blood flow, the material in V_f^t should be considered as an incompressible flow, and the related conservation equations are changed to

$$\begin{aligned} \operatorname{div} v_f &= 0 \quad \text{in } \Omega_f^t \\ \rho_f \frac{\partial v_f}{\partial t} + \rho_f v_f \cdot \nabla v_f &= \rho_f f_f^b + \operatorname{div} \sigma_f \quad \text{in } \Omega_f^t \end{aligned} \quad (2.8)$$

To achieve the conservation equations for an incompressible flow, we also need to derive constitutive equations to link the stress tensor σ_f to the other quantities such as the density ρ_f and the velocity v_f . Here we assume that the fluid is a Stokes fluid, which has the properties of symmetry and isotropy^[51;53], and also a Newtonian fluid, which is generally valid in large vessels^[45]. Since the fluid reacts mechanically to the rate of deformation^[16], if the property of the fluid is independent on its temperature (it is available in isothermal material), the stress tensor σ_f can have the form:

$$\sigma_f = -p_f I + \mu_f (\nabla v_f + \nabla v_f^T) - \frac{2}{3} \mu_f \operatorname{div} v_f I$$

The scalar function p_f is the *hydrostatic pressure* of the fluid. I is the unit matrix. The coefficient μ_f is called the *dynamic viscosity* and is dependent on the density ρ_f , so it can also be written as

$$\mu_f = \rho_f \nu$$

The coefficient ν is called the *kinematic viscosity*. Since the fluid is incompressible, then $\text{div}v_f = 0$ and the above form of stress tensor becomes

$$\sigma_f = -p_f I + \rho_f \nu (\nabla v_f + \nabla v_f^T) \quad \text{in } \Omega_f^t \quad (2.9)$$

Combine the form of stress tensor (2.9) with the conservation equations (2.8), and we can get

$$\begin{aligned} -\text{div}\sigma_f &= \nabla p_f - \rho_f \nu \text{div}(\nabla v_f) - \rho_f \nu \text{div}(\nabla v_f^T) \\ &= \nabla p_f - \rho_f \nu \Delta v_f - \rho_f \nu \nabla \text{div}v_f = \nabla p_f - \rho_f \nu \Delta v_f \end{aligned}$$

Here Δ denotes the Laplacian operator. So the equations for fluid dynamics of the blood flow are given by

$$\begin{aligned} \text{div}v_f &= 0 \quad \text{in } \Omega_f^t \\ \rho_f \frac{\partial v_f}{\partial t} + \rho_f v_f \cdot \nabla v_f - \rho_f \nu \Delta v_f + \nabla p_f &= \rho_f f_f^b \quad \text{in } \Omega_f^t \end{aligned} \quad (2.10)$$

which are called the *Navier-Stokes equations*. These equations investigate the quantities of the blood flow such as the velocity v_f and the pressure p_f , while the density ρ_f is considered as a constant coefficient because the blood flow is assumed to be homogeneous.

Remark 2.4.1 (Non-Newtonian fluid). In the incompressible Newtonian fluid, the stress tensor is written as

$$\sigma_f = -p_f I + 2\rho_f \nu D(v_f)$$

where the tensor defined as

$$D(v_f) = \frac{1}{2}(\nabla v_f + \nabla v_f^T)$$

is called the *strain rate tensor*. If σ_f does not have a linear relation with the tensor $D(v_f)$, the fluid is called the *non-Newtonian fluid*. There are different

models for fluids with different properties^[21]. One of the examples related to our problem is the blood in smaller vessels (with the diameter from 0.2mm to 1cm)^[45]. In this case the blood begins to show a "non-standard" behavior that the viscosity depends on the shear rate tensor:

$$\sigma_f = -p_f I + 2\rho_f \nu (|D(v_f)|) D(v_f) \quad \text{in } \Omega_f^t$$

where $|D(v_f)|$ denotes the principal invariants of $D(v_f)$ ^[25;59].

2.5 Structural mechanics

2.5.1 Conservation equations with growth function

Compared to the derivation of the Navier-Stokes equations for fluid dynamics of the blood flow, the equations for structural mechanics of the vessel wall are also derived from the conservation equations of mass and momentum. One difference is that in this case the mass is created during the formation of plaques, so we mention that the derivation of the equations for structural mechanics is different from their standard derivation. In the derivation of mass conservation equation (2.5), the mass of a volume V_t satisfies

$$\frac{d}{dt} m(V_t) = R(V_t)$$

$R(V_t)$ is the source of the volume $V_t \subset \Omega_t$ leading to the mass increase, and it is defined as

$$R(V_t) = \int_{V_t} f^g dx$$

$f^g = f^g(x, t) : \Omega_t \times I \rightarrow \mathbb{R}$ is called the *growth function*, which represents a time rate of mass growth per unit current volume^[11;37]. By Reynolds transport theorem, the conservation equation of mass can be derived from

$$\frac{d}{dt} \int_{V_t} \rho dx = \int_{V_t} \left\{ \frac{\partial \rho}{\partial t} + \operatorname{div}(\rho v) \right\} dx = \int_{V_t} f^g dx$$

and achieved as

$$\frac{\partial \rho}{\partial t} + \operatorname{div}(\rho v) = f^g \quad \text{in } \Omega_t \quad (2.11)$$

Similarly in the conservation equations of momentum,

$$\frac{d}{dt} \int_{V_t} \rho v dx = \int_{V_t} f^g v dx + \int_{V_t} \{\rho f^b + \operatorname{div} \sigma\} dx$$

where the additional part represents the momentum of the new created mass. Combine the above formula with Reynolds transport theorem and (2.11), and we obtain the conservation equations of momentum

$$\rho \frac{\partial v}{\partial t} + \rho v \cdot \nabla v = \rho f^b + \operatorname{div} \sigma \quad \text{in } \Omega_t \quad (2.12)$$

Combining (2.11) with (2.12), we also use the lower index "s" to denote that all the quantities are related to solids, and the equations for structural mechanics of the vessel wall are written as

$$\begin{aligned} \frac{\partial \rho_s}{\partial t} + \operatorname{div}(\rho_s v_s) &= f_s^g \quad \text{in } \Omega_s^t \\ \rho_s \frac{\partial v_s}{\partial t} + \rho_s v_s \cdot \nabla v_s &= \rho_s f_s^b + \operatorname{div} \sigma_s \quad \text{in } \Omega_s^t \end{aligned} \quad (2.13)$$

Additionally, the conservation equation of energy and the entropy inequality are also neglected because the vessel wall is assumed to be isothermal.

2.5.2 Piola transformation

In deriving the equations for structural mechanics, we also need a different framework from the equations for fluid dynamics. As the solid reacts mechanically to the deformation instead of its rate^[16], in structural mechanics we are more interested in the displacement $\hat{u}_s(X, t) : \Omega_s^0 \times I \rightarrow \mathbb{R}^d$ for every material particle of the reference volume $V_s^0 \subset \Omega_s^0$ ^[9;51;53]. This is the classical Lagrangian framework, so all the equations should be transformed to the reference configuration and the quantities should be redefined by the Lagrangian variables (X,t).

To build a transformation between the Eulerian and Lagrangian frameworks, transformation formulas (2.1) and (2.2) need to be used again. Since the

quantity displacement is of more interest than the velocity, we need to replace v_s with \hat{u}_s in the transformed equations of (2.13). From the definition of velocity in kinematics we know in the Eularian framework,

$$v_s = \frac{du_s}{dt} = \frac{\partial u_s}{\partial t} + v_s \cdot \nabla u_s \quad \text{in } \Omega_s^t \quad (2.14)$$

and its integral form in the current volume $V_s^t \subset \Omega_s^t$ can be written as

$$\int_{V_s^t} v_s dx = \int_{V_s^t} \left\{ \frac{\partial u_s}{\partial t} + v_s \cdot \nabla u_s \right\} dx = \int_{V_s^t} \frac{du_s}{dt} dx$$

By using transformation formula (2.1),

$$\int_{V_s^0} \hat{v}_s \hat{J}_s dX = \int_{V_s^t} v_s dx = \int_{V_s^t} \frac{du_s}{dt} dx = \int_{V_s^0} \frac{\partial \hat{u}_s}{\partial t} \hat{J}_s dX$$

and we can get

$$\hat{v}_s = \frac{\partial \hat{u}_s}{\partial t} \quad \text{in } \Omega_s^0 \quad (2.15)$$

which is the same as the definition of velocity in the Lagrangian framework. The corresponding integral form of mass conservation equation is

$$\frac{\partial}{\partial t} \int_{V_s^0} \hat{\rho}_s \hat{J}_s dX = \frac{d}{dt} \int_{V_s^t} \rho_s dx = \int_{V_s^t} \left\{ \frac{\partial \rho_s}{\partial t} + \text{div}(\rho_s v_s) \right\} dx = \int_{V_s^t} f_s^g dx = \int_{V_s^0} \hat{f}_s^g \hat{J}_s dX$$

with the same application of (2.1). So the conservation equation of mass in the Lagrangian framework is

$$\frac{\partial}{\partial t} (\hat{J}_s \hat{\rho}_s) = \hat{J}_s \hat{f}_s^g \quad \text{in } \Omega_s^0 \quad (2.16)$$

In the derivation of momentum conservation equations in the Lagrangian framework, the transformation formula of the divergence of Cauchy stress tensor $\text{div} \sigma_s$ needs to be achieved. Here we associate with σ_s a tensor \hat{P}_s defined by the Lagrangian variables (X,t) as

$$\hat{P}_s = \hat{J}_s \hat{\sigma}_s \hat{F}_s^{-T} \quad \text{in } \Omega_s^0 \quad (2.17)$$

This transformation is called the *Piola transformation* and \hat{P}_s is called the *first Piola-Kirchhoff stress tensor*. The Piola transformation satisfies the following theorem:

Theorem 2.5.1 (Properties of the Piola transformation). *Let $\hat{P}_s = \hat{P}_s(X, t) : \Omega_0 \times I \rightarrow \mathbb{R}^d \times \mathbb{R}^d$ denote the Piola transformation of $\sigma_s = \sigma_s(x, t) : \Omega_t \times I \rightarrow \mathbb{R}^d \times \mathbb{R}^d$. Then*

$$\int_{V_s^t} \operatorname{div} \sigma_s dx = \int_{V_s^0} \widehat{\operatorname{div}} \hat{P}_s dX \quad (2.18)$$

$$\int_{\partial V_s^t} \sigma_s \cdot n da = \int_{\partial V_s^0} \hat{P}_s \cdot N dA \quad (2.19)$$

Proof. (2.18) and (2.19) are equivalent because of divergence theorem, so combining (2.19) with the Piola transformation (2.17) we just have to prove

$$\int_{\partial V_s^t} \sigma_s \cdot n da = \int_{\partial V_s^0} \hat{\sigma}_s \cdot \hat{J}_s \hat{F}_s^{-T} \cdot N dA$$

Let $\sigma_{s,i}$ be the i -th ($i=1,2,\dots,d$) row-vector of σ_s , and with transformation formula (2.2) we can get

$$\int_{\partial V_s^t} \sigma_{s,i} \cdot n da = \int_{\partial V_s^0} \hat{\sigma}_{s,i} \cdot \hat{J}_s \hat{F}_s^{-T} \cdot N dA$$

Combine each element together to get the tensorial form, and we achieve formula (2.19). □

Based on the Piola transformation, the conservation equations of momentum in current volume V_s^t :

$$\int_{V_s^t} \rho_s \frac{dv_s}{dt} dx = \int_{V_s^t} \left\{ \rho_s \frac{\partial v_s}{\partial t} + \rho_s v_s \cdot \nabla v_s \right\} dx = \int_{V_s^t} \{ \rho_s f_s^b + \operatorname{div} \sigma_s \} dx$$

can be transformed to the Lagrangian framework as

$$\int_{V_s^0} \hat{\rho}_s \frac{\partial \hat{v}_s}{\partial t} \hat{J}_s dX = \int_{V_s^0} \{ \hat{\rho}_s \hat{f}_s^b \hat{J}_s + \widehat{\operatorname{div}} \hat{P}_s \} dX = \int_{V_s^0} \{ \hat{\rho}_s \hat{f}_s^b \hat{J}_s + \widehat{\operatorname{div}} (\hat{J}_s \hat{\sigma}_s \hat{F}_s^{-T}) \} dX$$

So the conservation equations of momentum in the Lagrangian framework are

$$\hat{J}_s \hat{\rho}_s \frac{\partial \hat{v}_s}{\partial t} = \hat{J}_s \hat{\rho}_s \hat{f}_s^b + \widehat{div}(\hat{J}_s \hat{\sigma}_s \hat{F}_s^{-T}) \quad \text{in } \Omega_s^0 \quad (2.20)$$

Combine (2.15) and (2.16) with (2.20), and we write the equations for structural mechanics of the vessel wall as

$$\begin{aligned} \frac{\partial}{\partial t}(\hat{J}_s \hat{\rho}_s) &= \hat{J}_s \hat{f}_s^g \quad \text{in } \Omega_s^0 \\ \hat{J}_s \hat{\rho}_s \frac{\partial \hat{v}_s}{\partial t} &= \hat{J}_s \hat{\rho}_s \hat{f}_s^b + \widehat{div}(\hat{J}_s \hat{\sigma}_s \hat{F}_s^{-T}) \quad \text{in } \Omega_s^0 \\ \frac{\partial \hat{u}_s}{\partial t} &= \hat{v}_s \quad \text{in } \Omega_s^0 \end{aligned} \quad (2.21)$$

and with the relation between velocity \hat{v}_s and displacement \hat{u}_s , the equations can also be written as

$$\begin{aligned} \frac{\partial}{\partial t}(\hat{J}_s \hat{\rho}_s) &= \hat{J}_s \hat{f}_s^g \quad \text{in } \Omega_s^0 \\ \hat{J}_s \hat{\rho}_s \frac{\partial^2 \hat{u}_s}{\partial t^2} &= \hat{J}_s \hat{\rho}_s \hat{f}_s^b + \widehat{div}(\hat{J}_s \hat{\sigma}_s \hat{F}_s^{-T}) \quad \text{in } \Omega_s^0 \end{aligned} \quad (2.22)$$

Here the quantity displacement \hat{u}_s is more important in the equations and is related to the constitutive equations in elastic materials which are used to derive the stress tensor of the vessel wall σ_s in Section 2.7.

Remark 2.5.1 (Equations for structural mechanics without growth). The main difference between the normal equations for structural mechanics and (2.22) is that there is no growth function in the conservation equation of mass. For the conservation of mass, it is given that

$$\frac{d}{dt} \int_{V_s^t} \rho_s dx = 0$$

Let $\hat{\rho}_s^0$ denote the density distribution at time $t = 0$ ^[51;53], and from the above formula we can get

$$\int_{V_s^0} \hat{\rho}_s^0 dX = \int_{V_s^t} \rho_s dx = \int_{V_s^0} \hat{\rho}_s \hat{J}_s dX$$

So the density $\hat{\rho}_s$ in the Lagrangian framework satisfies

$$\hat{\rho}_s \hat{J}_s = \hat{\rho}_s^0$$

Combining it with the conservation equations of momentum (2.20), we can get

$$\hat{\rho}_s^0 \frac{\partial \hat{v}_s}{\partial t} = \hat{\rho}_s^0 \hat{f}_s^b + \widehat{div}(\hat{J}_s \hat{\sigma}_s \hat{F}_s^{-T})$$

So the equations for structural mechanics without growth are written as

$$\begin{aligned} \hat{\rho}_s^0 &= \hat{J}_s \hat{\rho}_s \quad \text{in } \Omega_s^0 \\ \hat{\rho}_s^0 \frac{\partial^2 \hat{u}_s}{\partial t^2} &= \hat{\rho}_s^0 \hat{f}_s^b + \widehat{div}(\hat{J}_s \hat{\sigma}_s \hat{F}_s^{-T}) \quad \text{in } \Omega_s^0 \end{aligned} \quad (2.23)$$

Compared to (2.22), the density $\hat{\rho}_s^0$ in equations (2.23) is a constant coefficient, which is similar to the density ρ_f of the blood flow.

Remark 2.5.2 (The relation between differential elements). Concerning the Piola transformation formula (2.19), we neglect the denotation that all the quantities are related to solids, so the lower index "s" can be removed. Let σ be the unit matrix I , and then the corresponding *differential form* is

$$nda = \hat{J} \hat{F}^{-T} \cdot N dA \quad (2.24)$$

Since n is the unit normal vector, its Euclidean norm $|n| = 1$, so we can get the relation between the *differential elements* da and dA ^[9]:

$$da = \hat{J} |\hat{F}^{-T} \cdot N| dA \quad (2.25)$$

Combine (2.24) with (2.25), and we can also get the relation between the unit outer normal vectors n and N :

$$n = \frac{\hat{J} \hat{F}^{-T} \cdot N}{\hat{J} |\hat{F}^{-T} \cdot N|} \quad (2.26)$$

Additionally, the relation between the differential elements dx and dX is easy to be achieved by transformation formula (2.1):

$$dx = \hat{J}dX \quad (2.27)$$

In order to get the variational form for numerical simulations in Chapter 3, the equations should be transformed between different frameworks. Sometimes formulas (2.25) and (2.27) need to be used.

Remark 2.5.3 (Second Piola-Kirchhoff stress tensor). While the Cauchy stress tensor σ_s is symmetric, in general the first Piola-Kirchhoff stress tensor \hat{P}_s is not, instead the relation is

$$\hat{P}_s^T = \hat{F}_s^{-1} \hat{P}_s \hat{F}_s^T$$

It is nevertheless desirable to define a symmetric stress tensor in the reference configuration^[9]. Here we define the *second Piola-Kirchhoff stress tensor* \hat{S}_s as

$$\hat{S}_s = \hat{F}_s^{-1} \hat{P}_s = \hat{J}_s \hat{F}_s^{-1} \hat{\sigma}_s \hat{F}_s^{-T} \quad \text{in } \Omega_s^0 \quad (2.28)$$

These three different stress tensors are interrelated through the fundamental measure of the deformation gradient and its determinant^[30], and in elastic materials they are all dependent on the deformation gradient \hat{F}_s ^[9;25]. In the derivation of constitutive equations in Section 2.7, both the Cauchy stress tensor σ_s and the second Piola-Kirchhoff stress tensor \hat{S}_s take simple forms because of their symmetric property.

2.6 Chemical processes

2.6.1 Convection-diffusion equation

In our model, the main chemical processes are the penetration of monocytes from the blood flow into the vessel wall, and the accumulation of foam cells which leads to plaque growth. The equations for the motion of solutes or particles are the main models for these processes. Let us denote by $c = c(x, t) : \Omega_t \times I \rightarrow \mathbb{R}$ the concentration of the species (solutes or particles) in the blood flow or the vessel wall, and it has the similar conservation law as the density and the momentum. The amount of the species in the volume $V_t \subset \Omega_t$ can be defined as

$$n(V_t) = \int_{V_t} c dx$$

The dynamical principle of cellular species gives the mathematical form as

$$\frac{d}{dt}n(V_t) = J(V_t)$$

where

$$J(V_t) = \int_{\partial V_t} D \nabla c \cdot n da$$

denotes the flux of species with the movement of *diffusion*. D is called the *diffusion coefficient*. Apply Reynolds transport theorem and divergence theorem, and we can get

$$\int_{V_t} \left\{ \frac{\partial c}{\partial t} + \text{div}(cv) \right\} dx = \frac{d}{dt} \int_{V_t} c dx = \int_{\partial V_t} D \nabla c \cdot n da = \int_{V_t} \text{div}(D \nabla c) dx$$

so the equation for the motion of species is achieved as

$$\frac{\partial c}{\partial t} + \text{div}(cv) - \text{div}(D \nabla c) = 0 \quad \text{in } \Omega_t \quad (2.29)$$

In this equation the term $\text{div}(cv)$ is called the *convection (or advection)* term, which implies that the species are transported by fluid dynamics or structural mechanics. $\text{div}(D \nabla c)$ is called the diffusion term, which implies that the species move by diffusion - the random *Brownian motion* of individual particles. So equation (2.29) is called the *convection-diffusion equation*.

(2.29) is the general form of convection-diffusion equation, and it can be simplified in special cases. If we assume that the diffusion coefficient D is constant, as the blood flow is incompressible ($\text{div}v = 0$), equation (2.29) is changed to

$$\frac{\partial c_f}{\partial t} + v_f \cdot \nabla c_f - D_f \Delta c_f = 0 \quad \text{in } \Omega_f^t \quad (2.30)$$

The convection-diffusion equation (2.30) is used to describe the motion of monocytes in the blood flow, and the lower index "f" is added to denote that the quantities and coefficients are related to fluids.

Remark 2.6.1 (Convection and diffusion flux). In the derivation of convection-diffusion equation (2.29), we can also achieve the formula

$$\int_{V_t} \frac{\partial c}{\partial t} dx = - \int_{\partial V_t} cv \cdot nda + \int_{\partial V_t} D \nabla c \cdot nda$$

which gives the fact that the change of the concentration c in V_t over time equals to the sum of two fluxes over the boundary of V_t . The first term on the right side of the formula is the flux induced by convection, and the second one is the flux induced by diffusion.

Remark 2.6.2 (Diffusion coefficient). Although the blood flow is assumed to be homogeneous, the diffusion coefficient of solutes or particles may not be constant^[48;74;75]. From recent experimental observations, it has been proposed that D_f may be dependent on the concentration of red blood cells and the *shear rate* $\dot{\gamma}$ which is defined as

$$\dot{\gamma} = \sqrt{\frac{1}{2} D(v_f) : D(v_f)}$$

where $D(v_f)$ is the strain rate tensor defined in Remark 2.4.1.

2.6.2 Convection-diffusion-reaction equation

The derivation of the equations for the motion of monocytes and foam cells in the vessel wall is similar to the convection-diffusion equation in the last subsection. The main difference is that the change of their concentrations in the volume V_t is not just due to the flux over the boundary of V_t , but also because of the chemical reaction between monocytes and foam cells. Let c and c^* denote the concentrations of monocytes and foam cells, and their amounts in the volume V_t are defined as

$$n(V_t) = \int_{V_t} c dx, \quad n^*(V_t) = \int_{V_t} c^* dx$$

Then the mathematical statement of their motion and interaction can be given as

$$\frac{d}{dt} n(V_t) = J(V_t) - r(V_t), \quad \frac{d}{dt} n^*(V_t) = r(V_t)$$

where

$$r(V_t) = \int_{V_t} f^r dx$$

implies the fact that some monocytes are converted to foam cells. $f^r = f^r(x, t) : \Omega_t \times I \rightarrow \mathbb{R}$ is called the *reaction function*, which is dependent on the concentration of monocytes c and represents a time rate of the chemical reaction between monocytes and foam cells. After taking up lipoproteins, the foam cells accumulate to lead to plaque growth and are almost fixed in the vessel wall. Their motion by diffusion is so small that it can be neglected, so there is no diffusion flux of foam cells.

Using the same way of derivation of equation (2.29), and adding the lower index "s" to denote that the quantities and coefficients are related to solids, the equations for the motion of monocytes and the accumulation of foam cells in the vessel wall are achieved as

$$\frac{\partial c_s}{\partial t} + \text{div}(c_s v_s) - \text{div}(D_s \nabla c_s) = -f_s^r \quad \text{in } \Omega_s^t \quad (2.31)$$

$$\frac{\partial c_s^*}{\partial t} + \text{div}(c_s^* v_s) = f_s^r \quad \text{in } \Omega_s^t \quad (2.32)$$

Since the plaque has different components, and its property is especially different from the healthy vessel wall, Ω_s^t is not considered as homogeneous material, so normally D_s is not constant.

Concerning the reaction function f_s^r , we assume that the rate is linear with respect to the concentration of monocytes c_s , so f_s^r is defined as

$$f_s^r = \beta c_s \quad \text{in } \Omega_s^t \quad (2.33)$$

The coefficient β may easily depend on some other quantities in chemical reactions^[17;31]. For numerical simulations of our model in the next step we set it as a constant for simplification. As the increasing rate of the concentration of foam cells c_s^* , f_s^r is also related to f_s^g , the growth rate of the mass of the vessel wall, by the fact that the accumulation of foam cells leads to plaque growth. We assume they have a linear relation as

$$f_s^g = \gamma f_s^r \quad \text{in } \Omega_s^t \quad (2.34)$$

γ is a coefficient assumed to be constant. So the chemical reaction in the vessel wall is related to the growth of its mass in a mathematical approach, which will be tested by numerical simulations in Chapter 4.

Additionally, equations (2.31) and (2.32) can also be transformed to the Lagrangian framework as (2.22). The only difficulty is the transformation of the gradient "∇" with respect to the Eulerian variables to "∇̂" with respect to the Lagrangian variables. It is obtained by the following lemma:

Lemma 2.6.1. *Let $\phi = \phi(x, t) : \Omega_t \times I \rightarrow \mathbb{R}$ be a smooth scalar function with respect to both variables x and t , and $\hat{\phi}(X, t) = \phi(x(X, t), t)$. Then*

$$\nabla\phi = \hat{F}^{-T}\hat{\nabla}\hat{\phi} \quad (2.35)$$

Proof. For the i -th ($i=1,2,\dots,d$) component of $\nabla\phi$, we can get from the definition of deformation gradient that

$$\frac{\partial\phi}{\partial x_i} = \sum_{j=1}^d \frac{\partial\hat{\phi}}{\partial X_j} \frac{\partial X_j}{\partial x_i} = \sum_{j=1}^d \frac{\partial\hat{\phi}}{\partial X_j} (\hat{F}^{-1})_{ji} = \sum_{j=1}^d (\hat{F}^{-T})_{ij} \frac{\partial\hat{\phi}}{\partial X_j}$$

so formula (2.35) is proved. □

The corresponding integral form of equation (2.31) is

$$\frac{d}{dt} \int_{V_s^t} c_s dx = \int_{\partial V_s^t} D_s \nabla c_s \cdot n da - \int_{V_s^t} f_s^r dx$$

By applying the above lemma and transformation formulas, it can be transformed to

$$\frac{\partial}{\partial t} \int_{V_s^0} \hat{c}_s \hat{J}_s dX = \int_{\partial V_s^0} \hat{D}_s \hat{F}_s^{-T} \hat{\nabla} \hat{c}_s \cdot \hat{J}_s \hat{F}_s^{-T} \cdot N dA - \int_{V_s^0} \hat{f}_s^r \hat{J}_s dX$$

So equation (2.31) in the Lagrangian framework is achieved as

$$\frac{\partial}{\partial t} (\hat{J}_s \hat{c}_s) = \widehat{div}(\hat{J}_s \hat{F}_s^{-1} \cdot \hat{D}_s \hat{F}_s^{-T} \hat{\nabla} \hat{c}_s) - \hat{J}_s \hat{f}_s^r \quad \text{in } \Omega_s^0 \quad (2.36)$$

where the diffusion coefficient $\hat{D}_s(X, t) = D_s(x(X, t), t)$ is expressed in the Lagrangian framework. Similarly equation (2.32) is transformed to

$$\frac{\partial}{\partial t} (\hat{J}_s \hat{c}_s^*) = \hat{J}_s \hat{f}_s^r \quad \text{in } \Omega_s^0 \quad (2.37)$$

2.7 Stress tensor modeling

2.7.1 Decomposition of deformation gradient

To link the stress tensor σ_s to the other quantities, the vessel wall has its relevant constitutive equations, but as a kind of solid materials, the constitutive equations differ from the ones of fluids such as incompressible flow in Section 2.4^[25]. For a solid, it is important to determine whether the behavior is elastic or not^[30], and many important aspects of the mechanical behavior of arterial tissue can be treated on the basis of elasticity theory^[27]. If the considered material is *elastic*, the Cauchy stress tensor should only be dependent on the position x and the deformation gradient F_s . And if we restrict attention to *homogeneous* materials, the Cauchy stress tensor is independent on x and has the mathematical statement as

$$\sigma = \sigma(F) \tag{2.38}$$

The lower index "s" can be removed without loss of generality. For the definition of Piola-Kirchhoff stress tensors, \hat{P} and \hat{S} also have the property of

$$\hat{P} = \hat{P}(\hat{F}), \quad \hat{S} = \hat{S}(\hat{F}) \tag{2.39}$$

In general structural mechanics, the deformation gradient is easily achieved by its definition and can be considered to measure the stress tensor. But if we are dealing with the material which is able to grow, such as the vessel wall where the plaque is formed and growing, it will be a problem to define the deformation gradient which the stress tensor is dependent on. In this case the deformation is induced both by growth and mechanics, but only the deformation induced by mechanics can contribute to the stress loading of the material. Then the whole deformation gradient is not the "F" in formula (2.38), so the general way to derive the deformation gradient is incorrect.

Figure 2.3 is a simple thought experiment to clarify this problem^[11]. Let the force N applied on the elastic rod. In mechanical equilibrium N is proportional to the observed displacement of the rod ΔL and can be calculated by measuring ΔL . However, if for some reason the same rod is able to grow, there will be some new elements formed inside the rod when it is deformed by the force N . Then the observed displacement ΔL is not proportional to N anymore and it is not appropriate for calculating N . In this case the

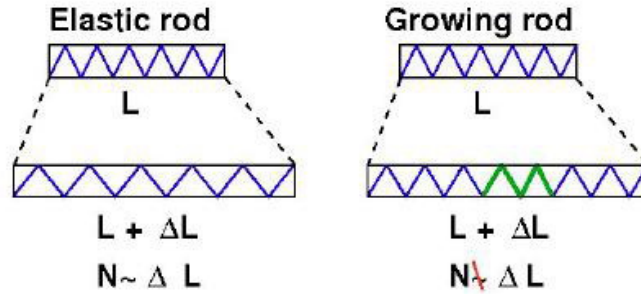


Figure 2.3: A thought experiment to show how growth may falsify the usual way of quantifying the deformation. From I. Doktorski^[11].

usual way of quantifying the deformation is falsified by growth and needs to be corrected.

To overcome this problem, we need to decompose the deformation gradient into two parts, one is induced only by growth and the other is induced only by mechanics. To get this decomposition a new configuration needs to be constructed, and the idea is based on the theory of multiple natural configurations^[49;50].

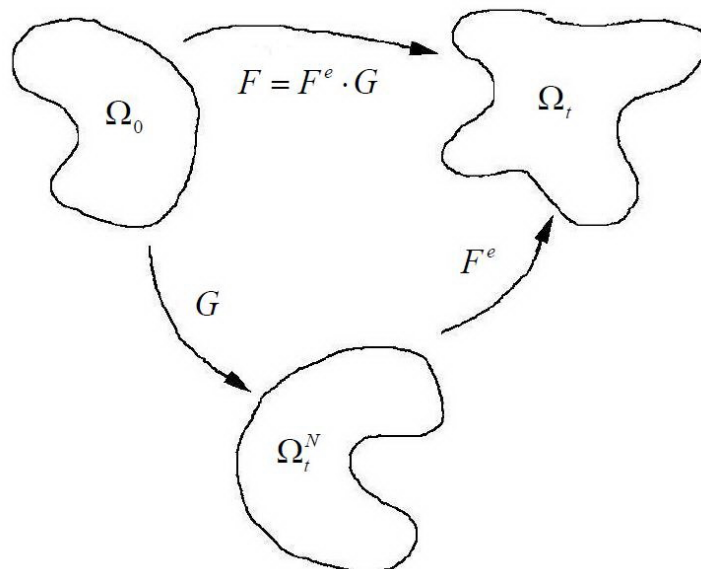


Figure 2.4: Decomposition of deformation gradient. Modified from I. Doktorski^[11].

Figure 2.4 shows how the idea of the theory of multiple natural configurations is modified to decompose the deformation gradient^[3]. According to the theory of kinematics, Ω_0 is the reference configuration and Ω_t is the current configuration. F denotes the corresponding deformation gradient. We define the *generic particles*, so that each of them occupies a volume of the differential element dX at initial time in Ω_0 . Then the mass of each generic particle is given by

$$dM = \hat{\rho}^0 dX$$

where $\hat{\rho}^0$ denotes the density at time $t = 0$. Analogously, after deformed to Ω_t , the same particle at time t has the mass of

$$dm = \rho dx$$

and occupies a volume of the differential element dx in Ω_t . If growth takes place in the deformation from Ω_0 to Ω_t , we have

$$dm > dM$$

Conversely, if resorption takes place, leading to the loss of mass, we have

$$dm < dM$$

As the reference configuration Ω_0 is deformed to the current configuration Ω_t by both growth and mechanics, each generic particle has grown and its stress value may be different from zero. Considering the current configuration, we cut the generic particle out of the body and relieve its state of stress while keeping its mass constant. Then it will reach a new state which is different from both the state in Ω_0 and the state in Ω_t . This state is called the *natural state* at time t , and the collection of all the generic particles in natural state at time t is called the *natural configuration*^[3], denoted by Ω_t^N in Figure 2.4. So Ω_0 can be considered to be deformed to Ω_t^N at first with the deformation gradient G , and then to Ω_t with the deformation gradient F^e ; the whole deformation gradient F is decomposed as

$$F = F^e G \tag{2.40}$$

Since the mass is preserved in the deformation from Ω_t^N to Ω_t , the matrix F^e is not related to growth. So it denotes the deformation induced by mechanics, and is the deformation gradient which the stress tensor is dependent on. Additionally, the matrix G is only connected to growth because the stress is at the relieved state in the deformation from Ω_0 to Ω_t^N . So it denotes the deformation induced by growth and can therefore be called the *growth matrix*. As the whole deformation gradient F is invertible, from the formula (2.40) it follows that F^e and G are also invertible. If the matrix F^e is separated from G , the stress tensor can be derived by the constitutive equations as

$$\sigma = \sigma(F^e) \quad (2.41)$$

So the rest of the work are to calculate the growth matrix G and to construct appropriate constitutive equations, which are achieved in the next two subsections.

2.7.2 Metric of growth

The decomposition of deformation gradient by introducing the natural configuration is in an ideal case, because growth and mechanics can not be simply separated^[11]. In this case the deformation from the reference configuration Ω_0 to the natural configuration Ω_t^N is only an evolution process of growth without any mechanics, so the quantities of the material, e.g. the density $\hat{\rho}^0$ is preserved, but the volume of the generic particle in Ω_0 is increasing. Let dX_N denote the volume of each generic particle in the natural configuration. Then the mass of the particle is given as

$$dM_N = \bar{\rho}^0 dX_N$$

The bar symbol is used to mark the function defined in the natural configuration. Since the mass is preserved in the deformation from the natural configuration Ω_t^N to the current configuration Ω_t , we can get

$$\rho dx = dm = dM_N = \bar{\rho}^0 dX_N$$

Let V_0 be a subdomain of Ω_0 and it is deformed to V_t^N in Ω_t^N and to V_t in Ω_t . Applying transformation formula we can get

$$\int_{V_0} \hat{\rho} \hat{J} dX = \int_{V_t} \rho dx = \int_{V_t^N} \bar{\rho}^0 dX_N = \int_{V_0} \hat{\rho}^0 \hat{J}^g dX$$

Here J^g is the determinant of the growth matrix G . Let J^e denote the determinant of the matrix F^e , and since

$$J = J^e J^g$$

from the decomposition of deformation gradient, we have

$$\hat{\rho}^0 = \hat{\rho} \hat{J}^e \quad (2.42)$$

This implies that if there is no growth in the deformation, then $J^g = 1$, and formula (2.42) is the same as the conservation equation of mass in (2.23), where the corresponding structural mechanics is also without growth. Differentiating (2.42) with respect to time we have

$$\frac{\partial \hat{\rho}}{\partial t} \hat{J}^e + \hat{\rho} \frac{\partial \hat{J}^e}{\partial t} = 0 \quad (2.43)$$

and from the conservation equation of mass (2.16), we have

$$\frac{\partial \hat{\rho}}{\partial t} \hat{J} + \hat{\rho} \frac{\partial \hat{J}}{\partial t} = \hat{J} \hat{f}^g \quad (2.44)$$

Combining (2.43) and (2.44) we obtain

$$\frac{1}{\hat{J}} \frac{\partial \hat{J}}{\partial t} - \frac{1}{\hat{J}^e} \frac{\partial \hat{J}^e}{\partial t} = \frac{\hat{f}^g}{\hat{\rho}} \quad (2.45)$$

and recalling $J = J^e J^g$ we can simplify (2.45) as

$$\frac{\partial \hat{J}^g}{\partial t} = \frac{\hat{f}^g}{\hat{\rho}} \hat{J}^g \quad (2.46)$$

Concerning the growth of plaques in the vessel wall, we assume that the growth is isotropic, which means that the plaque is growing equally in all directions. Then the growth matrix is written as

$$G = gI \quad (2.47)$$

Here $g = g(x, t) : \Omega_t \times I \rightarrow \mathbb{R}$ is a scalar function and since $J^g = g^d$ describes how the metric of the reference configuration is changed through $dX_N = \hat{J}^g dX$ during the growth process, we call g the *metric of growth*, and (2.46) is rewritten as

$$d \frac{\partial \hat{g}_s}{\partial t} = \frac{\hat{f}_s^g}{\hat{\rho}_s} \hat{g}_s \quad \text{in } \Omega_s^0 \quad (2.48)$$

Here the lower index "s" is added to denote that the metric of growth is a quantity in the solid material - the vessel wall, where the plaque is formed and growing. (2.48) is the equation for the metric of growth in the Lagrangian framework, and in the Eulerian framework it is transformed to

$$d \frac{\partial g_s}{\partial t} + dv_s \cdot \nabla g_s = \frac{f_s^g}{\rho_s} g_s \quad \text{in } \Omega_s^t \quad (2.49)$$

The equation for the metric of growth is one of the equations in our mathematical model, from which the growth matrix G_s is calculated, and the stress tensor is obtained by the constitutive equations and the matrix F_s^e defined as

$$F_s^e = F_s G_s^{-1} = \frac{1}{g_s} F_s \quad \text{in } \Omega_s^t \quad (2.50)$$

2.7.3 Constitutive equations

We assume that both the healthy vessel wall and the plaque are hyperelastic, isotropic, incompressible and homogeneous^[69;70], and the derivation of constitutive equations is based on Holzapfel's book about nonlinear solid mechanics^[25]. The *hyperelastic* material has the property that there exists a so-called *stored energy function* $\Psi = \Psi(x, F) : \Omega_s^t \times \mathbb{M}_+^d \rightarrow \mathbb{R}$, which can also be written as $\hat{\Psi} = \hat{\Psi}(X, F) : \Omega_s^0 \times \mathbb{M}_+^d \rightarrow \mathbb{R}$, such that

$$\hat{P}_s = \frac{\partial \hat{\Psi}}{\partial \hat{F}_s}(X, \hat{F}_s) \quad \text{in } \Omega_s^0 \quad (2.51)$$

and each component of the first Piola-Kirchhoff stress tensor \hat{P}_s is

$$\hat{P}_{sij} = \frac{\partial \hat{\Psi}}{\partial \hat{F}_{sij}}, \quad i, j = 1, 2, 3, \dots, d$$

Here \mathbb{M}_+^d is the set of all real matrices of order d with positive determinant. The homogeneous assumption let the stored energy function depend only on the deformation gradient, and by use of relation (2.17) between Cauchy stress tensor and first Piola-Kirchhoff stress tensor, we have

$$\sigma_s = J_s^{-1} P_s F_s^T = J_s^{-1} \frac{\partial \Psi}{\partial F_s}(F_s) F_s^T \quad \text{in } \Omega_s^t \quad (2.52)$$

From form (2.51) and (2.52) it is clear that the constitutive equations of hyperelastic materials are derived from the stored energy function. In order to illustrate Ψ we assume that it satisfies the property of *objectivity*. This means that the stored energy function is not changed after a rigid-body motion such as translation and rotation^[9;25]. The mathematical statement of this property is given as

$$\Psi(F) = \Psi(QF) \quad \forall F \in \mathbb{M}_+^d, \forall Q \in \mathbb{O}_+^d \quad (2.53)$$

where \mathbb{O}_+^d is the set of all orthogonal matrices of order d with positive determinant. From this formula we can express Ψ as a function of the *right Cauchy-Green tensor* $C_s = F_s^T F_s$, and the second Piola-Kirchhoff stress tensor is given by

$$\hat{S}_s = 2 \frac{\partial \hat{\Psi}}{\partial \hat{C}_s}(\hat{C}_s) \quad \text{in } \Omega_s^0 \quad (2.54)$$

In addition, we restrict the stored energy function by the property of *isotropy*. This property gives the physical idea that the response of the isotropic material is same in all directions^[9;25]. The corresponding mathematical statement is

$$\Psi(F) = \Psi(FQ^T) \quad \forall F \in \mathbb{M}_+^d, \forall Q \in \mathbb{O}_+^d \quad (2.55)$$

And considering Ψ as a function of the right Cauchy-Green tensor, we have

$$\Psi(C) = \Psi(QCQ^T) \quad \forall C \in \mathbb{S}_{>}^d, \forall Q \in \mathbb{O}_+^d \quad (2.56)$$

Here $\mathbb{S}_{>}^d$ is the set of all symmetric and positive definite matrices of order d . Additionally, Ψ can also be expressed as a function of the *left Cauchy-Green tensor* $B_s = F_s F_s^T$, which is proved with formulas (2.54) and (2.56)^[9;25].

As Ψ is an invariant function under a rotation according to (2.56), it can be expressed in terms of the *principal invariants* of C_s or B_s . This is a fundamental theorem for the stored energy function of isotropic hyperelastic materials, given as follows:

Theorem 2.7.1 (representation theorem for invariants). *The stored energy function Ψ satisfies (2.56) if and only if it satisfies*

$$\Psi(C) = \Psi(I_1(C), I_2(C), \dots, I_d(C)) \quad \forall C \in \mathbb{S}_>^d \quad (2.57)$$

where $I_i(C)$ is the i -th ($i=1,2,\dots,d$) principal invariant of the matrix C .

Proof. The proof of this theorem is given in literatures^[9;22]. □

From theorem 2.6.1 Ψ can be expressed by the principal invariants of the Cauchy-Green tensors C_s or B_s , which means

$$\Psi = \Psi(I_1(C_s), I_2(C_s), \dots, I_d(C_s)) = \Psi(I_1(B_s), I_2(B_s), \dots, I_d(B_s)) \quad (2.58)$$

Since C_s and B_s have the same eigenvalues, they also have the same principal invariants. So $I_i(C_s)$ and $I_i(B_s)$ can be denoted by I_i for short ($i=1,2,\dots,d$), and the stress tensor can be derived as

$$\hat{S}_s = 2 \frac{\partial \hat{\Psi}}{\partial \hat{C}_s} = 2 \sum_{i=1}^d \frac{\partial \hat{\Psi}}{\partial \hat{I}_i} \frac{\partial \hat{I}_i}{\partial \hat{C}_s} \quad (2.59)$$

If we consider $d = 3$ in special case, which is also the most important and widely-used case in continuum mechanics, the principal invariants are defined as

$$\begin{aligned} I_1 &= \text{tr}C_s \\ I_2 &= \frac{1}{2}[(\text{tr}C_s)^2 - \text{tr}C_s^2] \\ I_3 &= \det C_s \end{aligned} \quad (2.60)$$

Then by applying some theories of tensor analysis^[25], we have

$$\begin{aligned}
 \frac{\partial I_1}{\partial C_s} &= I \\
 \frac{\partial I_2}{\partial C_s} &= I_1 I - C_s \\
 \frac{\partial I_3}{\partial C_s} &= I_3 C_s^{-1}
 \end{aligned} \tag{2.61}$$

and substituting it into (2.59) we obtain

$$\hat{S}_s = 2\left[\left(\frac{\partial \hat{\Psi}}{\partial \hat{I}_1} + \hat{I}_1 \frac{\partial \hat{\Psi}}{\partial \hat{I}_2}\right)I - \frac{\partial \hat{\Psi}}{\partial \hat{I}_2} \hat{C}_s + \hat{I}_3 \frac{\partial \hat{\Psi}}{\partial \hat{I}_3} \hat{C}_s^{-1}\right] \quad \text{in } \Omega_s^0 \tag{2.62}$$

(2.62) is the general form of the second Piola-Kirchhoff stress tensor \hat{S}_s in the Lagrangian framework, with which we deduce from $\sigma_s = J_s^{-1} F_s S_s F_s^T$ that

$$\sigma_s = 2J_s^{-1}\left[I_3 \frac{\partial \Psi}{\partial I_3} I + \left(\frac{\partial \Psi}{\partial I_1} + I_1 \frac{\partial \Psi}{\partial I_2}\right)B_s - \frac{\partial \Psi}{\partial I_2} B_s^2\right] \quad \text{in } \Omega_s^t \tag{2.63}$$

Since a 3×3 matrix A has a relation with its principal invariants by the Cayley-Hamilton equations^[9;25]:

$$A^3 - I_1(A)A^2 + I_2(A)A - I_3(A)I = 0 \tag{2.64}$$

Applying (2.64) to (2.63) we can get the general form of the Cauchy stress tensor σ_s in the Eulerian framework as

$$\sigma_s = 2J_s^{-1}\left[\left(I_2 \frac{\partial \Psi}{\partial I_2} + I_3 \frac{\partial \Psi}{\partial I_3}\right)I + \frac{\partial \Psi}{\partial I_1} B_s - I_3 \frac{\partial \Psi}{\partial I_2} B_s^{-1}\right] \quad \text{in } \Omega_s^t \tag{2.65}$$

(2.62) and (2.65) are the constitutive equations we formulate. If the material is incompressible, they can get even simpler forms. As is mentioned in Section 2.4, the incompressible material keeps the volume constant throughout a motion and has the incompressibility constraint:

$$J_s = 1 \tag{2.66}$$

which is equivalent to the one of incompressible flows^[25]. Then the stored energy function is defined as

$$\Psi = -p_s(J_s - 1) + \Psi(F_s) \quad (2.67)$$

where p_s serves as an *indeterminate Lagrange multiplier* and is identified as the hydrostatic pressure^[25]. From (2.51) the corresponding first Piola-Kirchhoff stress tensor has the form

$$\hat{P}_s = -\hat{p}_s \hat{F}_s^{-T} + \frac{\partial \hat{\Psi}}{\partial \hat{F}_s}(\hat{F}_s) \quad (2.68)$$

Similarly the second Piola-Kirchhoff stress tensor and the Cauchy stress tensor are given as

$$\hat{S}_s = -\hat{p}_s \hat{C}_s^{-1} + 2 \frac{\partial \hat{\Psi}}{\partial \hat{C}_s}(\hat{C}_s) \quad (2.69)$$

$$\sigma_s = -p_s I + \frac{\partial \Psi}{\partial F_s}(F_s) F^T \quad (2.70)$$

For the case of isotropic material and $d = 3$ we have already pointed out that the stored energy function Ψ is only dependent on the principal invariants I_1 and I_2 because $I_3 = \det C_s = 1$, so

$$\Psi = -\frac{1}{2} p_s (I_3 - 1) + \Psi(I_1, I_2) \quad (2.71)$$

where $p_s/2$ serves as an indeterminate Lagrange multiplier. Combining (2.61) with (2.71) we obtain the form of the second Piola-Kirchhoff stress tensor \hat{S}_s in the Lagrangian framework as

$$\begin{aligned} \hat{S}_s &= -\hat{p}_s \frac{\partial(\hat{I}_3 - 1)}{\partial \hat{C}_s} + 2 \frac{\partial \hat{\Psi}}{\partial \hat{C}_s}(\hat{I}_1, \hat{I}_2) \\ &= -\hat{p}_s \hat{C}_s^{-1} + 2 \left(\frac{\partial \hat{\Psi}}{\partial \hat{I}_1} + \hat{I}_1 \frac{\partial \hat{\Psi}}{\partial \hat{I}_2} \right) I - 2 \frac{\partial \hat{\Psi}}{\partial \hat{I}_2} \hat{C}_s \quad \text{in } \Omega_s^0 \end{aligned} \quad (2.72)$$

By using $\sigma_s = J_s^{-1} F_s S_s F_s^T$ and (2.64), the form of the Cauchy stress tensor σ_s in the Eulerian framework is achieved corresponding to (2.63) and (2.65) as

$$\sigma_s = -p_s I + 2\left(\frac{\partial \Psi}{\partial I_1} + I_1 \frac{\partial \Psi}{\partial I_2}\right) B_s - 2 \frac{\partial \Psi}{\partial I_2} B_s^2 \quad \text{in } \Omega_s^t \quad (2.73)$$

$$\sigma_s = -p_s I + 2 \frac{\partial \Psi}{\partial I_1} B_s - 2 \frac{\partial \Psi}{\partial I_2} B_s^{-1} \quad \text{in } \Omega_s^t \quad (2.74)$$

Note that p_s in (2.73) and (2.74) differ by the term $2I_2(\partial \Psi / \partial I_2)$.

Based on (2.74), two types of useful hyperelastic materials are considered as the material of the vessel wall in our model, and the constitutive equations for them are obtained. These materials are rubber-like materials and behave similarly like the biological tissue^[34]. One of them is called the *incompressible neo-Hookean material* (INH), in which the stored energy function Ψ is only dependent on the first principal invariant I_1 ^[12;25], defined as

$$\Psi = \frac{\mu_s}{2}(I_1 - 3) \quad (2.75)$$

The coefficient μ_s is called the *shear modulus*. The other material is called the *incompressible Mooney-Rivlin material* (IMR), and its corresponding stored energy function is dependent on the principal invariants I_1 and I_2 ^[25;29], defined as

$$\Psi = C_1(I_1 - 3) + C_2(I_2 - 3) \quad (2.76)$$

The coefficients C_1 and C_2 are related to the shear modulus μ_s and satisfy

$$C_1 + C_2 = \frac{\mu_s}{2} \quad (2.77)$$

Normally μ_s , C_1 and C_2 are all constants. However, the accumulation of foam cells leads to formation of plaques, which have different mechanical properties from the healthy vessel wall. From some literatures^[28;68;70] it is shown that even though the unique stored energy function is determined in the blood vessel wall, the coefficients in the function are still different between different components. Considering the change of mechanical properties of the vessel wall due to the accumulation of foam cells, we assume that the unique stored energy function is valid in both the healthy vessel wall and the plaque, but the coefficients will be changed by the influence of foam cells. Let μ_s be an example of these coefficients and it has a general form as

$$\mu_s = \mu_{s,d} + (\mu_{s,h} - \mu_{s,d})f(c_s^*) \quad (2.78)$$

which is also used for the shear-rate-dependent viscosity in non-Newtonian fluid modeling^[7;32;60]. $\mu_{s,d}$ denotes the shear modulus in the diseased vessel wall where the plaque is formed with high concentration of foam cells, and $\mu_{s,h}$ denotes the shear modulus in the healthy vessel wall where there are no foam cells. The function f is a continuous monotonic function dependent on the concentration of foam cells c_s^* . When $c_s^* = 0$, f should satisfies $f = 1$, and $\mu_s = \mu_{s,h}$. As c_s^* is increasing, f should rapidly decrease to zero limit and μ_s is getting very close to $\mu_{s,d}$. For this purpose we define f as an exponential function and (2.78) can be written as

$$\mu_s = \mu_{s,d} + (\mu_{s,h} - \mu_{s,d})e^{-a_0 c_s^*} \quad (2.79)$$

Here $a_0 > 0$ is a constant. Similarly the coefficients C_1 and C_2 also have forms as

$$C_1 = C_{1,d} + (C_{1,h} - C_{1,d})e^{-a_1 c_s^*} \quad (2.80)$$

$$C_2 = C_{2,d} + (C_{2,h} - C_{2,d})e^{-a_2 c_s^*} \quad (2.81)$$

As we have discussed in Section 2.6 that the diffusion coefficient D_s in (2.31) is also different between the plaque and the healthy vessel wall, it can also be defined correspondingly as

$$D_s = D_{s,d} + (D_{s,h} - D_{s,d})e^{-a_3 c_s^*} \quad (2.82)$$

and a_1, a_2, a_3 are all positive constants. Substituting (2.75) and (2.76) into (2.74), we can obtain the constitutive equations of the incompressible neo-Hookean material and the incompressible Mooney-Rivlin material as

$$\sigma_s = -p_s I + \mu_s (F_s F_s^T - I) \quad (\text{INH}) \quad \text{in } \Omega_s^t \quad (2.83)$$

$$\sigma_s = -p_s I + 2C_1 F_s F_s^T - 2C_2 F_s^{-T} F_s^{-1} \quad (\text{IMR}) \quad \text{in } \Omega_s^t \quad (2.84)$$

In our model the stress tensor should only be dependent on the deformation gradient representing the deformation induced by mechanics, so we replace F_s with F_s^e in (2.83) and (2.84) to obtain

$$\sigma_s = -p_s I + \mu_s (F_s^e F_s^{eT} - I) \quad (\text{INH}) \quad \text{in } \Omega_s^t \quad (2.85)$$

$$\sigma_s = -p_s I + 2C_1 F_s^e F_s^{eT} - 2C_2 F_s^{e-T} F_s^{e-1} \quad (\text{IMR}) \quad \text{in } \Omega_s^t \quad (2.86)$$

(2.85) and (2.86) are the constitutive equations of the vessel wall in our model, and the deformation gradient F_s^e denoting the deformation of the vessel wall induced by mechanics is derived in (2.50). Combined with the constitutive equations (2.85) or (2.86), the equations for structural mechanics of the vessel wall (2.21) is finally obtained.

Remark 2.7.1 (Anisotropic materials). Sometimes the isotropic property of the material limits the applicability of its corresponding constitutive law. e.g. the arterial wall is somewhat anisotropic for the presence of fibres made of collagen, elastin and smooth muscle cells. Its behavior in the direction of the fibres will be different from the behavior in the direction transversal to the fibres^[34]. One example of the models for *anisotropic materials* is from Holzapfel et al.^[26;40], and this model is for the arterial wall with two families of fibres. Let M_s and M'_s denote the unit vectors in the direction of the fibres in the reference configuration, and if we let $d = 3$ there are some additional invariants defined as

$$\begin{aligned} I_4 &= M_s \cdot (C_s M_s), & I_5 &= M_s \cdot (C_s^2 M_s) \\ I_6 &= M'_s \cdot (C_s M'_s), & I_7 &= M'_s \cdot (C_s^2 M'_s) \\ & & I_8 &= M_s \cdot (C_s M'_s) \end{aligned} \quad (2.87)$$

Similarly to (2.58), the stored energy function Ψ is dependent on the invariants I_1, I_2, \dots, I_8 . In a special case^[26;40] it is defined as

$$\Psi = \Psi_{iso}(I_1) + \Psi_{aniso}(I_4, I_6) \quad (2.88)$$

where the isotropic term is from the incompressible neo-Hookean material as

$$\Psi_{iso}(I_1) = \frac{\mu_s}{2} (I_1 - 3) \quad (2.89)$$

and the anisotropic term is given by

$$\Psi_{aniso}(I_4, I_6) = \frac{k_1}{2k_2} \sum_{i=4,6} (e^{k_2(I_i-1)^2} - 1) \quad (2.90)$$

Similarly to the derivation of (2.83) and (2.84), the corresponding constitutive equations of this model can be derived by combining (2.89), (2.90) and (2.59).

2.8 Final model

Before formulating the whole system of our model, the appropriate initial and boundary conditions of these partial differential equations should be discussed. The most important and complicated ones are the boundary conditions on the interface $\Gamma_1^t \cup \Gamma_2^t$ of the computational domain in Figure 2.1, which is moving due to plaque growth and the fluid-structure interaction. Some quantities in the domain Ω_f^t and Ω_s^t have relations and need some *transmission conditions* on this interface. For the velocity v_f, v_s , and the stress tensor σ_f, σ_s , the *continuity of velocity* and the *balance of force* are given on the interface, such as

$$v_f = v_s, \quad \sigma_f \cdot n_f + \sigma_s \cdot n_s = 0, \quad \text{on } \Gamma_i^t, i = 1, 2 \quad (2.91)$$

Here n_f and n_s are the unit outer normal vectors of the interface $\Gamma_1^t \cup \Gamma_2^t$ with respect to Ω_f^t and Ω_s^t . These conditions are widely used in the fluid-structure interaction problem^[12;16;18;32;38;45;53;78], implying that on the interface the velocity of the blood flow and the vessel wall must coincide, and the total traction should vanish.

Concerning the penetration of monocytes from the blood flow into the vessel wall, we also need the transmission conditions of the concentration of monocytes c_f and c_s , which are given as

$$D_f \nabla c_f \cdot n_f + D_s \nabla c_s \cdot n_s = 0, \quad \text{on } \Gamma_i^t, i = 1, 2 \quad (2.92)$$

$$D_f \nabla c_f \cdot n_f + \zeta(c_f - c_s) = 0, \quad \text{on } \Gamma_i^t, i = 1, 2 \quad (2.93)$$

Here $D_f \nabla c_f \cdot n_f$ and $D_s \nabla c_s \cdot n_s$ denote the flux of monocytes in Ω_f^t and Ω_s^t . These conditions imply that the outflux of the monocytes from the blood flow equals the influx of the monocytes into the vessel wall, and this flux is related to the difference of the concentration across the interface^[48]. The coefficient ζ is a positive constant and a measure of the vessel wall *permeability* for the monocytes. So it is clear that $\zeta = 0$ on the interface of the healthy vessel wall Γ_2^t .

Most of the other boundary conditions are given as *Dirichlet boundary conditions*, e.g.

$$c_f = c_f^D, \quad \text{on } \Gamma_{f,in} \quad (2.94)$$

or *Neumann boundary conditions*, e.g.

$$\nabla c_f \cdot n_f = 0, \quad \text{on } \Gamma_{f,wall} \quad (2.95)$$

Additionally, on the outlet boundary $\Gamma_{f,out}$, we impose the *do nothing boundary conditions*:

$$\rho_f \nu \nabla v_f \cdot n_f - p_f n_f = 0, \quad \text{on } \Gamma_{f,out} \quad (2.96)$$

After obtaining the initial and boundary conditions of all the equations, we can formulate the whole system of our model. The main equations in the fluid domain $\bigcup_{0 < t \leq T} \Omega_f^t \times \{t\}$ are

$$\begin{aligned} \rho_f \frac{\partial v_f}{\partial t} + \rho_f v_f \cdot \nabla v_f - \rho_f \nu \Delta v_f + \nabla p_f &= \rho_f f_f^b \\ \operatorname{div} v_f &= 0 \\ \frac{\partial c_f}{\partial t} + v_f \cdot \nabla c_f - D_f \Delta c_f &= 0 \end{aligned} \quad (2.97)$$

including the Navier-Stokes equations (2.10) for fluid dynamics of the blood flow and the convection-diffusion equation (2.30) for the motion of monocytes. In (2.97) the velocity v_f , the pressure p_f and the concentration of monocytes c_f are the variables of the equations. We can also obtain the main equations in the solid domain $\bigcup_{0 < t \leq T} \Omega_s^t \times \{t\}$ as

$$\begin{aligned} \frac{\partial \rho_s}{\partial t} + \operatorname{div}(\rho_s v_s) &= f_s^g \\ \rho_s \frac{\partial v_s}{\partial t} + \rho_s v_s \cdot \nabla v_s &= \rho_s f_s^b + \operatorname{div} \sigma_s \\ \frac{\partial u_s}{\partial t} + v_s \cdot \nabla u_s &= v_s \\ \frac{\partial g_s}{\partial t} + dv_s \cdot \nabla g_s &= \frac{f_s^g}{\rho_s} g_s \\ \frac{\partial c_s}{\partial t} + \operatorname{div}(c_s v_s) - \operatorname{div}(D_s \nabla c_s) &= -f_s^r \\ \frac{\partial c_s^*}{\partial t} + \operatorname{div}(c_s^* v_s) &= f_s^r \end{aligned} \quad (2.98)$$

with the equations (2.13) and (2.14) for structural mechanics of the vessel wall, the equation (2.49) for the metric of growth and the equations (2.31) and (2.32) for the motion of monocytes and the accumulation of foam cells. The variables of equations (2.98) are the density ρ_s , the velocity v_s , the displacement u_s , the metric of growth g_s , the concentration of monocytes c_s and the concentration of foam cells c_s^* . From (2.33), (2.34), (2.50) (2.85) and (2.86), the growth function f_s^g , the reaction function f_s^r and the stress tensor σ_s are given as

$$\begin{aligned} f_s^g &= \gamma f_s^r, \quad f_s^r = \beta c_s \quad \text{in } \Omega_s^t \\ \sigma_s &= \begin{cases} -p_s I + \mu_s (F_s^e F_s^{eT} - I) & \text{(INH)} \\ -p_s I + 2C_1 F_s^e F_s^{eT} - 2C_2 F_s^{e-T} F_s^{e-1} & \text{(IMR)} \end{cases} \quad \text{in } \Omega_s^t \quad (2.99) \\ F_s^e &= F_s G_s^{-1} = \frac{1}{g_s} F_s \quad \text{in } \Omega_s^t \end{aligned}$$

With the corresponding initial and boundary conditions of equations (2.97) and (2.98) obtained as

$$\begin{aligned} v_f|_{t=0} &= v_f^0, \quad c_f|_{t=0} = c_f^0 \quad \text{in } \Omega_f^0 \\ v_f &= v_f^D, \quad c_f = c_f^D \quad \text{on } \Gamma_{f,in} \\ v_f &= 0, \quad \nabla c_f \cdot n_f = 0 \quad \text{on } \Gamma_{f,wall} \quad (2.100) \\ \rho_f \nu \nabla v_f \cdot n_f - p_f n_f &= 0, \quad \nabla c_f \cdot n_f = 0 \quad \text{on } \Gamma_{f,out} \end{aligned}$$

$$\begin{aligned} \rho_s|_{t=0} &= \rho_s^0, \quad g_s|_{t=0} = 1 \quad \text{in } \Omega_s^0 \\ v_s|_{t=0} &= 0, \quad u_s|_{t=0} = 0 \quad \text{in } \Omega_s^0 \\ c_s|_{t=0} &= 0, \quad c_s^*|_{t=0} = 0 \quad \text{in } \Omega_s^0 \quad (2.101) \\ v_s &= 0, \quad u_s = 0 \quad \text{on } \Gamma_{s,in} \cup \Gamma_{s,wall} \cup \Gamma_{s,out} \\ \nabla c_s \cdot n_s &= 0 \quad \text{on } \Gamma_{s,in} \cup \Gamma_{s,wall} \cup \Gamma_{s,out} \end{aligned}$$

and especially the transmission conditions on the interface $\bigcup_{0 < t \leq T} \Gamma_i^t \times \{t\}$ ($i = 1, 2$) obtained as

$$\begin{aligned} v_f &= v_s, \quad \sigma_f \cdot n_f + \sigma_s \cdot n_s = 0 \\ D_f \nabla c_f \cdot n_f + D_s \nabla c_s \cdot n_s &= 0 \quad (2.102) \\ D_f \nabla c_f \cdot n_f + \zeta(c_f - c_s) &= 0 \end{aligned}$$

our mathematical model is finally derived to describe the formation and evolution of plaques in blood vessels. Here the initial conditions of the quantities in Ω_s^0 implies the fact that in the healthy blood vessel wall there are no monocytes and foam cells, so the plaque is not formed and there is no growth of the vessel wall. Correspondingly if we want to consider the chemical reactions and structural mechanics of the vessel wall in the reference configuration, equations (2.98) can be rewritten in the solid domain $\Omega_s^0 \times [0, T]$ in the Lagrangian framework as

$$\begin{aligned}
 \frac{\partial}{\partial t}(\hat{J}_s \hat{\rho}_s) &= \hat{J}_s \hat{f}_s^g \\
 \hat{J}_s \hat{\rho}_s \frac{\partial \hat{v}_s}{\partial t} &= \hat{J}_s \hat{\rho}_s \hat{f}_s^b + \widehat{div}(\hat{J}_s \hat{\sigma}_s \hat{F}_s^{-T}) \\
 \frac{\partial \hat{u}_s}{\partial t} &= \hat{v}_s \\
 d \frac{\partial \hat{g}_s}{\partial t} &= \frac{\hat{f}_s^g}{\hat{\rho}_s} \hat{g}_s \\
 \frac{\partial}{\partial t}(\hat{J}_s \hat{c}_s) &= \widehat{div}(\hat{J}_s \hat{F}_s^{-1} \cdot D_s \hat{F}_s^{-T} \hat{\nabla} \hat{c}_s) - \hat{J}_s \hat{f}_s^r \\
 \frac{\partial}{\partial t}(\hat{J}_s \hat{c}_s^*) &= \hat{J}_s \hat{f}_s^r
 \end{aligned} \tag{2.103}$$

from equations (2.21), (2.36), (2.37) and (2.48). Here the equations for structural mechanics are written as a set of first-order equations in time instead of (2.22), so that they are in the context of fluid-structure interaction with the Navier-Stokes equations in (2.97)^[53]. If we only consider the incompressible material as the material of the vessel wall, the incompressibility constraint is obtained as

$$J_s^e = 1 \quad \text{in} \quad \Omega_s^0$$

Since $J_s = J_s^e J_s^g$, and $J_s^g = g_s^d$, the conservation equation of mass (2.16) can be written as

$$\frac{\partial}{\partial t}(\hat{J}_s \hat{\rho}_s) = \frac{\partial}{\partial t}(\hat{J}_s^g \hat{\rho}_s) = \frac{\partial}{\partial t}(\hat{g}_s^d \hat{\rho}_s) = \hat{g}_s^d \hat{f}_s^g$$

Combining the upper formula with the equation (2.48) for the metric of growth, we have

$$\frac{\partial \hat{\rho}_s}{\partial t} = 0 \quad \text{in } \Omega_s^0$$

So in this case, the density of the vessel wall $\hat{\rho}_s$ is independent on time and can be considered as a constant coefficient. The equations (2.103) in the solid domain $\Omega_s^0 \times [0, T]$ can be simplified as

$$\begin{aligned} \hat{J}_s \hat{\rho}_s \frac{\partial \hat{v}_s}{\partial t} &= \hat{J}_s \hat{\rho}_s \hat{f}_s^b + \widehat{div}(\hat{J}_s \hat{\sigma}_s \hat{F}_s^{-T}) \\ \frac{\partial \hat{u}_s}{\partial t} &= \hat{v}_s \\ d \frac{\partial \hat{g}_s}{\partial t} &= \frac{\hat{f}_s^g}{\hat{\rho}_s} \hat{g}_s \\ \frac{\partial}{\partial t}(\hat{J}_s \hat{c}_s) &= \widehat{div}(\hat{J}_s \hat{F}_s^{-1} \cdot D_s \hat{F}_s^{-T} \hat{\nabla} \hat{c}_s) - \hat{J}_s \hat{f}_s^r \\ \frac{\partial}{\partial t}(\hat{J}_s \hat{c}_s^*) &= \hat{J}_s \hat{f}_s^r \end{aligned} \tag{2.104}$$

Based on equations (2.97) and (2.104), numerical simulations are performed in the next step to show the evolution of plaque formation. The fluid dynamics of the blood flow, the structural mechanics of the incompressible vessel wall and the motion of monocytes and foam cells all contribute to these processes.

Remark 2.8.1 (Non-dimensional form of the model). To investigate our model not involving units with physical meaning, we derive the *non-dimensional forms* of equations (2.97) and (2.104). We let c_{non} be a characteristic concentration and ρ_{non} be a characteristic density. Take t_{non} as characteristic time and L as characteristic length, set $\bar{x} := x/L$, $\bar{t} := t/t_{non}$, and we can normalize all the variables in (2.97) and (2.104) as follows:

$$\begin{aligned} \bar{v}_f &= \frac{v_f t_{non}}{L}, \quad \bar{\rho}_f = \frac{\rho_f}{\rho_{non}}, \quad \bar{p}_f = \frac{p_f t_{non}^2}{L^2 \rho_{non}}, \quad \bar{c}_f = \frac{c_f}{c_{non}}, \quad \bar{u}_s = \frac{\hat{u}_s}{L}, \quad \bar{v}_s = \frac{\hat{v}_s t_{non}}{L} \\ \bar{\rho}_s &= \frac{\hat{\rho}_s}{\rho_{non}}, \quad \bar{p}_s = \frac{\hat{p}_s t_{non}^2}{L^2 \rho_{non}}, \quad \bar{g}_s = \hat{g}_s, \quad \bar{c}_s = \frac{\hat{c}_s}{c_{non}}, \quad \bar{c}_s^* = \frac{\hat{c}_s^*}{c_{non}} \end{aligned} \tag{2.105}$$

Similarly the parameters in the equations can also be normalized as

$$\begin{aligned}
 Re &= \frac{L^2}{\nu t_{non}}, \quad \bar{f}_f^b = \frac{f_f^b t_{non}^2}{L}, \quad Pe_f = \frac{L^2}{D_f t_{non}}, \quad \bar{\zeta} = \frac{\zeta t_{non}}{L}, \quad \bar{\mu}_s = \frac{\hat{\mu}_s t_{non}^2}{L^2 \rho_{non}}, \quad \bar{C}_i = \frac{\hat{C}_i t_{non}^2}{L^2 \rho_{non}}, \\
 \bar{f}_s^b &= \frac{\hat{f}_s^b t_{non}^2}{L}, \quad \hat{P}e_s = \frac{L^2}{\hat{D}_s t_{non}}, \quad \bar{\gamma} = \frac{\gamma c_{non}}{\rho_{non}}, \quad \bar{\beta} = \beta t_{non},
 \end{aligned} \tag{2.106}$$

Here Re and Pe are Reynolds number and Peclet number. Replacing the variables and parameters with the normalized ones in equations (2.97) and (2.104), and removing the characteristic quantities t_{non} , L , ρ_{non} and c_{non} , we obtain the non-dimensional form of our model without the tilde symbol as

$$\begin{aligned}
 \rho_f \frac{\partial v_f}{\partial t} + \rho_f v_f \cdot \nabla v_f - \rho_f Re^{-1} \Delta v_f + \nabla p_f &= \rho_f f_f^b \\
 \operatorname{div} v_f &= 0 \quad \text{in } \Omega_f^t/L \tag{2.107} \\
 \frac{\partial c_f}{\partial t} + v_f \cdot \nabla c_f - Pe_f^{-1} \Delta c_f &= 0
 \end{aligned}$$

$$\begin{aligned}
 \hat{J}_s \hat{\rho}_s \frac{\partial \hat{v}_s}{\partial t} &= \hat{J}_s \hat{\rho}_s \hat{f}_s^b + \widehat{\operatorname{div}}(\hat{J}_s \hat{\sigma}_s \hat{F}_s^{-T}) \\
 \frac{\partial \hat{u}_s}{\partial t} &= \hat{v}_s \\
 d \frac{\partial \hat{g}_s}{\partial t} &= \frac{\hat{f}_s^g}{\hat{\rho}_s} \hat{g}_s \quad \text{in } \Omega_s^0/L \tag{2.108} \\
 \frac{\partial}{\partial t}(\hat{J}_s \hat{c}_s) &= \widehat{\operatorname{div}}(\hat{J}_s \hat{F}_s^{-1} \cdot \hat{P}e_s^{-1} \hat{F}_s^{-T} \hat{\nabla} \hat{c}_s) - \hat{J}_s \hat{f}_s^r \\
 \frac{\partial}{\partial t}(\hat{J}_s \hat{c}_s^*) &= \hat{J}_s \hat{f}_s^r
 \end{aligned}$$

Here Ω_f^t/L and Ω_s^0/L denote the fluid and solid domains with normalized length. All the variables and parameters in the non-dimensional form (2.107) and (2.108) have no physical units. By choosing different characteristic quantities, certain variables or parameters can be measured relatively to some appropriate units, and the problem can be simplified in numerical simulations.

Chapter 3

Variational Formulation

To compute the numerical solutions of our model, the variational formulations of the whole system in both the fluid and solid domains are derived separately from equations (2.97) and (2.104) in Section 3.1. However, they are given in different frameworks, making a common solution approach challenging^[12;53;78;79]. So a new framework is introduced in Section 3.2, and the variational formulations are transformed to the same framework. Furthermore, the priori energy estimate and other theoretical results are discussed in Section 3.3, and some open questions are also stated.

Typically, the variational form in the fluid domain (blood flow) is formulated in the Eulerian framework, and the form in the solid domain (vessel wall) is given in the Lagrangian framework. Additionally, the interface between two subdomains moves because of the deformation of the solid domain. So for numerical simulations we need different meshes for both subdomains, and the meshes are also different for each time step due to the moving of the interface. The clue to treat this problem is to formulate the whole system in a common framework, in which both subdomains are fixed. We construct the widely-used arbitrary Lagrangian-Eulerian (ALE) framework so that the variational formulation of our model is transformed to the corresponding ALE formulation, and all the equations are rewritten in the fixed domain in the ALE framework. Another difference of the ALE formulation from the general one is that the displacement is defined in the whole domain. Its extension to the fluid domain is used to define the ALE mapping and has different forms by using different mesh motion techniques^[6;53;78;79].

3.1 General variational formulation

Before deriving the variational formulation, we first introduce some basic notation of the usual function spaces^[1;14]. By $\Omega \subset \mathbb{R}^d$ we denote the computational domain we are considering in general, and it has the boundary $\Gamma = \partial\Omega$. We split this boundary into $\Gamma = \Gamma^D \cup \Gamma^N$, where Γ^D represents the part of the boundary with Dirichlet boundary conditions and Γ^N represents the part of the boundary with Neumann or the other boundary conditions (e.g. do nothing boundary conditions). For the domain Ω and its boundary Γ , we indicate by $L^p(\Omega), 1 \leq p \leq \infty$ the set of all measurable functions, defined in Ω , and Lebesgue-integrable to the p-th power. $L^p(\Omega)$ is called the *Lebesgue space* and is a Banach space with the norm $\|\cdot\|_{L^p(\Omega)}$. For $p = 2$, $L^2(\Omega)$ is a Hilbert space, and the functions in $L^2(\Omega)$ or $L^2(\partial\Omega)$ are equipped with the inner products and norms as

$$\begin{aligned} (\phi, \psi)_{L^2(\Omega)} &:= \int_{\Omega} \phi\psi dx, & \|\phi\|_{L^2(\Omega)} &:= (\phi, \phi)_{L^2(\Omega)} \\ \langle \phi, \psi \rangle_{L^2(\partial\Omega)} &:= \int_{\partial\Omega} \phi\psi dx, & \|\phi\|_{L^2(\partial\Omega)} &:= \langle \phi, \phi \rangle_{L^2(\partial\Omega)} \end{aligned}$$

And without loss of generality, the inner products and norms are written as

$$\begin{aligned} (\phi, \psi)_{L^2(\Omega)} &= (\phi, \psi)_{\Omega}, & \|\phi\|_{L^2(\Omega)} &= \|\phi\|_{\Omega} \\ \langle \phi, \psi \rangle_{L^2(\partial\Omega)} &= \langle \phi, \psi \rangle_{\partial\Omega}, & \|\phi\|_{L^2(\partial\Omega)} &= \|\phi\|_{\partial\Omega} \end{aligned}$$

The *Sobolev space* $W^{m,p}(\Omega), m \in \mathbb{N}, 1 \leq p \leq \infty$ is defined as a set of functions in $L^p(\Omega)$, having weak derivatives of order up to m , which belong to $L^p(\Omega)$. And we indicate the set of functions in $W^{m,p}(\Omega)$ with zero trace on $\partial\Omega$ by $W_0^{m,p}(\Omega)$. For $p = 2$, $H^m(\Omega) := W^{m,2}(\Omega)$ is a Hilbert space with the norm $\|\cdot\|_{H^m(\Omega)}$. Specifically, for the functions in $H^1(\Omega)$ with zero trace only on $\Gamma^D \subset \partial\Omega$, and the functions in $L^2(\Omega)$ with a constant difference, we introduce the following function spaces:

$$\begin{aligned} H_0^1(\Omega; \Gamma^D) &= \{\phi \in H^1(\Omega) : \phi = 0 \text{ on } \Gamma^D\} \\ L_0^2(\Omega) &= \{\phi \in L^2(\Omega) : (\phi, 1)_{\Omega} = 0\} \end{aligned}$$

Finally, for the time dependent functions, we define the Lebesgue and Sobolev spaces involving time, in which the functions map time into Banach spaces^[14].

3.1. GENERAL VARIATIONAL FORMULATION

One example of these spaces is $L^2[I; X]$, where $I = [0, T]$ denotes the time interval and X denotes a real Banach space with the norm $\|\cdot\|_X$. It has the norm as

$$\|\phi\|_{L^2[I; X]} := \left(\int_0^T \|\phi\|_X^2 dt \right)^{1/2}$$

Based on the function spaces defined above, the variational formulations of our model are obtained from the equations and the initial-boundary conditions derived in Chapter 2. We multiply equations (2.97) with some test functions and take the integrals in Ω_f^t , and the weak formulation of the equations in the fluid domain is derived as follows:

Problem 3.1.1 (Variational formulation of the equations in the fluid domain). *In Ω_f^t , find $v_f \in v_f^D + L^2[I; V_f^v]$, $p_f \in L^2[I; L_f^p]$, and $c_f \in c_f^D + L^2[I; V_f^c]$, such that $v_f|_{t=0} = v_f^0$, $c_f|_{t=0} = c_f^0$, and*

$$\begin{aligned} & (\rho_f \left(\frac{\partial v_f}{\partial t} + v_f \cdot \nabla v_f \right), \psi_f^v)_{\Omega_f^t} + (\sigma_f, \nabla \psi_f^v)_{\Omega_f^t} - (\rho_f f_f^b, \psi_f^v)_{\Omega_f^t} \\ & \quad + \langle g_f^{int}, \psi_f^v \rangle_{\Gamma_1^t \cup \Gamma_2^t} - \langle g_f^{out}, \psi_f^v \rangle_{\Gamma_{f,out}} = 0 \quad \forall \psi_f^v \in V_f^v \\ & \quad (div v_f, \psi_f^p)_{\Omega_f^t} = 0 \quad \forall \psi_f^p \in L_f^p \quad (3.1) \\ & \left(\frac{\partial c_f}{\partial t} + v_f \cdot \nabla c_f, \psi_f^c \right)_{\Omega_f^t} + (D_f \nabla c_f, \nabla \psi_f^c)_{\Omega_f^t} \\ & \quad + \langle g_f^c, \psi_f^c \rangle_{\Gamma_1^t \cup \Gamma_2^t} = 0 \quad \forall \psi_f^c \in V_f^c \end{aligned}$$

with the stress tensor

$$\sigma_f = -p_f I + \rho_f \nu (\nabla v_f + \nabla v_f^T) \quad \text{in } \Omega_f^t \quad (3.2)$$

the boundary terms

$$\begin{aligned} g_f^{int} &= \sigma_s \cdot n_s \quad \text{on } \Gamma_1^t \cup \Gamma_2^t \\ g_f^{out} &= \rho_f \nu \nabla v_f^T \cdot n_f \quad \text{on } \Gamma_{f,out} \\ g_f^c &= \zeta (c_f - c_s) \quad \text{on } \Gamma_1^t \cup \Gamma_2^t \end{aligned} \quad (3.3)$$

and the function spaces

$$\begin{aligned} V_f^v &:= H_0^1(\Omega_f^t; \Gamma_{f,in} \cup \Gamma_{f,wall})^d, & L_f^p &:= L^2(\Omega_f^t) \\ V_f^c &:= H_0^1(\Omega_f^t; \Gamma_{f,in}) \end{aligned} \quad (3.4)$$

Here the boundary terms g_f^{out} , g_f^{int} and g_f^c are obtained from boundary conditions (2.100) and (2.102). v_f^D and c_f^D are suitable extensions of the Dirichlet boundary data of v_f and c_f . If $\Gamma^D = \partial\Omega_f^t$ for the velocity v_f , which implies that the Dirichlet boundary conditions of v_f are given on the whole boundary of Ω_f^t , the pressure p_f and the test function ψ_f^p should belong to the function space $L_f^0 := L_0^2(\Omega_f^t)$ [55;56]. In Problem 3.1.1, $\Gamma^D = \Gamma_{f,in} \cup \Gamma_{f,wall}$ for v_f , so p_f and ψ_f^p still belong to L_f^p defined in (3.4). For the existence of the time derivative of some variables in variational formulation (3.1), these variables have more regularities as

$$\frac{\partial v_f}{\partial t} \in L^2[I; (V_f^v)^*], \quad \frac{\partial c_f}{\partial t} \in L^2[I; (V_f^c)^*]$$

Here the spaces $(V_f^v)^*$ and $(V_f^c)^*$ denote the dual spaces of V_f^v and V_f^c . To derive the weak formulation of the equations in the solid domain, we multiply equations (2.104) in the Lagrangian framework with test functions and take the integrals in Ω_s^0 . Since the Dirichlet boundary values of v_s and u_s are both equal to zero in (2.101), the extensions of their Dirichlet boundary data are also zero.

Problem 3.1.2 (Variational formulation of the equations in the solid domain). *In Ω_s^0 , find $\hat{v}_s \in L^2[I; \hat{L}_s^v]$, $\hat{u}_s \in L^2[I; \hat{V}_s^u]$, $\hat{p}_s \in L^2[I; \hat{L}_s^p]$, $\hat{g}_s \in L^2[I; \hat{L}_s^g]$, $\hat{c}_s \in L^2[I; \hat{V}_s^c]$, and $\hat{c}_s^* \in L^2[I; \hat{L}_s^{c*}]$, such that $\hat{v}_s|_{t=0} = 0$, $\hat{u}_s|_{t=0} = 0$, $\hat{g}_s|_{t=0} = 1$, $\hat{c}_s|_{t=0} = 0$, $\hat{c}_s^*|_{t=0} = 0$, and*

$$\begin{aligned} & (\hat{J}_s \hat{\rho}_s \frac{\partial \hat{v}_s}{\partial t}, \hat{\psi}_s^v)_{\Omega_s^0} + (\hat{J}_s \hat{\sigma}_s \hat{F}_s^{-T}, \hat{\nabla} \hat{\psi}_s^v)_{\Omega_s^0} \\ & - (\hat{J}_s \hat{\rho}_s \hat{f}_s^b, \hat{\psi}_s^v)_{\Omega_s^0} + \langle \hat{g}_s^{int}, \hat{\psi}_s^v \rangle_{\Gamma_1^0 \cup \Gamma_2^0} = 0 \quad \forall \hat{\psi}_s^v \in \hat{V}_s^v \\ & \left(\frac{\partial \hat{u}_s}{\partial t} - \hat{v}_s, \hat{\psi}_s^u \right)_{\Omega_s^0} = 0 \quad \forall \hat{\psi}_s^u \in \hat{L}_s^u \\ & (\hat{J}_s^c - 1, \hat{\psi}_s^p)_{\Omega_s^0} = 0 \quad \forall \hat{\psi}_s^p \in \hat{L}_s^p \\ & (d\hat{\rho}_s \frac{\partial \hat{g}_s}{\partial t}, \hat{\psi}_s^g)_{\Omega_s^0} - (\hat{f}_s^g \hat{g}_s, \hat{\psi}_s^g)_{\Omega_s^0} = 0 \quad \forall \hat{\psi}_s^g \in \hat{L}_s^g \quad (3.5) \\ & \left(\frac{\partial}{\partial t} (\hat{J}_s \hat{c}_s), \hat{\psi}_s^c \right)_{\Omega_s^0} + (\hat{J}_s \hat{D}_s \hat{F}_s^{-T} \hat{\nabla} \hat{c}_s, \hat{F}_s^{-T} \hat{\nabla} \hat{\psi}_s^c)_{\Omega_s^0} \\ & + (\hat{J}_s \hat{f}_s^r, \hat{\psi}_s^c)_{\Omega_s^0} + \langle \hat{g}_s^c, \hat{\psi}_s^c \rangle_{\Gamma_1^0 \cup \Gamma_2^0} = 0 \quad \forall \hat{\psi}_s^c \in \hat{V}_s^c \\ & \left(\frac{\partial}{\partial t} (\hat{J}_s \hat{c}_s^*), \hat{\psi}_s^{c*} \right)_{\Omega_s^0} - (\hat{J}_s \hat{f}_s^r, \hat{\psi}_s^{c*})_{\Omega_s^0} = 0 \quad \forall \hat{\psi}_s^{c*} \in \hat{L}_s^{c*} \end{aligned}$$

with the stress tensor

3.1. GENERAL VARIATIONAL FORMULATION

$$\begin{aligned} \hat{\sigma}_s &= \begin{cases} -\hat{p}_s I + \hat{\mu}_s (\hat{F}_s^e \hat{F}_s^{eT} - I) & (INH) \\ -\hat{p}_s I + 2\hat{C}_1 \hat{F}_s^e \hat{F}_s^{eT} - 2\hat{C}_2 \hat{F}_s^{e-T} \hat{F}_s^{e-1} & (IMR) \end{cases} \quad \text{in } \Omega_s^0 \quad (3.6) \\ \hat{F}_s^e &= \hat{F}_s \hat{G}_s^{-1} = \frac{1}{\hat{g}_s} \hat{F}_s \quad \text{in } \Omega_s^0 \end{aligned}$$

the growth and reaction functions

$$\hat{f}_s^g = \gamma \hat{f}_s^r, \quad \hat{f}_s^r = \beta \hat{c}_s \quad \text{in } \Omega_s^0 \quad (3.7)$$

the boundary terms

$$\begin{aligned} \hat{g}_s^{int} &= \hat{J}_f \hat{\sigma}_f \hat{F}_f^{-T} \cdot N_f \quad \text{on } \Gamma_1^0 \cup \Gamma_2^0 \\ \hat{g}_s^c &= \zeta (\hat{c}_s - \hat{c}_f) \hat{J}_s | \hat{F}_s^{-T} \cdot N_s | \quad \text{on } \Gamma_1^0 \cup \Gamma_2^0 \end{aligned} \quad (3.8)$$

and the function spaces

$$\begin{aligned} \hat{V}_s^v = \hat{V}_s^u &:= H_0^1(\Omega_s^0; \Gamma_{s,in} \cup \Gamma_{s,wall} \cup \Gamma_{s,out})^d, \quad \hat{L}_s^v = \hat{L}_s^u := L^2(\Omega_s^0)^d \\ \hat{L}_s^p = \hat{L}_s^g = \hat{L}_s^{c*} &:= L^2(\Omega_s^0), \quad \hat{V}_s^c := H^1(\Omega_s^0) \end{aligned} \quad (3.9)$$

The boundary terms \hat{g}_s^{int} and \hat{g}_s^c are transformed to the Lagrangian framework by using transformation formulas (2.24) and (2.25). Similarly, if $\Gamma^D = \partial\Omega_s^0$ for the velocity \hat{v}_s , the pressure \hat{p}_s and the test function $\hat{\psi}_s^p$ should belong to the function space $\hat{L}_s^0 := L_0^2(\Omega_s^0)$. And the variables with time derivatives in variational formulation (3.5) have more regularities as

$$\begin{aligned} \frac{\partial \hat{v}_s}{\partial t} &\in L^2[I; (\hat{V}_s^v)^*], \quad \frac{\partial \hat{c}_s}{\partial t} \in L^2[I; (\hat{V}_s^c)^*] \\ \frac{\partial \hat{u}_s}{\partial t} &\in L^2[I; L^2(\Omega_s^0)^d], \quad \frac{\partial \hat{g}_s}{\partial t}, \frac{\partial \hat{c}_s^*}{\partial t} \in L^2[I; L^2(\Omega_s^0)] \end{aligned}$$

Additionally, the coefficients \hat{D}_s , $\hat{\mu}_s$, \hat{C}_1 and \hat{C}_2 are expressed in the Lagrangian framework and written as

$$\begin{aligned} \hat{D}_s &= D_{s,d} + (D_{s,h} - D_{s,d}) e^{-a_3 \hat{c}_s^*} \\ \hat{\mu}_s &= \mu_{s,d} + (\mu_{s,h} - \mu_{s,d}) e^{-a_0 \hat{c}_s^*} \\ \hat{C}_1 &= C_{1,d} + (C_{1,h} - C_{1,d}) e^{-a_1 \hat{c}_s^*} \\ \hat{C}_2 &= C_{2,d} + (C_{2,h} - C_{2,d}) e^{-a_2 \hat{c}_s^*} \end{aligned}$$

Coupling (3.1) and (3.5) with transmission conditions (2.102), we can get a first version of the variational formulation of the whole system in both the fluid and solid domains.

Problem 3.1.3 (Variational formulation of the whole system). *Find $v_f \in v_f^D + L^2[I; V_f^v]$, $p_f \in L^2[I; L_f^p]$, $c_f \in c_f^D + L^2[I; V_f^c]$, $\hat{v}_s \in L^2[I; \hat{L}_s^v]$, $\hat{u}_s \in L^2[I; \hat{V}_s^u]$, $\hat{p}_s \in L^2[I; \hat{L}_s^p]$, $\hat{g}_s \in L^2[I; \hat{L}_s^g]$, $\hat{c}_s \in L^2[I; \hat{V}_s^c]$, and $\hat{c}_s^* \in L^2[I; \hat{L}_s^{c*}]$, such that (3.1), (3.5) and (2.102) are fulfilled for all the suitable test functions defined in Problem 3.1.1 and Problem 3.1.2, and the relevant initial conditions are also satisfied.*

To solve problem 3.1.3 by numerical simulations, there are some difficulties^[53]. First, variational form (3.1) is formulated in the Eulerian framework, and form (3.5) is formulated in the Lagrangian framework. The domain Ω_f^t is moving, while Ω_s^0 is fixed. So for numerical simulations we need different meshes for both subdomains. Second, transmission conditions (2.102) are formulated on a common interface. But since the variational formulations in different domains are in different frameworks, the boundary terms are not on a common interface either. So we need to express both conditions in one framework, e.g. the continuity of velocity written as

$$\hat{v}_s(X) = \hat{v}_f(X) = v_f(X + \hat{u}_s) \quad \text{on} \quad \Gamma_1^0 \cup \Gamma_2^0$$

However, the point $x = X + \hat{u}_s$ may not be a mesh point in the fluid domain, so the transmission conditions can not be fulfilled exactly. For the balance of force we also need to transform the tensors to the same framework by using Piola transformation formula (2.19). Finally, as the interface between two subdomains is moving because of the deformation of the solid domain, the domain partitioning is also changing in each time step $t_n \rightarrow t_{n+1}$ when we use finite difference schemes for temporal discretization in the next chapter. We thus need different meshes at the beginning and the end of each time step.

The clue to treat this problem is to formulate the whole system in a common framework, in which both subdomains are fixed. In the following section we introduce the *arbitrary Lagrangian-Eulerian* (ALE) framework for the equations in the fluid domain, so that variational formulation (3.1) will be transformed to the corresponding ALE formulation. This new form is expressed on the fixed domain Ω_f^0 which matches the solid domain Ω_s^0 for all time steps.

3.2 Variational formulation in the ALE framework

3.2.1 ALE formulation in the fluid domain

The main problem of the numerical difficulties listed above is the moving domain Ω_f^t , so the ideal situation to solve this problem is to formulate Problem 3.1.1 in a fixed domain Ω_f^0 , and a mapping between Ω_f^0 and the moving domain Ω_f^t needs to be given. This mapping can not be the deformation defined in Section 2.3 for kinematics of continuum media, because the inlet $\Gamma_{f,in}$ and the outlet $\Gamma_{f,out}$ can not be kept at the same spatial location under this mapping^[45]. We only wish to consider the fluid domain in the area of interest, following the movement of the wall interface, not to follow the evolution of the blood particles as they circulate along the whole cardiovascular system^[44]. We thus construct the widely-used arbitrary Lagrangian-Eulerian (ALE) framework, in which the fluid domain Ω_f^0 is arbitrary, and the solid domain Ω_s^0 is in the Lagrangian framework. The corresponding mapping is called the arbitrary Lagrangian-Eulerian (ALE) mapping.

The ALE mapping $\hat{\mathcal{A}}(X, t)$ is defined similarly as the deformation for kinematics in Section 2.3:

$$\hat{\mathcal{A}} : \Omega_0 \times I \rightarrow \Omega_t, \quad (X, t) \mapsto x = \hat{\mathcal{A}}(X, t)$$

We also assume that $\hat{\mathcal{A}}$ is a smooth one-to-one mapping with respect to X in the so-called ALE reference configuration Ω_0 and is differentiable almost everywhere with respect to t in the time interval I . In the solid domain Ω_s^0 , $\hat{\mathcal{A}}$ is formulated in the same way as the deformation for kinematics, so the displacement \hat{u}_s has the relation with $\hat{\mathcal{A}}$ as

$$\hat{u}_s(X, t) = \hat{\mathcal{A}}(X, t) - X, \quad X \in \Omega_s^0, t \in I$$

In the fluid domain Ω_f^0 , we also define the displacement variable as

$$\hat{u}_f(X, t) = \hat{\mathcal{A}}(X, t) - X, \quad X \in \Omega_f^0, t \in I$$

This artificial variable has no physical meaning and is not the displacement of the material particle anymore. Similarly the gradient of the ALE mapping and its determinant in Ω_f^0 are also defined as

$$\hat{F}_f = \hat{\nabla} \hat{\mathcal{A}} = I + \hat{\nabla} \hat{u}_f, \quad \hat{J}_f = \det \hat{F}_f$$

In a similar way as Section 2.3, for any function $\phi(x, t)$ defined in Ω_f^t we have its definition in Ω_f^0 as

$$\hat{\phi}(X, t) = \phi(\hat{\mathcal{A}}(X, t), t), \quad X \in \Omega_f^0, t \in I$$

Additionally, the time derivative of the ALE mapping is

$$\frac{\partial \hat{\mathcal{A}}}{\partial t}(X, t) = \frac{\partial \hat{u}_f}{\partial t}(X, t), \quad X \in \Omega_f^0, t \in I$$

which is not equal to the velocity \hat{v}_f in general, because this variable \hat{u}_f is not a displacement in the sense that it fits to the velocity any more.

Based on the ALE mapping we can transform variational formulation (3.1) to a new one in the ALE framework, which is called the ALE formulation. For the derivation, the transformation formulas of the time derivative " $\frac{\partial}{\partial t}$ " and the spatial gradient " ∇ " are given in the following lemma:

Lemma 3.2.1 (Derivatives of the ALE mapping). *$\hat{\mathcal{A}}$ is the ALE mapping. Let $\phi = \phi(x, t) : \Omega_f^t \times I \rightarrow \mathbb{R}$ be a differentiable scalar function and $\varphi = \varphi(x, t) : \Omega_f^t \times I \rightarrow \mathbb{R}^d$ a differentiable vector function with respect to both variables x and t . $\hat{\phi}(X, t) = \phi(\hat{\mathcal{A}}(X, t), t)$ and $\hat{\varphi}(X, t) = \varphi(\hat{\mathcal{A}}(X, t), t)$. Then*

$$\frac{\partial \phi}{\partial t} = \frac{\partial \hat{\phi}}{\partial t} - \hat{F}_f^{-1} \frac{\partial \hat{u}_f}{\partial t} \cdot \hat{\nabla} \hat{\phi} \quad (3.10)$$

$$\nabla \phi = \hat{F}_f^{-T} \hat{\nabla} \hat{\phi} \quad (3.11)$$

$$\nabla \varphi = \hat{\nabla} \hat{\varphi} \hat{F}_f^{-1} \quad (3.12)$$

$$\varphi \cdot \nabla \phi = \hat{F}_f^{-1} \hat{\varphi} \cdot \hat{\nabla} \hat{\phi} \quad (3.13)$$

Proof. Since $\hat{\mathcal{A}}$ is a homeomorphism, it has the inverse mapping as $\hat{\mathcal{A}}^{-1}(x, t) = X$. For the time derivative $\frac{\partial}{\partial t} \phi(x, t)$ we get with the chain rule that

$$\frac{\partial \phi}{\partial t} = \frac{\partial}{\partial t} \phi(x, t) = \frac{\partial}{\partial t} \hat{\phi}(\hat{\mathcal{A}}^{-1}(x, t), t) = \frac{\partial \hat{\phi}}{\partial t} + \frac{\partial \hat{\mathcal{A}}^{-1}}{\partial t} \cdot \hat{\nabla} \hat{\phi} \quad (3.14)$$

3.2. VARIATIONAL FORMULATION IN THE ALE FRAMEWORK

For the inverse of the ALE mapping it holds by differentiating

$$\begin{aligned}\hat{\mathcal{A}} \circ \hat{\mathcal{A}}^{-1} = id \Rightarrow 0 &= \frac{\partial}{\partial t} \hat{\mathcal{A}}(\hat{\mathcal{A}}^{-1}(x, t), t) = \frac{\partial \hat{\mathcal{A}}}{\partial t} + \hat{\nabla} \hat{\mathcal{A}} \frac{\partial \hat{\mathcal{A}}^{-1}}{\partial t} \\ &\Rightarrow \frac{\partial \hat{\mathcal{A}}^{-1}}{\partial t} = -\hat{\nabla} \hat{\mathcal{A}}^{-1} \frac{\partial \hat{\mathcal{A}}}{\partial t} = -\hat{F}_f^{-1} \frac{\partial \hat{u}_f}{\partial t}\end{aligned}\quad (3.15)$$

Combining (3.14) and (3.15), we derive the first formula (3.10). The second formula (3.11) is proved in the same way as the proof of (2.35) in Lemma 2.6.1, and (3.12) follows by applying (3.11) to the components of φ and by noting that $\nabla \varphi$ is given by the row-vector $\nabla \varphi_i^T$ ($i=1,2,\dots,d$). For the last formula (3.13) we get

$$\begin{aligned}\varphi \cdot \nabla \phi &= \sum_{i=1}^d \varphi_i \frac{\partial \phi}{\partial x_i} = \sum_{i,j=1}^d \hat{\varphi}_i \frac{\partial \hat{\phi}}{\partial X_j} \frac{\partial X_j}{\partial x_i} = \sum_{i,j=1}^d \hat{\varphi}_i \frac{\partial \hat{\phi}}{\partial X_j} (\hat{F}_f^{-1})_{ji} \\ &= \sum_{j=1}^d (\hat{F}_f^{-1} \hat{\varphi})_j \frac{\partial \hat{\phi}}{\partial X_j} = \hat{F}_f^{-1} \hat{\varphi} \cdot \hat{\nabla} \hat{\phi}\end{aligned}$$

□

Now the ALE formulation of the equations in the fixed domain Ω_f^0 can be derived. Considering the divergence term, we use transformation formulas (2.2) and (3.11) to get

$$\begin{aligned}(\operatorname{div} v_f, \psi_f^p)_{\Omega_f^t} &= \int_{\Omega_f^t} \operatorname{div} v_f \psi_f^p dx = \int_{\partial \Omega_f^t} v_f \psi_f^p \cdot n_f da - \int_{\Omega_f^t} v_f \cdot \nabla \psi_f^p dx \\ &= \int_{\partial \Omega_f^0} \hat{v}_f \hat{\psi}_f^p \cdot \hat{J}_f \hat{F}_f^{-T} \cdot N_f dA - \int_{\Omega_f^0} \hat{v}_f \cdot \hat{F}_f^{-T} \hat{\nabla} \hat{\psi}_f^p \hat{J}_f dX \\ &= \int_{\partial \Omega_f^0} \hat{J}_f \hat{F}_f^{-1} \hat{v}_f \hat{\psi}_f^p \cdot N_f dA - \int_{\Omega_f^0} \hat{J}_f \hat{F}_f^{-1} \hat{v}_f \cdot \hat{\nabla} \hat{\psi}_f^p dX \\ &= \int_{\Omega_f^0} \widehat{\operatorname{div}}(\hat{J}_f \hat{F}_f^{-1} \hat{v}_f) \hat{\psi}_f^p dX = (\widehat{\operatorname{div}}(\hat{J}_f \hat{F}_f^{-1} \hat{v}_f), \hat{\psi}_f^p)_{\Omega_f^0}\end{aligned}$$

The time derivative terms and the convection terms are transformed by using (2.1), (3.10) and (3.13) and we get

$$\begin{aligned}
 (\rho_f \frac{\partial v_f}{\partial t}, \psi_f^v)_{\Omega_f^t} &= (\hat{J}_f \hat{\rho}_f \frac{\partial \hat{v}_f}{\partial t}, \hat{\psi}_f^v)_{\Omega_f^0} - (\hat{J}_f \hat{\rho}_f \hat{F}_f^{-1} \frac{\partial \hat{u}_f}{\partial t} \cdot \hat{\nabla} \hat{v}_f, \hat{\psi}_f^v)_{\Omega_f^0} \\
 (\frac{\partial c_f}{\partial t}, \psi_f^c)_{\Omega_f^t} &= (\hat{J}_f \frac{\partial \hat{c}_f}{\partial t}, \hat{\psi}_f^c)_{\Omega_f^0} - (\hat{J}_f \hat{F}_f^{-1} \frac{\partial \hat{u}_f}{\partial t} \cdot \hat{\nabla} \hat{c}_f, \hat{\psi}_f^c)_{\Omega_f^0} \\
 (\rho_f v_f \cdot \nabla v_f, \psi_f^v)_{\Omega_f^t} &= (\hat{J}_f \hat{\rho}_f \hat{F}_f^{-1} \hat{v}_f \cdot \hat{\nabla} \hat{v}_f, \hat{\psi}_f^v)_{\Omega_f^0} \\
 (v_f \cdot \nabla c_f, \psi_f^c)_{\Omega_f^t} &= (\hat{J}_f \hat{F}_f^{-1} \hat{v}_f \cdot \hat{\nabla} \hat{c}_f, \hat{\psi}_f^c)_{\Omega_f^0}
 \end{aligned}$$

The body force term is easily transformed as

$$(\rho_f f_f^b, \psi_f^v)_{\Omega_f^t} = (\hat{J}_f \hat{\rho}_f \hat{f}_f^b, \hat{\psi}_f^v)_{\Omega_f^0}$$

Finally by using (3.11) and (3.12) the viscous term and the diffusion term are transformed as

$$\begin{aligned}
 (\sigma_f, \nabla \psi_f^v)_{\Omega_f^t} &= (\hat{J}_f \hat{\sigma}_f, \hat{\nabla} \hat{\psi}_f^v \hat{F}_f^{-1})_{\Omega_f^0} = (\hat{J}_f \hat{\sigma}_f \hat{F}_f^{-T}, \hat{\nabla} \hat{\psi}_f^v)_{\Omega_f^0} \\
 (D_f \nabla c_f, \nabla \psi_f^c)_{\Omega_f^t} &= (\hat{J}_f D_f \hat{F}_f^{-T} \hat{\nabla} \hat{c}_f, \hat{F}_f^{-T} \hat{\nabla} \hat{\psi}_f^c)_{\Omega_f^0}
 \end{aligned}$$

where the stress tensor $\hat{\sigma}_f$ is written as

$$\hat{\sigma}_f = -\hat{p}_f I + \hat{\rho}_f \nu (\hat{\nabla} \hat{v}_f \hat{F}_f^{-1} + \hat{F}_f^{-T} \hat{\nabla} \hat{v}_f^T)$$

Then the complete ALE formulation in Ω_f^0 is obtained in the following problem:

Problem 3.2.1 (ALE formulation of the equations in the fixed fluid domain). *In Ω_f^0 , find $\hat{v}_f \in \hat{V}_f^D + L^2[I; \hat{V}_f^v]$, $\hat{p}_f \in L^2[I; \hat{L}_f^p]$, and $\hat{c}_f \in \hat{c}_f^D + L^2[I; \hat{V}_f^c]$, such that $\hat{v}_f|_{t=0} = \hat{v}_f^0$, $\hat{c}_f|_{t=0} = \hat{c}_f^0$, and*

$$\begin{aligned}
 (\hat{J}_f \hat{\rho}_f \frac{\partial \hat{v}_f}{\partial t}, \hat{\psi}_f^v)_{\Omega_f^0} + (\hat{J}_f \hat{\rho}_f \hat{F}_f^{-1} (\hat{v}_f - \frac{\partial \hat{u}_f}{\partial t}) \cdot \hat{\nabla} \hat{v}_f, \hat{\psi}_f^v)_{\Omega_f^0} &+ (\hat{J}_f \hat{\sigma}_f \hat{F}_f^{-T}, \hat{\nabla} \hat{\psi}_f^v)_{\Omega_f^0} \\
 - (\hat{J}_f \hat{\rho}_f \hat{f}_f^b, \hat{\psi}_f^v)_{\Omega_f^0} + \langle \hat{g}_f^{int}, \hat{\psi}_f^v \rangle_{\Gamma_1^0 \cup \Gamma_2^0} - \langle \hat{g}_f^{out}, \hat{\psi}_f^v \rangle_{\Gamma_{f,out}} &= 0 \quad \forall \hat{\psi}_f^v \in \hat{V}_f^v \\
 (\widehat{div}(\hat{J}_f \hat{F}_f^{-1} \hat{v}_f), \hat{\psi}_f^p)_{\Omega_f^0} &= 0 \quad \forall \hat{\psi}_f^p \in \hat{L}_f^p \quad (3.16) \\
 (\hat{J}_f \frac{\partial \hat{c}_f}{\partial t}, \hat{\psi}_f^c)_{\Omega_f^0} + (\hat{J}_f \hat{F}_f^{-1} (\hat{v}_f - \frac{\partial \hat{u}_f}{\partial t}) \cdot \hat{\nabla} \hat{c}_f, \hat{\psi}_f^c)_{\Omega_f^0} \\
 + (\hat{J}_f D_f \hat{F}_f^{-T} \hat{\nabla} \hat{c}_f, \hat{F}_f^{-T} \hat{\nabla} \hat{\psi}_f^c)_{\Omega_f^0} + \langle \hat{g}_f^c, \hat{\psi}_f^c \rangle_{\Gamma_1^0 \cup \Gamma_2^0} &= 0 \quad \forall \hat{\psi}_f^c \in \hat{V}_f^c
 \end{aligned}$$

3.2. VARIATIONAL FORMULATION IN THE ALE FRAMEWORK

with the stress tensor

$$\hat{\sigma}_f = -\hat{p}_f I + \hat{\rho}_f \nu (\hat{\nabla} \hat{v}_f \hat{F}_f^{-1} + \hat{F}_f^{-T} \hat{\nabla} \hat{v}_f^T) \quad \text{in } \Omega_f^0 \quad (3.17)$$

the boundary terms

$$\begin{aligned} \hat{g}_f^{int} &= \hat{J}_s \hat{\sigma}_s \hat{F}_s^{-T} \cdot N_s & \text{on } \Gamma_1^0 \cup \Gamma_2^0 \\ \hat{g}_f^{out} &= \hat{J}_f \hat{\rho}_f \nu \hat{F}_f^{-T} \hat{\nabla} \hat{v}_f^T \hat{F}_f^{-T} \cdot N_f & \text{on } \Gamma_{f,out} \\ \hat{g}_f^c &= \zeta (\hat{c}_f - \hat{c}_s) \hat{J}_f |\hat{F}_f^{-T} \cdot N_f| & \text{on } \Gamma_1^0 \cup \Gamma_2^0 \end{aligned} \quad (3.18)$$

and the function spaces

$$\begin{aligned} \hat{V}_f^v &:= H_0^1(\Omega_f^0; \Gamma_{f,in} \cup \Gamma_{f,wall})^d, & \hat{L}_f^p &:= L^2(\Omega_f^0) \\ \hat{V}_f^c &:= H_0^1(\Omega_f^0; \Gamma_{f,in}) \end{aligned} \quad (3.19)$$

The boundary terms \hat{g}_f^{int} , \hat{g}_f^{out} and \hat{g}_f^c are transformed to the ALE framework by using transformation formulas (2.24), (2.25) and (3.12), and the variables with time derivatives in variational formulation (3.16) have more regularities as

$$\frac{\partial \hat{v}_f}{\partial t} \in L^2[I; (\hat{V}_f^v)^*], \quad \frac{\partial \hat{c}_f}{\partial t} \in L^2[I; (\hat{V}_f^c)^*]$$

Since the ALE formulation in Ω_s^0 is in the Lagrangian framework, it is same as variational formulation (3.5). If we couple (3.5) with (3.16) as the variational formulation of the whole system, they are both formulated in the ALE framework. Both the fluid domain Ω_f^0 and the solid one Ω_s^0 are fixed, and the interface $\Gamma_1^0 \cup \Gamma_2^0$ does not move anymore. So transmission conditions (2.102) are on a common interface, formulated as

$$\begin{aligned} \hat{v}_f &= \hat{v}_s, & \hat{J}_f \hat{\sigma}_f \hat{F}_f^{-T} \cdot N_f + \hat{J}_s \hat{\sigma}_s \hat{F}_s^{-T} \cdot N_s &= 0 \\ \hat{J}_f D_f \hat{F}_f^{-T} \hat{\nabla} \hat{c}_f \hat{F}_f^{-T} \cdot N_f + \hat{J}_s \hat{D}_s \hat{F}_s^{-T} \hat{\nabla} \hat{c}_s \hat{F}_s^{-T} \cdot N_s &= 0 \\ \hat{J}_f D_f \hat{F}_f^{-T} \hat{\nabla} \hat{c}_f \hat{F}_f^{-T} \cdot N_f + \zeta (\hat{c}_f - \hat{c}_s) \hat{J}_f |\hat{F}_f^{-T} \cdot N_f| &= 0 \end{aligned} \quad (3.20)$$

In general, the function spaces of the variables in Problem 3.2.1 are not given as (3.19) but should be defined as

$$\begin{aligned}\hat{V}_f^v &:= \{\hat{v}_f(\cdot, t) : \Omega_f^0 \rightarrow \mathbb{R}^d \mid \hat{v}_f(\cdot, t) = v_f \circ \hat{\mathcal{A}}(\cdot, t), v_f \in V_f^v, t \in I\} \\ \hat{L}_f^p &:= \{\hat{p}_f(\cdot, t) : \Omega_f^0 \rightarrow \mathbb{R}^d \mid \hat{p}_f(\cdot, t) = p_f \circ \hat{\mathcal{A}}(\cdot, t), p_f \in L_f^p, t \in I\} \\ \hat{V}_f^c &:= \{\hat{c}_f(\cdot, t) : \Omega_f^0 \rightarrow \mathbb{R}^d \mid \hat{c}_f(\cdot, t) = c_f \circ \hat{\mathcal{A}}(\cdot, t), c_f \in V_f^c, t \in I\}\end{aligned}$$

To let (3.19) be admissible we need more conditions for the regularity of the ALE mapping^[78], which address the following problem:

Problem 3.2.2 (Conditions for the regularity of the ALE mapping). *The ALE mapping $\hat{\mathcal{A}}$ needs sufficient conditions so that $\phi \in H^1(\Omega_t)$ if and only if $\hat{\phi} = \phi \circ \hat{\mathcal{A}} \in H^1(\Omega_0)$.*

Classical results of function spaces indicate that a sufficient condition of Problem 3.2.2 is that

$$\hat{\mathcal{A}} \in C^1(\overline{\Omega_0}), \quad \hat{\mathcal{A}}^{-1} \in C^1(\overline{\Omega_t})$$

and

$$\hat{F} = \hat{\nabla} \hat{\mathcal{A}} \in L^\infty(\Omega_0), \quad F^{-1} = \nabla \hat{\mathcal{A}}^{-1} \in L^\infty(\Omega_t)$$

In fact, this requirement is too restrictive and the ALE mapping is not necessarily in $C^1(\overline{\Omega_0})$, because a finite element space discretization is used to reconstruct the ALE mapping^[19;39]. So it is possible to relax the above requirements by the following lemmas:

Lemma 3.2.2 (Spatial regularity of the ALE mapping). *Let Ω_0 be a bounded domain with Lipschitz continuous boundary and let $\hat{\mathcal{A}}$ be invertible in $\overline{\Omega_0}$ and satisfy the following conditions for each $t \in I$:*

- Ω_t is bounded and $\partial\Omega_t$ is Lipschitz continuous.
- $\hat{\mathcal{A}} \in W^{1,\infty}(\Omega_0)$ and $\hat{\mathcal{A}}^{-1} \in W^{1,\infty}(\Omega_t)$

Then $\phi \in H^1(\Omega_t)$ if and only if $\hat{\phi} = \phi \circ \hat{\mathcal{A}} \in H^1(\Omega_0)$. Moreover, the norm $\|\cdot\|_{H^1(\Omega_0)}$ is equivalent to $\|\cdot\|_{H^1(\Omega_t)}$.

Proof. The proof of this lemma is given in literatures^[19;39]. □

3.2. VARIATIONAL FORMULATION IN THE ALE FRAMEWORK

Lemma 3.2.3 (Temporal regularity of the ALE mapping). *Let us assume that $\hat{\mathcal{A}}(X, t) \in H^1[I; W^{1,\infty}(\Omega_0)]$. If $\hat{\phi} \in H^1[I; H^1(\Omega_0)]$, then $\phi = \hat{\phi} \circ \hat{\mathcal{A}}^{-1} \in H^1[I; H^1(\Omega_t)]$ and the ALE time-derivative of ϕ has the regularity result as*

$$\frac{\partial}{\partial t} \Big|_{\hat{\mathcal{A}}} \phi := \frac{\partial \phi}{\partial t} + w \cdot \nabla \phi \in L^2[I; H^1(\Omega_t)]$$

with the domain velocity defined as $w(x, t) = \hat{w}(\hat{\mathcal{A}}^{-1}(x, t), t)$ and

$$\hat{w}(X, t) := \frac{\partial \hat{\mathcal{A}}}{\partial t}(X, t), \quad X \in \Omega_0, t \in I$$

Proof. The proof of this lemma is given in literatures^[19;39]. □

Here we simply assume that the required regularity of the ALE mapping in the above two lemmas are given, and then the definition of function spaces in (3.19) is admissible for the ALE formulation (3.16).

3.2.2 Construction of the ALE mapping

In this section, we focus our attention on the construction of the ALE mapping in the fluid domain Ω_f^0 , which is obtained in terms of the displacement variable \hat{u}_f , and should have the following properties^[53]:

1. The mapping $\hat{\mathcal{A}}$ must be bijective and has the inverse mapping $\hat{\mathcal{A}}^{-1}$.
2. The displacement of the fluid domain should follow the motion of the interface, which means the transmission condition

$$\hat{u}_f = \hat{u}_s, \quad \text{on } \Gamma_1^0 \cup \Gamma_2^0$$

3. The transformation should be orientation preserving, which means the determinant of the deformation gradient

$$\hat{J}_f = \det \hat{F}_f > 0$$

or most preferable $\hat{J}_f \sim 1$.

In the fluid domain Ω_f^0 , the construction of the ALE mapping is arbitrary and it is described by means of an artificial partial differential equation to be solved:

$$\mathcal{L}(\hat{u}_f) = 0 \text{ in } \Omega_f^0, \quad \hat{u}_f = \hat{u}_s \text{ on } \Gamma_1^0 \cup \Gamma_2^0, \quad \hat{u}_f = 0 \text{ on } \partial\Omega_f^0/(\Gamma_1^0 \cup \Gamma_2^0) \quad (3.21)$$

From this equation we produce a smooth evolution of the fluid mesh, and the ALE mapping is given as a new variable in the whole system. The differential operator \mathcal{L} should be defined in such a way that the solution \hat{u}_f is as smooth as possible. In the following, we will discuss three possible partial differential equations with the style of (3.21).

The harmonic model

The first simple model is to consider the Laplace equation to get a *harmonic extension* of \hat{u}_s to \hat{u}_f in the fluid domain. The general formulation is written as

$$\begin{aligned} \widehat{div}(\alpha_u \hat{\nabla} \hat{u}_f) = 0 \quad & \text{in } \Omega_f^0, \quad \hat{u}_f = \hat{u}_s \quad \text{on } \Gamma_1^0 \cup \Gamma_2^0, \\ \hat{u}_f = 0 \quad & \text{on } \partial\Omega_f^0/(\Gamma_1^0 \cup \Gamma_2^0) \end{aligned} \quad (3.22)$$

Here the extension parameter α_u is chosen in such a way that a good fluid mesh quality is guaranteed. In our model, the interface is under a large deformation because of plaque formation and growth, so the fluid mesh near $\Gamma_1^0 \cup \Gamma_2^0$ is easy to get broken if the deformation is at a critical value. One simple way to solve this problem is to divide the parameter α_u by the determinant of the ALE mapping^[6;65;72], then the parameter is given as

$$\alpha_u = \alpha_u^0 / \hat{J}_f \quad (3.23)$$

This choice will avoid the mesh distortion in the vicinity of $\Gamma_1^0 \cup \Gamma_2^0$, because $\hat{J}_f \rightarrow 0$ near $\Gamma_1^0 \cup \Gamma_2^0$ if the deformation increases for plaque growth. With the definition (3.23) of the parameter, $\alpha_u \gg 0$ near $\Gamma_1^0 \cup \Gamma_2^0$, so the quality of the fluid mesh is maintained.

Specifically, we assume that the computational domain Figure 2.1 is in two-dimensional space. The inlet and outlet boundaries $\Gamma_{f,in}$ and $\Gamma_{f,out}$ is assumed to be parallel to the y-axis, and the boundary $\Gamma_{f,wall}$ is assumed to be parallel to the x-axis. We write the components of \hat{u}_f in x- and y-directions as

$$\hat{u}_f = (\hat{u}_f^{(x)}, \hat{u}_f^{(y)})$$

3.2. VARIATIONAL FORMULATION IN THE ALE FRAMEWORK

Then the boundary conditions for equations (3.22) can also be given as

$$\begin{aligned}\hat{u}_f^{(x)} &= \hat{\nabla} \hat{u}_f^{(y)} \cdot N_f = 0 \quad \text{on } \Gamma_{f,in} \cup \Gamma_{f,out} \\ \hat{u}_f^{(y)} &= \hat{\nabla} \hat{u}_f^{(x)} \cdot N_f = 0 \quad \text{on } \Gamma_{f,wall}\end{aligned}\tag{3.24}$$

which implies that the mesh is left free to move in the tangential direction of the boundary $\partial\Omega_f^0/(\Gamma_1^0 \cup \Gamma_2^0)$. This effect can reduce mesh cell distortion because only the component of \hat{u}_f in the perpendicular direction of the boundary is constrained to zero^[78;79].

The biharmonic model

Another model for large deformation is to use the *biharmonic equation*, in which an artificial parameter α_u is also used to control the mesh motion as before. This equation is written as

$$\begin{aligned}\hat{\eta}_f &= -\hat{\Delta} \hat{u}_f \quad \text{and} \quad -\alpha_u \hat{\Delta} \hat{\eta}_f = 0 \quad \text{in } \Omega_f^0 \\ & \quad \quad \quad -\alpha_u \hat{\Delta} \hat{\eta}_s = 0 \quad \text{in } \Omega_s^0\end{aligned}\tag{3.25}$$

with the boundary conditions

$$\hat{u}_f = \hat{\eta}_f = 0 \quad \text{on } \partial\Omega_f^0/(\Gamma_1^0 \cup \Gamma_2^0)\tag{3.26}$$

$$\hat{u}_f = \hat{u}_s \quad \text{and} \quad \hat{\eta}_f = \hat{\eta}_s \quad \text{on } \Gamma_1^0 \cup \Gamma_2^0\tag{3.27}$$

Similarly, if we consider the same case as boundary conditions (3.24), equations (3.25) can also have the boundary condition as

$$\begin{aligned}\hat{u}_f^{(x)} &= \hat{\nabla} \hat{u}_f^{(y)} \cdot N_f = 0 \quad \text{and} \quad \hat{\eta}_f^{(x)} = \hat{\nabla} \hat{\eta}_f^{(y)} \cdot N_f = 0 \quad \text{on } \Gamma_{f,in} \cup \Gamma_{f,out} \\ \hat{u}_f^{(y)} &= \hat{\nabla} \hat{u}_f^{(x)} \cdot N_f = 0 \quad \text{and} \quad \hat{\eta}_f^{(y)} = \hat{\nabla} \hat{\eta}_f^{(x)} \cdot N_f = 0 \quad \text{on } \Gamma_{f,wall}\end{aligned}\tag{3.28}$$

Additionally, the biharmonic model does not require a careful choice of the parameter α_u , so we simply choose a small constant $\alpha_u > 0$ as the parameter^[78].

The linear elastic model

The third model to define the ALE mapping is the *linear elastic equation*, based on the conservation equations of momentum in a steady state. The equations and boundary conditions are written as

$$\begin{aligned} \widehat{\operatorname{div}}(\hat{\sigma}_{mesh}) = 0 \quad & \text{in } \Omega_f^0, \quad \hat{u}_f = \hat{u}_s \quad \text{on } \Gamma_1^0 \cup \Gamma_2^0, \\ \hat{u}_f = 0 \quad & \text{on } \partial\Omega_f^0 / (\Gamma_1^0 \cup \Gamma_2^0) \end{aligned} \quad (3.29)$$

where $\hat{\sigma}_{mesh}$ is formally equivalent to the constitutive equations of STVK material^[78;79], given by

$$\hat{\sigma}_{mesh} := \alpha_\lambda(\operatorname{tr}\hat{\epsilon})I + 2\alpha_\mu\hat{\epsilon} \quad (3.30)$$

The parameters α_λ and α_μ are determined by the Poisson ratio and the Young modulus in elastic materials^[9;78;79], and the tensor $\hat{\epsilon} = \frac{1}{2}(\hat{\nabla}\hat{u}_f + \hat{\nabla}\hat{u}_f^T)$ is the linearized version of the strain tensor. To preserve the fluid mesh quality under a large deformation, the elastic coefficients can also be divided by the determinant of the ALE mapping^[6;65;72]. And a negative Poisson ration is used, such that compression to the fluid mesh will lead to compression in the perpendicular direction, which is also a useful property for the evolution of the fluid mesh^[53;78].

3.2.3 Final ALE formulation

In this section we can finally state the variational formulation of the whole system in the ALE framework. Typically, the variational form in the solid domain is formulated in the Lagrangian framework, and the form in the fluid domain is formulated in the ALE framework. All the equations of the whole system are rewritten in the fixed domain Ω_f^0 or Ω_s^0 with the fixed interface $\Gamma_1^0 \cup \Gamma_2^0$. As we introduce in the last section, there are different forms for the definition of the displacement \hat{u}_f , which obtains the construction of the ALE mapping. Here we consider harmonic extension from (3.22) and (3.23), and obtain its variational formulation as

$$(\alpha_u \hat{\nabla}\hat{u}_f, \hat{\nabla}\hat{\psi}_f^u)_{\Omega_f^0} = 0 \quad \forall \hat{\psi}_f^u \in \hat{V}_f^u := H_0^1(\Omega_f^0)^d \quad (3.31)$$

For the definition of the velocity, displacement and pressure, we search for the variables \hat{v} , \hat{u} and \hat{p} , such that their local quantities satisfy

3.2. VARIATIONAL FORMULATION IN THE ALE FRAMEWORK

$$\hat{v}|_{\Omega_f^0} = \hat{v}_f, \quad \hat{v}|_{\Omega_s^0} = \hat{v}_s, \quad \hat{u}|_{\Omega_f^0} = \hat{u}_f, \quad \hat{u}|_{\Omega_s^0} = \hat{u}_s, \quad \hat{p}|_{\Omega_f^0} = \hat{p}_f, \quad \hat{p}|_{\Omega_s^0} = \hat{p}_s$$

The continuity conditions $\hat{v}_f = \hat{v}_s$ and $\hat{u}_f = \hat{u}_s$ on $\Gamma_1^0 \cup \Gamma_2^0$ should be included in the definition of the function spaces of \hat{v} and \hat{u} . However the definition of \hat{v} is not well-posed, as $\hat{v}_s \in L^2[I; \hat{L}_s^v]$ does not have a regular $H^{\frac{1}{2}}$ trace as $\hat{v}_f \in \hat{v}_f^D + L^2[I; \hat{V}_f^v]$ has on $\Gamma_1^0 \cup \Gamma_2^0$ [32;55]. To guarantee the required regularity we need to add a damping term [55;78] and in the following we assume that $\hat{v}_s \in L^2[I; \hat{V}_s^v]$. Then the velocity $\hat{v} \in \hat{v}^D + L^2[I; \hat{V}^v]$ can be constructed, and $\hat{V}^v := H_0^1(\Omega_f^0 \cup \Omega_s^0; \partial\Omega_f^0/\Gamma_{f,out})^d$. Similarly the test functions $\hat{\psi}_f^v \in \hat{V}_f^v$ and $\hat{\psi}_s^v \in \hat{V}_s^v$ can also be coupled as one function $\hat{\psi}^v \in \hat{V}^v$, such that

$$\hat{\psi}^v|_{\Omega_f^0} = \hat{\psi}_f^v, \quad \hat{\psi}^v|_{\Omega_s^0} = \hat{\psi}_s^v$$

Considering the harmonic extension for defining \hat{u}_f in (3.31), both $\hat{u}_f \in \hat{V}_f^u$ and $\hat{u}_s \in \hat{V}_s^u$ are given with at least H^1 -regularity [55] and we define the coupled variable \hat{u} as

$$\hat{u} \in L^2[I; \hat{V}^u], \quad \hat{V}^u := H_0^1(\Omega_f^0 \cup \Omega_s^0)^d$$

With the definition of \hat{u} we can also construct the ALE mapping $\hat{\mathcal{A}}$ as

$$\hat{\mathcal{A}}(X, t) = X + \hat{u}(X, t), \quad X \in \Omega_f^0 \cup \Omega_s^0, t \in I \quad (3.32)$$

and further define its gradient and determinant as

$$\hat{F} = \hat{\nabla} \hat{\mathcal{A}} = I + \hat{\nabla} \hat{u}, \quad \hat{J} = \det \hat{F}$$

which satisfies

$$\hat{F}|_{\Omega_f^0} = \hat{F}_f, \quad \hat{F}|_{\Omega_s^0} = \hat{F}_s, \quad \hat{J}|_{\Omega_f^0} = \hat{J}_f, \quad \hat{J}|_{\Omega_s^0} = \hat{J}_s$$

For the variable of pressure, $\hat{p} \in L^2[I; \hat{L}^p]$ can be easily defined since $\hat{p}_f \in L^2[I; \hat{L}_f^p]$ and $\hat{p}_s \in L^2[I; \hat{L}_s^p]$. Combine variational formulations (3.5) and (3.16) with harmonic extension form (3.31), we can finally obtain the ALE formulation of the whole system as follows:

Problem 3.2.3 (ALE formulation of the whole system). *In $\Omega_f^0 \cup \Omega_s^0$, find $\hat{v} \in \hat{v}^D + L^2[I; \hat{V}^v]$, $\hat{u} \in L^2[I; \hat{V}^u]$, $\hat{p} \in L^2[I; \hat{L}^p]$, $\hat{g}_s \in L^2[I; \hat{L}_s^g]$, $\hat{c}_f \in \hat{c}_f^D + L^2[I; \hat{V}_f^c]$, $\hat{c}_s \in L^2[I; \hat{V}_s^c]$, and $\hat{c}_s^* \in L^2[I; \hat{L}_s^{c*}]$, such that $\hat{v}|_{\Omega_f^0, t=0} = \hat{v}_f^0$, $\hat{c}_f|_{t=0} = \hat{c}_f^0$, $\hat{v}|_{\Omega_s^0, t=0} = 0$, $\hat{u}|_{\Omega_s^0, t=0} = 0$, $\hat{g}_s|_{t=0} = 1$, $\hat{c}_s|_{t=0} = 0$, $\hat{c}_s^*|_{t=0} = 0$, and*

$$\begin{aligned}
 & (\hat{J}\hat{\rho}_f \frac{\partial \hat{v}}{\partial t}, \hat{\psi}^v)_{\Omega_f^0} + (\hat{J}\hat{\rho}_f \hat{F}^{-1}(\hat{v} - \frac{\partial \hat{u}}{\partial t}) \cdot \hat{\nabla} \hat{v}, \hat{\psi}^v)_{\Omega_f^0} + (\hat{J}\hat{\rho}_s \frac{\partial \hat{v}}{\partial t}, \hat{\psi}^v)_{\Omega_s^0} \\
 & \quad (\hat{J}\hat{\sigma}_f \hat{F}^{-T}, \hat{\nabla} \hat{\psi}^v)_{\Omega_f^0} + (\hat{J}\hat{\sigma}_s \hat{F}^{-T}, \hat{\nabla} \hat{\psi}^v)_{\Omega_s^0} - \langle \hat{g}_f^{out}, \hat{\psi}^v \rangle_{\Gamma_{f,out}} \\
 & \quad - (\hat{J}\hat{\rho}_f \hat{f}_f^b, \hat{\psi}^v)_{\Omega_f^0} - (\hat{J}\hat{\rho}_s \hat{f}_s^b, \hat{\psi}^v)_{\Omega_s^0} = 0 \quad \forall \hat{\psi}^v \in \hat{V}^v \\
 & \quad (\alpha_u \hat{\nabla} \hat{u}, \hat{\nabla} \hat{\psi}_f^u)_{\Omega_f^0} = 0 \quad \forall \hat{\psi}_f^u \in \hat{V}_f^u \\
 & \quad (\frac{\partial \hat{u}}{\partial t} - \hat{v}, \hat{\psi}_s^u)_{\Omega_s^0} = 0 \quad \forall \hat{\psi}_s^u \in \hat{L}_s^u \\
 & \quad (\widehat{div}(\hat{J}\hat{F}^{-1}\hat{v}), \hat{\psi}_f^p)_{\Omega_f^0} = 0 \quad \forall \hat{\psi}_f^p \in \hat{L}_f^p \\
 & \quad (\hat{J}_s^e - 1, \hat{\psi}_s^p)_{\Omega_s^0} = 0 \quad \forall \hat{\psi}_s^p \in \hat{L}_s^p \quad (3.33) \\
 & \quad (d\hat{\rho}_s \frac{\partial \hat{g}_s}{\partial t}, \hat{\psi}_s^g)_{\Omega_s^0} - (\hat{f}_s^g \hat{g}_s, \hat{\psi}_s^g)_{\Omega_s^0} = 0 \quad \forall \hat{\psi}_s^g \in \hat{L}_s^g \\
 & \quad (\hat{J} \frac{\partial \hat{c}_f}{\partial t}, \hat{\psi}_f^c)_{\Omega_f^0} + (\hat{J}\hat{F}^{-1}(\hat{v} - \frac{\partial \hat{u}}{\partial t}) \cdot \hat{\nabla} \hat{c}_f, \hat{\psi}_f^c)_{\Omega_f^0} \\
 & \quad + (\hat{J}D_f \hat{F}^{-T} \hat{\nabla} \hat{c}_f, \hat{F}^{-T} \hat{\nabla} \hat{\psi}_f^c)_{\Omega_f^0} + \langle \hat{g}_f^c, \hat{\psi}_f^c \rangle_{\Gamma_1^0 \cup \Gamma_2^0} = 0 \quad \forall \hat{\psi}_f^c \in \hat{V}_f^c \\
 & \quad (\frac{\partial}{\partial t}(\hat{J}\hat{c}_s), \hat{\psi}_s^c)_{\Omega_s^0} + (\hat{J}\hat{D}_s \hat{F}^{-T} \hat{\nabla} \hat{c}_s, \hat{F}^{-T} \hat{\nabla} \hat{\psi}_s^c)_{\Omega_s^0} \\
 & \quad + (\hat{J}\hat{f}_s^r, \hat{\psi}_s^c)_{\Omega_s^0} + \langle \hat{g}_s^c, \hat{\psi}_s^c \rangle_{\Gamma_1^0 \cup \Gamma_2^0} = 0 \quad \forall \hat{\psi}_s^c \in \hat{V}_s^c \\
 & \quad (\frac{\partial}{\partial t}(\hat{J}\hat{c}_s^*), \hat{\psi}_s^{c*})_{\Omega_s^0} - (\hat{J}\hat{f}_s^r, \hat{\psi}_s^{c*})_{\Omega_s^0} = 0 \quad \forall \hat{\psi}_s^{c*} \in \hat{L}_s^{c*}
 \end{aligned}$$

with the stress tensor

$$\begin{aligned}
 \hat{\sigma}_f &= -\hat{p}I + \hat{\rho}_f \nu (\hat{\nabla} \hat{v} \hat{F}^{-1} + \hat{F}^{-T} \hat{\nabla} \hat{v}^T) \quad in \quad \Omega_f^0 \\
 \hat{\sigma}_s &= \begin{cases} -\hat{p}I + \hat{\mu}_s (\hat{F}_s^e \hat{F}_s^{eT} - I) & (INH) \\ -\hat{p}I + 2\hat{C}_1 \hat{F}_s^e \hat{F}_s^{eT} - 2\hat{C}_2 \hat{F}_s^{e-T} \hat{F}_s^{e-1} & (IMR) \end{cases} \quad in \quad \Omega_s^0 \quad (3.34) \\
 \hat{F}_s^e &= \hat{F} \hat{G}_s^{-1} = \frac{1}{\hat{g}_s} \hat{F} \quad in \quad \Omega_s^0
 \end{aligned}$$

the growth and reaction functions

$$\hat{f}_s^g = \gamma \hat{f}_s^r, \quad \hat{f}_s^r = \beta \hat{c}_s \quad in \quad \Omega_s^0 \quad (3.35)$$

3.2. VARIATIONAL FORMULATION IN THE ALE FRAMEWORK

the boundary terms

$$\hat{g}_f^{out} = \hat{J} \hat{\rho}_f \nu \hat{F}^{-T} \hat{\nabla} \hat{v}^T \hat{F}^{-T} \cdot N_f \quad \text{on } \Gamma_{f,out} \quad (3.36)$$

$$\hat{g}_f^c = \zeta(\hat{c}_f - \hat{c}_s) \hat{J} |\hat{F}^{-T} \cdot N_f| \quad \text{on } \Gamma_1^0 \cup \Gamma_2^0 \quad (3.37)$$

$$\hat{g}_s^c = \zeta(\hat{c}_s - \hat{c}_f) \hat{J} |\hat{F}^{-T} \cdot N_s| \quad \text{on } \Gamma_1^0 \cup \Gamma_2^0 \quad (3.38)$$

and the function spaces

$$\begin{aligned} \hat{V}^v &:= H_0^1(\Omega_f^0 \cup \Omega_s^0; \partial\Omega_f^0/\Gamma_{f,out})^d, & \hat{L}^p &:= L^2(\Omega_f^0 \cup \Omega_s^0) \\ \hat{V}^u &:= H_0^1(\Omega_f^0 \cup \Omega_s^0)^d, & \hat{V}_f^c &:= H_0^1(\Omega_f^0; \Gamma_{f,in}) \\ \hat{V}_s^c &:= H^1(\Omega_s^0), & \hat{L}_f^p &:= L^2(\Omega_f^0) \\ \hat{L}_s^p = \hat{L}_s^g = \hat{L}_s^{c*} &:= L^2(\Omega_s^0), & \hat{L}_s^u &:= L^2(\Omega_s^0)^d \\ \hat{V}_f^u &:= H_0^1(\Omega_f^0)^d, \end{aligned} \quad (3.39)$$

For transmission conditions (2.91) the boundary terms of the stress tensors $\hat{\sigma}_f$ and $\hat{\sigma}_s$ vanish as

$$\langle \hat{J}_f \hat{\sigma}_f \hat{F}_f^{-T} \cdot N_f, \hat{\psi}^v \rangle_{\Gamma_1^0 \cup \Gamma_2^0} + \langle \hat{J}_s \hat{\sigma}_s \hat{F}_s^{-T} \cdot N_s, \hat{\psi}^v \rangle_{\Gamma_1^0 \cup \Gamma_2^0} = 0 \quad \forall \hat{\psi}^v \in \hat{V}^v \quad (3.40)$$

And similarly the variables with time derivatives in variational formulation (3.33) have more regularities as they have in Problem 3.1.2 and Problem 3.2.1.

Remark 3.2.1 (ALE formulation of the whole system with the biharmonic mesh model). To maintain the quality of the fluid mesh in a better way, we can also use biharmonic extension for \hat{u}_f and obtain the ALE formulation of the whole system with the biharmonic mesh model. An artificial variable $\hat{\eta}$ is defined by equations (3.25) in Ω_f^0 and by harmonic extension in Ω_s^0 , and the ALE formulation is

$$\begin{aligned} (\hat{J} \hat{\rho}_f \frac{\partial \hat{v}}{\partial t}, \hat{\psi}^v)_{\Omega_f^0} + (\hat{J} \hat{\rho}_f \hat{F}_f^{-1} (\hat{v} - \frac{\partial \hat{u}}{\partial t}) \cdot \hat{\nabla} \hat{v}, \hat{\psi}^v)_{\Omega_f^0} &+ (\hat{J} \hat{\rho}_s \frac{\partial \hat{v}}{\partial t}, \hat{\psi}^v)_{\Omega_s^0} \\ (\hat{J} \hat{\sigma}_f \hat{F}_f^{-T}, \hat{\nabla} \hat{\psi}^v)_{\Omega_f^0} + (\hat{J} \hat{\sigma}_s \hat{F}_s^{-T}, \hat{\nabla} \hat{\psi}^v)_{\Omega_s^0} &- \langle \hat{g}_f^{out}, \hat{\psi}^v \rangle_{\Gamma_{f,out}} \\ - (\hat{J} \hat{\rho}_f \hat{f}_f^b, \hat{\psi}^v)_{\Omega_f^0} - (\hat{J} \hat{\rho}_s \hat{f}_s^b, \hat{\psi}^v)_{\Omega_s^0} &= 0 \quad \forall \hat{\psi}^v \in \hat{V}^v \end{aligned}$$

$$\begin{aligned}
 (\alpha_u \hat{\nabla} \hat{\eta}, \hat{\nabla} \hat{\psi}_f^u)_{\Omega_f^0} &= 0 \quad \forall \hat{\psi}_f^u \in \hat{V}_f^u \\
 \left(\frac{\partial \hat{u}}{\partial t} - \hat{v}, \hat{\psi}_s^u \right)_{\Omega_s^0} &= 0 \quad \forall \hat{\psi}_s^u \in \hat{L}_s^u \\
 -(\hat{\eta}, \hat{\psi}_f^\eta)_{\Omega_f^0} + (\hat{\nabla} \hat{u}, \hat{\nabla} \hat{\psi}_f^\eta)_{\Omega_f^0} &= 0 \quad \forall \hat{\psi}_f^\eta \in \hat{V}_f^\eta \\
 (\alpha_\eta \hat{\nabla} \hat{\eta}, \hat{\nabla} \hat{\psi}_s^\eta)_{\Omega_s^0} &= 0 \quad \forall \hat{\psi}_s^\eta \in \hat{V}_s^\eta \\
 (\widehat{div}(\hat{J} \hat{F}^{-1} \hat{v}), \hat{\psi}_f^p)_{\Omega_f^0} &= 0 \quad \forall \hat{\psi}_f^p \in \hat{L}_f^p \\
 (\hat{J}_s^e - 1, \hat{\psi}_s^p)_{\Omega_s^0} &= 0 \quad \forall \hat{\psi}_s^p \in \hat{L}_s^p \quad (3.41) \\
 (d\hat{\rho}_s \frac{\partial \hat{g}_s}{\partial t}, \hat{\psi}_s^g)_{\Omega_s^0} - (\hat{f}_s^g \hat{g}_s, \hat{\psi}_s^g)_{\Omega_s^0} &= 0 \quad \forall \hat{\psi}_s^g \in \hat{L}_s^g \\
 (\hat{J} \frac{\partial \hat{c}_f}{\partial t}, \hat{\psi}_f^c)_{\Omega_f^0} + (\hat{J} \hat{F}^{-1} (\hat{v} - \frac{\partial \hat{u}}{\partial t}) \cdot \hat{\nabla} \hat{c}_f, \hat{\psi}_f^c)_{\Omega_f^0} \\
 + (\hat{J} D_f \hat{F}^{-T} \hat{\nabla} \hat{c}_f, \hat{F}^{-T} \hat{\nabla} \hat{\psi}_f^c)_{\Omega_f^0} + \langle \hat{g}_f^c, \hat{\psi}_f^c \rangle_{\Gamma_1^0 \cup \Gamma_2^0} &= 0 \quad \forall \hat{\psi}_f^c \in \hat{V}_f^c \\
 (\frac{\partial}{\partial t} (\hat{J} \hat{c}_s), \hat{\psi}_s^c)_{\Omega_s^0} + (\hat{J} \hat{D}_s \hat{F}^{-T} \hat{\nabla} \hat{c}_s, \hat{F}^{-T} \hat{\nabla} \hat{\psi}_s^c)_{\Omega_s^0} \\
 + (\hat{J} \hat{f}_s^r, \hat{\psi}_s^c)_{\Omega_s^0} + \langle \hat{g}_s^c, \hat{\psi}_s^c \rangle_{\Gamma_1^0 \cup \Gamma_2^0} &= 0 \quad \forall \hat{\psi}_s^c \in \hat{V}_s^c \\
 (\frac{\partial}{\partial t} (\hat{J} \hat{c}_s^*), \hat{\psi}_s^{c*})_{\Omega_s^0} - (\hat{J} \hat{f}_s^r, \hat{\psi}_s^{c*})_{\Omega_s^0} &= 0 \quad \forall \hat{\psi}_s^{c*} \in \hat{L}_s^{c*}
 \end{aligned}$$

with the function space of $\hat{\eta}$ defined as

$$\hat{V}_f^\eta := H_0^1(\Omega_f^0)^d, \quad \hat{V}_s^\eta := H_0^1(\Omega_s^0)^d \quad (3.42)$$

Here we highlight the variational formulations of biharmonic extension in (3.41) to show its difference from (3.33). Numerical simulations will also be performed with this formulation in the next chapter, and the results show that the maintenance of fluid mesh quality is much better in biharmonic extension than in harmonic one.

3.3 Theoretical results

In this section, we investigate the priori *energy estimate* to get the first step for approaching the existence of the solution of our model, and state a review of theoretical results from literatures which is related to our model (2.97) and (2.104).

Energy estimate of the model

First we write equations (2.97) in Ω_f^t in another form as

$$\begin{aligned}
 \rho_f \frac{\partial v_f}{\partial t} + \rho_f v_f \cdot \nabla v_f - \operatorname{div} \sigma_f &= \rho_f f_f^b \\
 \operatorname{div} v_f &= 0 \\
 \frac{\partial c_f}{\partial t} + v_f \cdot \nabla c_f - D_f \Delta c_f &= 0
 \end{aligned} \tag{3.43}$$

with the stress tensor

$$\sigma_f = -p_f I + \rho_f \nu (\nabla v_f + \nabla v_f^T) \tag{3.44}$$

Equations (2.104) in Ω_s^0 are not changed and the related functions are written as

$$\begin{aligned}
 \hat{f}_s^g &= \gamma \hat{f}_s^r, \quad \hat{f}_s^r = \beta \hat{c}_s \\
 \hat{\sigma}_s &= \begin{cases} -\hat{p}_s I + \hat{\mu}_s (\hat{F}_s^e \hat{F}_s^{eT} - I) & \text{(INH)} \\ -\hat{p}_s I + 2\hat{C}_1 \hat{F}_s^e \hat{F}_s^{eT} - 2\hat{C}_2 \hat{F}_s^{e-T} \hat{F}_s^{e-1} & \text{(IMR)} \end{cases} \\
 \hat{F}_s^e &= \hat{F}_s \hat{G}_s^{-1} = \frac{1}{\hat{g}_s} \hat{F}_s
 \end{aligned} \tag{3.45}$$

The energy estimate of equations (2.104) and (3.43) can be derived by following the energy estimate of general fluid-structure interaction problem coupled with convection-diffusion equations^[18;32;38;48;78]. Here we set that all the coefficients in (3.45) are constant for simplicity. Since the deformation gradient $\hat{J}_s = \hat{J}_s^e \hat{J}_s^g = \hat{J}_s^g$ is equal to \hat{g}_s^d , the equation for the metric of growth (2.48) can be written as

$$\frac{\partial \hat{J}_s}{\partial t} = \frac{\hat{f}_s^g}{\hat{\rho}_s} \hat{J}_s$$

which will not be in the energy inequality but will be used in its derivation. To prove this argument we start with equations (2.104). Multiplying the conservation equations of momentum with \hat{v}_s and integrating over Ω_s^0 , we obtain the formulations as

$$(\hat{J}_s \hat{\rho}_s \frac{\partial \hat{v}_s}{\partial t}, \hat{v}_s)_{\Omega_s^0} - (\widehat{\operatorname{div}}(\hat{J}_s \hat{\sigma}_s \hat{F}_s^{-T}), \hat{v}_s)_{\Omega_s^0} = (\hat{J}_s \hat{\rho}_s \hat{f}_s^b, \hat{v}_s)_{\Omega_s^0} \tag{3.46}$$

The first term can be written as

$$\begin{aligned}
 (\hat{J}_s \hat{\rho}_s \frac{\partial \hat{v}_s}{\partial t}, \hat{v}_s)_{\Omega_s^0} &= \frac{\hat{\rho}_s}{2} \int_{\Omega_s^0} \hat{J}_s \frac{\partial}{\partial t} |\hat{v}_s|^2 dX = \frac{\hat{\rho}_s}{2} \frac{\partial}{\partial t} \int_{\Omega_s^0} \hat{J}_s |\hat{v}_s|^2 dX \\
 -\frac{1}{2} \int_{\Omega_s^0} \hat{J}_s \hat{f}_s^g |\hat{v}_s|^2 dX &= \frac{\rho_s}{2} \frac{\partial}{\partial t} \int_{\Omega_s^t} |v_s|^2 dx - \frac{1}{2} \int_{\Omega_s^t} f_s^g |v_s|^2 dx \\
 &= \frac{\rho_s}{2} \frac{\partial}{\partial t} \|v_s\|_{\Omega_s^t}^2 - \frac{1}{2} \int_{\Omega_s^t} f_s^g |v_s|^2 dx
 \end{aligned} \tag{3.47}$$

and using integration by parts, the second term is treated as

$$-(\widehat{div}(\hat{J}_s \hat{\sigma}_s \hat{F}_s^{-T}), \hat{v}_s)_{\Omega_s^0} = (\hat{J}_s \hat{\sigma}_s \hat{F}_s^{-T}, \hat{\nabla} \hat{v}_s)_{\Omega_s^0} - \langle \hat{J}_s \hat{\sigma}_s \hat{F}_s^{-T} \cdot N_s, \hat{v}_s \rangle_{\Gamma_1^0 \cup \Gamma_2^0} \tag{3.48}$$

where the boundary conditions of \hat{v}_s in (2.101) is used. To treat the Cauchy stress tensor term $(\hat{J}_s \hat{\sigma}_s \hat{F}_s^{-T}) : \hat{\nabla} \hat{v}_s$, we use the second Piola-Kirchhoff stress tensor $\hat{S}_s = \hat{F}_s^{e-1} \hat{\sigma}_s \hat{F}_s^{e-T}$ and the *Green-Lagrange tensor* E_s which is defined as

$$E_s = \frac{1}{2} (F_s^{eT} F_s^e - I)$$

In the hyperelastic material with the property of objectivity, the stored energy function Ψ can be expressed by E_s ^[9;25], and \hat{S}_s has the relation with \hat{E}_s as

$$\hat{S}_s = \frac{\partial \hat{\Psi}}{\partial \hat{E}_s}(\hat{E}_s)$$

Since

$$\hat{J}_s \hat{\sigma}_s \hat{F}_s^{-T} = \hat{g}_s^d \hat{\sigma}_s \hat{F}_s^{e-T} \frac{1}{\hat{g}_s} = \hat{g}_s^{d-1} \hat{\sigma}_s \hat{F}_s^{e-T} = \hat{g}_s^{d-1} \hat{F}_s^e \hat{S}_s$$

By applying some theories of tensor analysis^[9;25], we have

$$\begin{aligned}
 (\hat{J}_s \hat{\sigma}_s \hat{F}_s^{-T}) : \hat{\nabla} \hat{v}_s &= \hat{g}_s^{d-1}(\hat{F}_s^e \hat{S}_s) : \hat{\nabla} \frac{\partial \hat{u}_s}{\partial t} = \hat{g}_s^{d-1}(\hat{F}_s^e \hat{S}_s) : \frac{\partial}{\partial t}(\hat{\nabla} \hat{u}_s) \\
 &= \hat{g}_s^{d-1}(\hat{F}_s^e \hat{S}_s) : \frac{\partial}{\partial t}(\hat{\nabla} \hat{u}_s + I) = \hat{g}_s^{d-1}(\hat{F}_s^e \hat{S}_s) : \frac{\partial \hat{F}_s}{\partial t} \\
 &= \hat{g}_s^{d-1}(\hat{F}_s^e \hat{S}_s) : \frac{\partial}{\partial t}(\hat{g}_s \hat{F}_s^e) = \hat{g}_s^d(\hat{F}_s^e \hat{S}_s) : \frac{\partial \hat{F}_s^e}{\partial t} + \hat{g}_s^{d-1}(\hat{F}_s^e \hat{S}_s) : \left(\frac{\partial \hat{g}_s}{\partial t} \hat{F}_s^e\right) \\
 &= \hat{g}_s^d \hat{S}_s : \hat{F}_s^{eT} \frac{\partial \hat{F}_s^e}{\partial t} + \hat{g}_s^{d-1} \frac{\partial \hat{g}_s}{\partial t} \text{tr}(\hat{F}_s^e \hat{S}_s \hat{F}_s^{eT}) = \hat{g}_s^d \hat{S}_s : \frac{\partial \hat{E}_s}{\partial t} + \frac{\hat{g}_s^d \hat{f}_s^g}{d \hat{\rho}_s} \text{tr}(\hat{\sigma}_s) \\
 &= \hat{g}_s^d \frac{\partial \hat{\Psi}}{\partial \hat{E}_s} : \frac{\partial \hat{E}_s}{\partial t} + \frac{\hat{g}_s^d \hat{f}_s^g}{d \hat{\rho}_s} \text{tr}(\hat{\sigma}_s) = \hat{J}_s \frac{\partial \hat{\Psi}}{\partial t}(\hat{E}_s) + \frac{\hat{J}_s \hat{f}_s^g}{d \hat{\rho}_s} \text{tr}(\hat{\sigma}_s)
 \end{aligned}$$

Combine the above relation with (3.48) and we get

$$\begin{aligned}
 -(\widehat{\text{div}}(\hat{J}_s \hat{\sigma}_s \hat{F}_s^{-T}), \hat{v}_s)_{\Omega_s^0} &= \int_{\Omega_s^0} \hat{J}_s \frac{\partial \hat{\Psi}}{\partial t}(\hat{E}_s) dX + \int_{\Omega_s^0} \frac{\hat{J}_s \hat{f}_s^g}{d \hat{\rho}_s} \text{tr}(\hat{\sigma}_s) dX \\
 -\langle \hat{J}_s \hat{\sigma}_s \hat{F}_s^{-T} \cdot N_s, \hat{v}_s \rangle_{\Gamma_1^0 \cup \Gamma_2^0} &= \frac{\partial}{\partial t} \int_{\Omega_s^0} \hat{J}_s \hat{\Psi}(\hat{E}_s) dX - \int_{\Omega_s^0} \frac{\hat{J}_s \hat{f}_s^g}{\hat{\rho}_s} \hat{\Psi}(\hat{E}_s) dX \\
 + \int_{\Omega_s^0} \frac{\hat{J}_s \hat{f}_s^g}{d \hat{\rho}_s} \text{tr}(\hat{\sigma}_s) dX - \langle \hat{J}_s \hat{\sigma}_s \hat{F}_s^{-T} \cdot N_s, \hat{v}_s \rangle_{\Gamma_1^0 \cup \Gamma_2^0} &= \frac{\partial}{\partial t} \int_{\Omega_s^t} \Psi(E_s) dx \\
 - \int_{\Omega_s^t} \frac{f_s^g}{\rho_s} \Psi(E_s) dx + \int_{\Omega_s^t} \frac{f_s^g}{d \rho_s} \text{tr}(\sigma_s) dx - \langle \sigma_s \cdot n_s, v_s \rangle_{\Gamma_1^t \cup \Gamma_2^t}
 \end{aligned}$$

and (3.46) is finally written as

$$\begin{aligned}
 \frac{\rho_s}{2} \frac{\partial}{\partial t} \|v_s\|_{\Omega_s^t}^2 + \frac{\partial}{\partial t} \int_{\Omega_s^0} \hat{\Psi}(\hat{E}_s) dX - \frac{1}{2} \int_{\Omega_s^t} f_s^g |v_s|^2 dx - \int_{\Omega_s^t} \frac{f_s^g}{\rho_s} \Psi(E_s) dx \\
 + \int_{\Omega_s^t} \frac{f_s^g}{d \rho_s} \text{tr}(\sigma_s) dx = \langle \sigma_s \cdot n_s, v_s \rangle_{\Gamma_1^t \cup \Gamma_2^t} + (\rho_s f_s^b, v_s)_{\Omega_s^t} \quad (3.49)
 \end{aligned}$$

Similarly by multiplying the equation for \hat{c}_s with \hat{c}_s and integrating over Ω_s^0 by parts, we have

$$\begin{aligned}
 \left(\frac{\partial}{\partial t}(\hat{J}_s \hat{c}_s), \hat{c}_s\right)_{\Omega_s^0} + (\hat{J}_s \hat{D}_s \hat{F}_s^{-T} \hat{\nabla} \hat{c}_s, \hat{F}_s^{-T} \hat{\nabla} \hat{c}_s)_{\Omega_s^0} + (\hat{J}_s \beta \hat{c}_s, \hat{c}_s)_{\Omega_s^0} \\
 = \langle \hat{J}_s \hat{D}_s \hat{F}_s^{-T} \hat{\nabla} \hat{c}_s \hat{F}_s^{-T} \cdot N_s, \hat{c}_s \rangle_{\Gamma_1^0 \cup \Gamma_2^0} \quad (3.50)
 \end{aligned}$$

The first term can also be written like (3.47) as

$$\begin{aligned}
 \left(\frac{\partial}{\partial t}(\hat{J}_s \hat{c}_s), \hat{c}_s\right)_{\Omega_s^0} &= \frac{1}{2} \frac{\partial}{\partial t} \int_{\Omega_s^0} \hat{J}_s \hat{c}_s^2 dX + \frac{1}{2} \frac{\partial}{\partial t} \int_{\Omega_s^0} \frac{\hat{J}_s \hat{f}_s^g}{\hat{\rho}_s} \hat{c}_s^2 dX \\
 &= \frac{1}{2} \frac{\partial}{\partial t} \|c_s\|_{\Omega_s^t}^2 + \frac{1}{2} \frac{\partial}{\partial t} \int_{\Omega_s^t} \frac{f_s^g}{\rho_s} c_s^2 dx
 \end{aligned} \tag{3.51}$$

For the definition of the diffusion coefficient D_s in (2.82), $D_{s,h} \leq \hat{D}_s \leq D_{s,d}$. Then by applying the formulas in Lemma 2.3.1 and Lemma 2.6.1, we obtain the second term and the boundary term as

$$\begin{aligned}
 (\hat{J}_s \hat{D}_s \hat{F}_s^{-T} \hat{\nabla} \hat{c}_s, \hat{F}_s^{-T} \hat{\nabla} \hat{c}_s)_{\Omega_s^0} &= (D_s \nabla c_s, \nabla c_s)_{\Omega_s^t} \geq D_{s,h} \|\nabla c_s\|_{\Omega_s^t}^2 \\
 \langle \hat{J}_s \hat{D}_s \hat{F}_s^{-T} \hat{\nabla} \hat{c}_s \hat{F}_s^{-T} \cdot N_s, \hat{c}_s \rangle_{\Gamma_1^0 \cup \Gamma_2^0} &= \langle D_s \nabla c_s \cdot n_s, c_s \rangle_{\Gamma_1^t \cup \Gamma_2^t}
 \end{aligned} \tag{3.52}$$

Summarizing the above formulas and due to transmission conditions (2.102) we can write (3.50) as

$$\begin{aligned}
 \frac{1}{2} \frac{\partial}{\partial t} \|c_s\|_{\Omega_s^t}^2 + \frac{1}{2} \int_{\Omega_s^t} \frac{f_s^g}{\rho_s} c_s^2 dx + D_{s,h} \|\nabla c_s\|_{\Omega_s^t}^2 \\
 + \beta \|c_s\|_{\Omega_s^t}^2 - \langle \zeta(c_f - c_s), c_s \rangle_{\Gamma_1^t \cup \Gamma_2^t} \leq 0
 \end{aligned} \tag{3.53}$$

By multiplying the equation for \hat{c}_s^* with \hat{c}_s^* and integrating over Ω_s^0 by parts, we can get the similar results as (3.53):

$$\frac{1}{2} \frac{\partial}{\partial t} \|c_s^*\|_{\Omega_s^t}^2 + \frac{1}{2} \int_{\Omega_s^t} \frac{f_s^g}{\rho_s} (c_s^*)^2 dx - \beta (c_s, c_s^*)_{\Omega_s^t} = 0 \tag{3.54}$$

We continue with equations (3.43) by multiplying the Navier-Stokes equations with v_f and the convection-diffusion equation with c_f . After integrating over Ω_f^t by parts, we have

$$\begin{aligned}
 \left(\rho_f \frac{\partial v_f}{\partial t}, v_f\right)_{\Omega_f^t} + (\rho_f v_f \cdot \nabla v_f, v_f)_{\Omega_f^t} + (\sigma_f, \nabla v_f)_{\Omega_f^t} \\
 = \langle \sigma_f \cdot n_f, v_f \rangle_{\Gamma_1^t \cup \Gamma_2^t \cup \Gamma_{f,in} \cup \Gamma_{f,out}} + (\rho_f f_f^b, v_f)_{\Omega_f^t}
 \end{aligned} \tag{3.55}$$

$$\begin{aligned}
 \left(\frac{\partial c_f}{\partial t}, c_f\right)_{\Omega_f^t} + (v_f \cdot \nabla c_f, c_f)_{\Omega_f^t} + (D_f \nabla c_f, \nabla c_f)_{\Omega_f^t} \\
 = \langle D_f \nabla c_f \cdot n_f, c_f \rangle_{\Gamma_1^t \cup \Gamma_2^t \cup \Gamma_{f,in}}
 \end{aligned} \tag{3.56}$$

3.3. THEORETICAL RESULTS

Here we get the boundary terms because of boundary conditions (2.100). With the help of Reynolds transport theorem (2.4), the time derivative terms of (3.55) and (3.56) are written as

$$(\rho_f \frac{\partial v_f}{\partial t}, v_f)_{\Omega_f^t} = \frac{\rho_f}{2} \frac{d}{dt} \|v_f\|_{\Omega_f^t}^2 - \frac{\rho_f}{2} \int_{\Gamma_1^t \cup \Gamma_2^t} |v_f|^2 v_f \cdot n_f da \quad (3.57)$$

$$(\frac{\partial c_f}{\partial t}, c_f)_{\Omega_f^t} = \frac{1}{2} \frac{d}{dt} \|c_f\|_{\Omega_f^t}^2 - \frac{1}{2} \int_{\Gamma_1^t \cup \Gamma_2^t} |c_f|^2 v_f \cdot n_f da \quad (3.58)$$

Regarding the convection terms, we use integration by parts and get

$$\begin{aligned} (\rho_f v_f \cdot \nabla v_f, v_f)_{\Omega_f^t} &= -\frac{\rho_f}{2} \int_{\Omega_f^t} |v_f|^2 \operatorname{div} v_f dx + \frac{\rho_f}{2} \int_{\Gamma_1^t \cup \Gamma_2^t \cup \Gamma_{f,in} \cup \Gamma_{f,out}} |v_f|^2 v_f \cdot n_f da \\ &= \frac{\rho_f}{2} \int_{\Gamma_1^t \cup \Gamma_2^t \cup \Gamma_{f,in} \cup \Gamma_{f,out}} |v_f|^2 v_f \cdot n_f da \end{aligned} \quad (3.59)$$

$$\begin{aligned} (v_f \cdot \nabla c_f, c_f)_{\Omega_f^t} &= -\frac{1}{2} \int_{\Omega_f^t} |c_f|^2 \operatorname{div} v_f dx + \frac{1}{2} \int_{\Gamma_1^t \cup \Gamma_2^t \cup \Gamma_{f,in} \cup \Gamma_{f,out}} |c_f|^2 v_f \cdot n_f da \\ &= \frac{1}{2} \int_{\Gamma_1^t \cup \Gamma_2^t \cup \Gamma_{f,in} \cup \Gamma_{f,out}} |c_f|^2 v_f \cdot n_f da \end{aligned} \quad (3.60)$$

The diffusion and boundary terms of c_f are easily obtained as

$$(D_f \nabla c_f, \nabla c_f)_{\Omega_f^t} = D_f \|\nabla c_f\|_{\Omega_f^t}^2 \quad (3.61)$$

$$\langle D_f \nabla c_f \cdot n_f, c_f \rangle_{\Gamma_1^t \cup \Gamma_2^t \cup \Gamma_{f,in}} = \langle D_f \nabla c_f \cdot n_f, c_f \rangle_{\Gamma_{f,in}} - \langle \zeta(c_f - c_s), c_f \rangle_{\Gamma_1^t \cup \Gamma_2^t}$$

Finally we treat the Cauchy stress tensor term with the help of the strain rate tensor $D(v_f)$ defined in Remark 2.4.1. For the symmetry of $D(v_f)$ we have

$$\begin{aligned} (\sigma_f, \nabla v_f)_{\Omega_f^t} &= (-p_f, \operatorname{div} v_f)_{\Omega_f^t} + 2\rho_f \nu (D(v_f), \nabla v_f)_{\Omega_f^t} \\ &= 2\rho_f \nu (D(v_f), D(v_f))_{\Omega_f^t} = 2\rho_f \nu \|D(v_f)\|_{\Omega_f^t}^2 \end{aligned} \quad (3.62)$$

So (3.55) and (3.56) can be written as

$$\begin{aligned}
 \frac{\rho_f}{2} \frac{d}{dt} \|v_f\|_{\Omega_f^t}^2 &+ 2\rho_f \nu \|D(v_f)\|_{\Omega_f^t}^2 + \frac{\rho_f}{2} \int_{\Gamma_{f,in} \cup \Gamma_{f,out}} |v_f|^2 v_f \cdot n_f da \\
 &= \langle \sigma_f \cdot n_f, v_f \rangle_{\Gamma_1^t \cup \Gamma_2^t \cup \Gamma_{f,in} \cup \Gamma_{f,out}} + (\rho_f f_f^b, v_f)_{\Omega_f^t} \quad (3.63)
 \end{aligned}$$

$$\begin{aligned}
 \frac{1}{2} \frac{d}{dt} \|c_f\|_{\Omega_f^t}^2 &+ D_f \|\nabla c_f\|_{\Omega_f^t}^2 + \frac{1}{2} \int_{\Gamma_{f,in} \cup \Gamma_{f,out}} |c_f|^2 v_f \cdot n_f da \\
 &= \langle D_f \nabla c_f \cdot n_f, c_f \rangle_{\Gamma_{f,in}} - \langle \zeta(c_f - c_s), c_f \rangle_{\Gamma_1^t \cup \Gamma_2^t} \quad (3.64)
 \end{aligned}$$

Now we define the energy of equations (2.104) and (3.43) as

$$\begin{aligned}
 \mathbb{E}(t) &= \frac{\rho_s}{2} \|v_s\|_{\Omega_s^t}^2 + \frac{1}{2} \|c_s\|_{\Omega_s^t}^2 + \frac{1}{2} \|c_s^*\|_{\Omega_s^t}^2 + \frac{\rho_f}{2} \|v_f\|_{\Omega_f^t}^2 + \frac{1}{2} \|c_f\|_{\Omega_f^t}^2 + \int_{\Omega_s^t} \Psi(E_s) dx \\
 &+ \int_0^t (D_{s,h} \|\nabla c_s(\tau)\|_{\Omega_s^t}^2 + 2\rho_f \nu \|D(v_f)(\tau)\|_{\Omega_f^t}^2 + D_f \|\nabla c_f(\tau)\|_{\Omega_f^t}^2) d\tau
 \end{aligned}$$

Summarizing (3.49), (3.53), (3.54), (3.63) and (3.64), we finally get

$$\begin{aligned}
 \frac{d}{dt} \mathbb{E}(t) &- \frac{1}{2} \int_{\Omega_s^t} f_s^g |v_s|^2 dx - \int_{\Omega_s^t} \frac{f_s^g}{\rho_s} \Psi(E_s) dx + \int_{\Omega_s^t} \frac{f_s^g}{d\rho_s} \text{tr}(\sigma_s) dx \\
 &+ \frac{1}{2} \int_{\Omega_s^t} \frac{f_s^g}{\rho_s} c_s^2 dx + \frac{1}{2} \int_{\Omega_s^t} \frac{f_s^g}{\rho_s} (c_s^*)^2 dx + \beta \|c_s\|_{\Omega_s^t}^2 + \zeta \|c_f - c_s\|_{\Gamma_1^t \cup \Gamma_2^t}^2 \\
 &+ \frac{\rho_f}{2} \int_{\Gamma_{f,in} \cup \Gamma_{f,out}} |v_f|^2 v_f \cdot n_f da + \frac{1}{2} \int_{\Gamma_{f,in} \cup \Gamma_{f,out}} |c_f|^2 v_f \cdot n_f da \quad (3.65) \\
 &\leq \langle \sigma_f \cdot n_f, v_f \rangle_{\Gamma_{f,in} \cup \Gamma_{f,out}} + \langle D_f \nabla c_f \cdot n_f, c_f \rangle_{\Gamma_{f,in}} \\
 &+ (\rho_s f_s^b, v_s)_{\Omega_s^t} + (\rho_f f_f^b, v_f)_{\Omega_f^t} + \beta (c_s, c_s^*)_{\Omega_s^t}
 \end{aligned}$$

The boundary terms of the stress tensors σ_s and σ_f on the interface vanish because of the transmission conditions as follows:

$$\langle \sigma_s \cdot n_s, v_s \rangle_{\Gamma_1^t \cup \Gamma_2^t} + \langle \sigma_f \cdot n_f, v_f \rangle_{\Gamma_1^t \cup \Gamma_2^t} = 0$$

If we assume that the reaction coefficient $\beta = 0$, both the growth function f_s^g and the reaction function f_s^r are equal to 0. Then in (3.65) some terms will vanish and we can simplify it as

$$\begin{aligned}
 \frac{d}{dt}\mathbb{E}(t) &+ \zeta \|c_f - c_s\|_{\Gamma_1^t \cup \Gamma_2^t}^2 + \frac{\rho_f}{2} \int_{\Gamma_{f,in} \cup \Gamma_{f,out}} |v_f|^2 v_f \cdot n_f da \\
 &+ \frac{1}{2} \int_{\Gamma_{f,in} \cup \Gamma_{f,out}} |c_f|^2 v_f \cdot n_f da \leq \langle \sigma_f \cdot n_f, v_f \rangle_{\Gamma_{f,in} \cup \Gamma_{f,out}} \quad (3.66) \\
 &+ \langle D_f \nabla c_f \cdot n_f, c_f \rangle_{\Gamma_{f,in}} + (\rho_s f_s^b, v_s)_{\Omega_s^t} + (\rho_f f_f^b, v_f)_{\Omega_f^t}
 \end{aligned}$$

If we assume that v_f and c_f have homogeneous Dirichlet boundary conditions, i.e. $v_f = c_f = 0$ on all outer boundaries, the boundary terms in (3.66) will be 0, and the energy estimate will hold in the following theorem:

Theorem 3.3.1 (Energy inequality and energy decay property). *Let equations (2.104) and (3.43) have homogeneous Dirichlet boundary conditions $v_f = c_f = 0$ on $\partial\Omega_f^t / (\Gamma_1^t \cup \Gamma_2^t)$, and assume the reaction coefficient $\beta = 0$. Then the following energy inequality holds:*

$$\begin{aligned}
 \mathbb{E}(t) &+ \int_0^t \zeta \|c_f(\tau) - c_s(\tau)\|_{\Gamma_1^\tau \cup \Gamma_2^\tau}^2 d\tau \\
 &\leq \left[\mathbb{E}(0) + \int_0^t \left(\frac{\rho_s}{2} \|f_s^b(\tau)\|_{\Omega_s^\tau}^2 + \frac{\rho_f}{2} \|f_f^b(\tau)\|_{\Omega_f^\tau}^2 \right) d\tau \right] e^t \quad (3.67)
 \end{aligned}$$

Further, if $f_s^b = 0$ in Ω_s^t and $f_f^b = 0$ in Ω_f^t , the following energy decay property is obtained:

$$\mathbb{E}(t) \leq \mathbb{E}(0) - \int_0^t \zeta \|c_f(\tau) - c_s(\tau)\|_{\Gamma_1^\tau \cup \Gamma_2^\tau}^2 d\tau \quad (3.68)$$

Proof. For homogeneous Dirichlet boundary conditions, all the boundary terms in (3.66) vanish, and by using Young's inequality we have

$$\begin{aligned}
 \frac{d}{dt}\mathbb{E}(t) &+ \zeta \|c_f - c_s\|_{\Gamma_1^t \cup \Gamma_2^t}^2 \leq (\hat{\rho}_s \hat{f}_s^b, \hat{v}_s)_{\Omega_s^0} + (\rho_f f_f^b, v_f)_{\Omega_f^t} \\
 &\leq \frac{\rho_s}{2} \|f_s^b\|_{\Omega_s^t}^2 + \frac{\rho_f}{2} \|f_f^b\|_{\Omega_f^t}^2 + \mathbb{E}(t) \quad (3.69)
 \end{aligned}$$

By integrating between 0 and t we get

$$\begin{aligned}
 \mathbb{E}(t) &+ \int_0^t \zeta \|c_f(\tau) - c_s(\tau)\|_{\Gamma_1^\tau \cup \Gamma_2^\tau}^2 d\tau \quad (3.70) \\
 &\leq \mathbb{E}(0) + \int_0^t \left(\frac{\rho_s}{2} \|f_s^b(\tau)\|_{\Omega_s^\tau}^2 + \frac{\rho_f}{2} \|f_f^b(\tau)\|_{\Omega_f^\tau}^2 \right) d\tau + \int_0^t \mathbb{E}(\tau) d\tau
 \end{aligned}$$

and by applying Gronwall inequality^[45] we obtain the energy inequality (3.67). If the body forces f_s^b and f_f^b are equal to 0, the right side of the formula (3.66) is zero, and the energy decay property (3.68) is easy to be derived.

□

Compared to the energy estimate of the simplified model (3.66), the energy estimate of our model (2.97) and (2.104) is not so easy to be derived as in Theorem 3.3.1. In this case the growth and reaction functions are not zero, so the whole system will be much more complicated and highly nonlinear. In the final formula (3.65) there are many noncontrollable terms with the growth function f_s^g . The positivity and limit of these terms are not identified, and the energy decay property does not exist without enough artificial conditions. So theoretically the existence of the solution of the system is still an open question.

Review of theoretical results

Our model (2.97) and (2.104) is complicated from the theoretical point of view. However, even if we split the whole system into different problems, some questions are still in general unanswered. One of the main sub-problems is the fluid-structure interaction (FSI) problem, which is ubiquitous in nature and has many examples in application^[16;44;45;53;78]. Mathematically the equations for fluid dynamics are described by the Navier-Stokes equations (or more generalized fluid models, e.g. the non-Newtonian fluid models) and the equations for structural mechanics are governed by the elastic structure equations. Both of these equations have theoretical results in different special conditions^[9;21;55;71], but the well-posedness is still not known in all configurations. The analysis of FSI problem is even at the beginning and have more open questions. This system couples parabolic (fluid) and hyperbolic (structure) equations, and different behavior of these equations induces a lack of regularity on the interface between the fluid and the structure, which is also mentioned in Section 3.2.3. The existence and uniqueness of such problem is proved for a special kind of structural material^[10]. In addition, the free boundary problem is also a challenging aspect in the FSI problem, while the analysis of a free boundary problem for fluid dynamics and species motion is obtained^[77]. Another important problem in our model is the convection-diffusion equation. In a special case if the FSI problem is coupled with the convection-diffusion equation by the velocity only in one way, it is possible to prove the well-posedness of convection-diffusion equation under the well-posedness of FSI problem^[47;48;74;75]. However in our model the concentrations

3.3. THEORETICAL RESULTS

in convection-diffusion equations are also inserted to the FSI problem by influencing the constitutive equations, so their mathematical investigation is still missing. Finally the growth modeling is also very interesting. The metric of growth is related to structural mechanics through constitutive equations, and represents a typical biological situation^[11]. For the complexity of the problem this model including metric of growth and structural mechanics is also an open mathematical question. Coupling the above problems together we see that our model (2.97) and (2.104) is complicatedly coupled and highly nonlinear, and the mathematical analysis of this model will lead far beyond the scope of this thesis.

Chapter 4

Numerical Simulation

Based on the variational formulation derived in Chapter 3, numerical simulations of our model can be performed. The numerical methods and software for our model are introduced in Section 3.1, and in Section 3.2 the numerical results are obtained in two different computational domains in two-dimensional space. To introduce the numerical methods we first consider the ALE variational formulation (3.33) or (3.41) in a semi-linear form as follows:

$$\hat{A}_T(\hat{U})\left(\frac{\partial \hat{U}}{\partial t}, \hat{\Phi}\right) + \hat{A}_R(\hat{U})(\hat{\Phi}) = \hat{F}(\hat{\Phi}) \quad \forall \hat{\Phi} \in \hat{X} \quad (4.1)$$

In this abstract form, $\hat{U} \in \hat{V}$ is the vector of variables and $\hat{\Phi}$ is the vector of test functions. \hat{V} and \hat{X} are the corresponding function spaces. $\hat{A}_T(\hat{U})\left(\frac{\partial \hat{U}}{\partial t}, \hat{\Phi}\right)$ are the terms with time derivative and $\hat{F}(\hat{\Phi})$ are terms with only known function in the model. $\hat{A}_R(\hat{U})(\hat{\Phi})$ are the remaining terms. Temporal discretization of form (4.1) is achieved with finite difference schemes, and spatial discretization is based on the Galerkin finite element method. Moreover we briefly describe the stabilization techniques to treat Stokes equations and convection-dominant problems. For solving nonlinear problems we use the Newton method to present its linearization. Numerical simulations are performed by using the software Gascoigne. We try different time step sizes and mesh refinement levels to investigate the convergence of solutions. Comparing the results also reveals the necessity of local mesh refinement to get more stable and accurate solutions. The numerical results are obtained first in a simple example for test and then in a core example in which the configuration is closer to a real artery. The results in both of these two domains support the assumption that the penetration of monocytes and the accumulation of foam cells lead to the formation and growth of plaques, and

that the evolution of plaques induces the increase of stresses in the vessel wall.

4.1 Numerical methods

4.1.1 Temporal discretization

To treat the abstract problem (4.1) we use *Rothe's method*, in which by temporal discretization with a single-step method, the problem is resolved into a sequence of generalized steady-state problems which can be discretized in space^[53;55;78]. To achieve temporal discretization with finite difference schemes, we first denote by

$$0 = t_0 < t_1 < t_2 < \dots < t_N = T, \quad k := t_n - t_{n-1}$$

a partition of the time interval $I = [0, T]$ into subintervals $I_n := (t_{n-1}, t_n]$ and by

$$\hat{U}^n := \hat{U}(t_n)$$

the solution at time t_n . For approximation of time derivative we use the *one-step- θ scheme* with a parameter $\theta \in [0, 1]$:

$$\begin{aligned} \hat{A}_T(\theta \hat{U}^n + (1 - \theta) \hat{U}^{n-1}) \left(\frac{\hat{U}^n - \hat{U}^{n-1}}{k}, \hat{\Phi} \right) + \theta \hat{A}_R(\hat{U}^n)(\hat{\Phi}) + (1 - \theta) \hat{A}_R(\hat{U}^{n-1})(\hat{\Phi}) \\ = \theta \hat{F}^n(\hat{\Phi}) + (1 - \theta) \hat{F}^{n-1}(\hat{\Phi}) \quad \forall \hat{\Phi} \in \hat{X} \end{aligned} \quad (4.2)$$

where $\hat{F}^n(\hat{\Phi}) := \hat{F}(\hat{\Phi})(t_n)$. This scheme includes some basic time-stepping schemes^[53;55;78]. They are the *implicit backward Euler scheme* for $\theta = 1$, the *explicit forward Euler scheme* for $\theta = 0$ and the *Crank-Nicolson scheme* for $\theta = \frac{1}{2}$. Both the implicit and the explicit Euler schemes show first order accuracy in the time step k , and the Crank-Nicolson scheme is of second order. For numerical simulations of our model we use the implicit backward Euler scheme to achieve temporal discretization, which is written as

$$\hat{A}_T(\hat{U}^n) \left(\frac{\hat{U}^n - \hat{U}^{n-1}}{k}, \hat{\Phi} \right) + \hat{A}_R(\hat{U}^n)(\hat{\Phi}) = \hat{F}^n(\hat{\Phi}) \quad \forall \hat{\Phi} \in \hat{X} \quad (4.3)$$

This classical scheme with stationary limit is strongly A-stable and dissipative. In contrast, the Crank-Nicolson scheme has higher order accuracy and

very little dissipation, but is not strongly A-stable^[78]. Actually in our model, the error from temporal discretization is much smaller than it from spacial one because of the high nonlinearity of the generalized steady-state problem (4.2), so high order accuracy of time-stepping scheme is not so necessary and the implicit backward Euler one is sufficient. We can also get from the numerical results in Section 4.2 that the convergence of the Crank-Nicolson scheme is weaker because of more Newton iterations in the same time step compared to the implicit backward Euler scheme.

4.1.2 Spatial discretization

The temporal-discretized problem (4.3) by the implicit backward Euler scheme is the starting point for spatial discretization. In time step $t_{n-1} \rightarrow t_n$, \hat{U}^{n-1} is already solved in the last time step. So we denote by

$$\hat{A}(\hat{U}^n)(\hat{\Phi}) := \hat{A}_T(\hat{U}^n)\left(\frac{\hat{U}^n - \hat{U}^{n-1}}{k}, \hat{\Phi}\right) + \hat{A}_R(\hat{U}^n)(\hat{\Phi})$$

the abstract form of problem (4.3) in each single time step, and in the following we will use the *Galerkin finite element method* to find a discrete solution \hat{U}^n of the problem

$$\hat{A}(\hat{U}^n)(\hat{\Phi}) = \hat{F}^n(\hat{\Phi}) \quad \forall \hat{\Phi} \in \hat{X} \quad (4.4)$$

The main idea of finite element method is to construct finite dimensional subspaces $\hat{V}_h \subset \hat{V}$ and $\hat{X}_h \subset \hat{X}$ of piecewise *polynomial functions* up to a limited order. For the definition of these discrete spaces we introduce *finite element mesh*. The computational domain $\Omega^0 := \Omega_f^0 \cup \Omega_s^0$ is partitioned into open elements \hat{K} . These elements are quadrilaterals in two and hexahedrons in three dimensions. The finite element mesh $\hat{\mathcal{T}}_h = \{\hat{K}\}$ of Ω^0 is formed by all elements. The element parameter \hat{h} is used to measure the error of numerical solutions, and is denoted by $\hat{h} = \max_{\hat{K} \in \hat{\mathcal{T}}_h} \hat{h}_{\hat{K}}$, where $\hat{h}_{\hat{K}} := \text{diam}(\hat{K})$ denotes the diameter of an element \hat{K} . We require the mesh to be regular, fulfilling the following conditions:

- 1) $\bar{\Omega}^0 = \bigcup_{\hat{K} \in \hat{\mathcal{T}}_h} \bar{\hat{K}}$.
- 2) $\hat{K}_1 \cap \hat{K}_2 = \emptyset, \forall \hat{K}_1, \hat{K}_2 \in \hat{\mathcal{T}}_h$ if $\hat{K}_1 \neq \hat{K}_2$.

3) Each edge (or face) of any element $\hat{K}_1 \in \hat{\mathcal{T}}_h$ is either a subset of $\partial\Omega^0$ or an edge (or face) of another element $\hat{K}_2 \in \hat{\mathcal{T}}_h$.

The last condition is too restrictive and sometimes it can be weakened. If a locally refined mesh is used, there will be several *hanging nodes* of elements which are allowed to lie on the edges (or faces) of neighboring elements^[78]. In this case the mesh is still considered to be regular.

To define the finite element spaces \hat{V}_h and \hat{X}_h we first define the space of polynomial functions up to a fixed order r in the reference element $\hat{K}_{unit} = (0, 1)^d$, and by using transformation from \hat{K}_{unit} to each element \hat{K} the space of polynomial functions in \hat{K} is defined^[53;78]. Then the finite element space \hat{X}_h is defined as a continuous function space in which each function $\hat{\Phi}_h$ is a polynomial function in every element, and has the same boundary conditions as the function $\hat{\Phi} \in \hat{X}$ has. From Problem 3.2.3 we can get that the differences between \hat{V}_h and \hat{X}_h are suitable extensions of the Dirichlet boundary data. Having these preparations of finite elements, we write the spatial-discretized problem of (4.4) as

$$\hat{A}(\hat{U}_h^n)(\hat{\Phi}_h) = \hat{F}^n(\hat{\Phi}_h) \quad \forall \hat{\Phi}_h \in \hat{X}_h \quad (4.5)$$

where $\hat{U}_h^n \in \hat{V}_h$ is its discrete solution. The exact form of (4.5) is derived from variational formulation (3.33) or (3.41), and specifically we discuss the finite element discretization of the Navier-Stokes equations and the convection-diffusion equations in our model. In the Navier-Stokes equations, a stable discretization needs to satisfy the *inf-sup condition*, but some finite elements (e.g. equal-order finite elements for both velocity and pressure) are not inf-sup stable. One well-known technique is to add a stabilization term to the divergence term of the Navier-Stokes equations, so that the finite elements satisfy a modified inf-sup condition, and can be proved to be stable from this condition^[51;53;55;56]. The stabilization term in each element $\hat{K} \in \hat{\mathcal{T}}_h$ is written as $\hat{h}_{\hat{K}}^2 (\hat{\nabla} \hat{p}_h, \hat{\nabla} \hat{\psi}_{f,h}^p)_{\Omega_f^0 \cap \hat{K}}$, where \hat{p}_h and $\hat{\psi}_{f,h}^p$ are polynomial functions with respect to the pressure \hat{p} and its test function $\hat{\psi}_f^p$. Additionally, in the equations for structural mechanics, if the material is incompressible, the function spaces need to fulfill an inf-sup condition and this "pressure-stabilization" term may be required for some finite elements as well^[53]. So in the spatial-discretized problem (4.5), the stabilization terms are added to the Navier-Stokes equations and the equations for structural mechanics as

$$\begin{aligned}
 (\widehat{div}(\hat{J}_h^n \hat{F}_h^{n,-1} \hat{v}_h^n), \hat{\psi}_{f,h}^p)_{\Omega_f^0} + \sum_{\hat{K} \in \hat{\mathcal{T}}_h} \hat{h}_{\hat{K}}^2 (\hat{\nabla} \hat{p}_h, \hat{\nabla} \hat{\psi}_{f,h}^p)_{\Omega_f^0 \cap \hat{K}} &= 0 \\
 (\hat{J}_{s,h}^{e,n} - 1, \hat{\psi}_{s,h}^p)_{\Omega_s^0} + \sum_{\hat{K} \in \hat{\mathcal{T}}_h} \hat{h}_{\hat{K}}^2 (\hat{\nabla} \hat{p}_h, \hat{\nabla} \hat{\psi}_{s,h}^p)_{\Omega_s^0 \cap \hat{K}} &= 0 \quad (4.6)
 \end{aligned}$$

The stabilization techniques should also be implemented in the convection-diffusion equation for the concentration \hat{c}_f , if the convection term gets dominant over the diffusion term. In our model the diffusion coefficient $D_f \ll 1$, so the numerical solution is not stable and has oscillations. One possible approach to stabilize this convection-dominant problem is to add an *artificial diffusion term* to the equation, and the modified form of this problem in (4.5) is written as

$$\begin{aligned}
 (\hat{J}_h^n \frac{1}{k} (\hat{c}_{f,h}^n - \hat{c}_{f,h}^{n-1}), \hat{\psi}_{f,h}^c)_{\Omega_f^0} + (\hat{J}_h^n \hat{F}_h^{n,-1} (\hat{v}_h^n - \frac{1}{k} (\hat{u}_h^n - \hat{u}_h^{n-1}))) \cdot \hat{\nabla} \hat{c}_{f,h}^n, \hat{\psi}_{f,h}^c)_{\Omega_f^0} \\
 + (\hat{J}_h^n D_f \hat{F}_h^{n,-T} \hat{\nabla} \hat{c}_{f,h}^n, \hat{F}_h^{n,-T} \hat{\nabla} \hat{\psi}_{f,h}^c)_{\Omega_f^0} \quad (4.7) \\
 + \langle \zeta (\hat{c}_{f,h}^n - \hat{c}_{s,h}^n) \hat{J}_h^n |\hat{F}_h^{n,-T} \cdot N_f|, \hat{\psi}_{f,h}^c \rangle_{\Gamma_1^0 \cup \Gamma_2^0} + \sum_{\hat{K} \in \hat{\mathcal{T}}_h} \delta_{\hat{K}} (\hat{\nabla} \hat{c}_{f,h}^n, \hat{\nabla} \hat{\psi}_{f,h}^c)_{\Omega_f^0 \cap \hat{K}} = 0
 \end{aligned}$$

Here $\delta_{\hat{K}} (\hat{\nabla} \hat{c}_{f,h}^n, \hat{\nabla} \hat{\psi}_{f,h}^c)_{\Omega_f^0 \cap \hat{K}}$ is the classical artificial diffusion term, and for the other stabilization techniques there are diffusion terms acting in the direction perpendicular to the streamlines^[8;33;55;78]. In particular, we expect that for $\hat{h} \rightarrow 0$ the additional stabilization term must vanish, and the most simple approach is to let the parameter $\delta_{\hat{K}}$ be dependent on $\hat{h}_{\hat{K}}$. Here we set $\delta_{\hat{K}}$ as

$$\delta_{\hat{K}} = \frac{1}{2} \left(\frac{D_f}{\hat{h}_{\hat{K}}^2} + \frac{\|\hat{v}_h^n\|_{\hat{K},max}}{\hat{h}_{\hat{K}}} \right)^{-1} \quad (4.8)$$

where $\|\hat{v}_h^n\|_{\hat{K},max} = \max_{\hat{K}} |\hat{v}_h^n|_{l^2} = \max_{\hat{K}} (\sum_{i=1}^d |\hat{v}_{h,i}^n|^2)^{\frac{1}{2}}$ is the norm of the local velocity vector^[54]. Furthermore in the convection-diffusion equation for the concentration \hat{c}_s , the convection term vanishes in the Lagrangian framework, and no additional stabilization term is necessary. So $\hat{h}_{\hat{K}}^2 (\hat{\nabla} \hat{p}_h, \hat{\nabla} \hat{\psi}_{f,h}^p)_{\Omega_f^0 \cap \hat{K}}$, $\hat{h}_{\hat{K}}^2 (\hat{\nabla} \hat{p}_h, \hat{\nabla} \hat{\psi}_{s,h}^p)_{\Omega_s^0 \cap \hat{K}}$ and $\delta_{\hat{K}} (\hat{\nabla} \hat{c}_{f,h}^n, \hat{\nabla} \hat{\psi}_{f,h}^c)_{\Omega_f^0 \cap \hat{K}}$ are the stabilization terms we should add to the formulation (4.5), and all of them are used for numerical simulations in Section 4.2.

4.1.3 Linearization

After temporal and spatial discretization, we get a stationary problem (4.5) in each single time step. The main difficulty to solve this problem is its high nonlinearity. To linearize the problem we use the *Newton method*, and in each iteration step $l = 0, 1, 2, \dots$, we solve the linear problem

$$\hat{A}'(\hat{U}_h^{n,l})(\hat{W}_h^{n,l+1}, \hat{\Phi}_h) = \hat{F}^n(\hat{\Phi}_h) - \hat{A}(\hat{U}_h^{n,l})(\hat{\Phi}_h) \quad \forall \hat{\Phi}_h \in \hat{X}_h \quad (4.9)$$

to get the solution $\hat{W}_h^{n,l+1} \in \hat{X}_h$, and update the solution of problem (4.5) by

$$\hat{U}_h^{n,l+1} = \hat{U}_h^{n,l} + \hat{W}_h^{n,l+1} \quad (4.10)$$

The residual defined as

$$R(\hat{U}_h^{n,l}) = \max_i \|\hat{F}^n(\hat{\Phi}_{h,i}) - \hat{A}(\hat{U}_h^{n,l})(\hat{\Phi}_{h,i})\| \quad (4.11)$$

is used to check whether a sufficiently accurate value of $\hat{U}_h^{n,l}$ is reached, and $\{\hat{\Phi}_{h,i}\}$ denotes the basis of the space \hat{X}_h . $\hat{A}'(\hat{U})(\hat{W}, \hat{\Phi})$ is the directional derivative of the mapping \hat{A} at \hat{U} in direction \hat{W} and is defined as

$$\hat{A}'(\hat{U})(\hat{W}, \hat{\Phi}) = \frac{d}{ds} \hat{A}(\hat{U} + s\hat{W})(\hat{\Phi})|_{s=0} \quad (4.12)$$

In problem (4.9), we can write $\hat{W}_h^{n,l+1}$ as a linear combination of the basis $\{\hat{\Phi}_{h,i}\}$:

$$\hat{W}_h^{n,l+1} = \sum_j w_j^{n,l+1} \hat{\Phi}_{h,j}$$

Then (4.9) is equivalent to the algebraic equations:

$$A^{n,l} w^{n,l+1} = b^{n,l} \quad (4.13)$$

with

$$A_{ij}^{n,l} = \hat{A}'(\hat{U}_h^{n,l})(\hat{\Phi}_{h,j}, \hat{\Phi}_{h,i}), \quad b_i^{n,l} = \hat{F}^n(\hat{\Phi}_{h,i}) - \hat{A}(\hat{U}_h^{n,l})(\hat{\Phi}_{h,i})$$

Specifically the matrix $A^{n,l}$ can be approximated as

$$A_{ij}^{n,l} \approx \frac{1}{\epsilon} (\hat{A}(\hat{U}_h^{n,l} + \epsilon \hat{\Phi}_{h,j})(\hat{\Phi}_{h,i}) - \hat{A}(\hat{U}_h^{n,l})(\hat{\Phi}_{h,i}))$$

4.1.4 Introduction of Gascoigne

In this section we briefly introduce the finite element library *Gascoigne*^[54], which is used to perform numerical simulations of our problem. In Gascoigne, the partial differential equations of our model are solved simultaneously by a monolithic approach, and given in the variational formulation as (4.5) in each time step:

$$\hat{A}(\hat{U}^n)(\hat{\Phi}) = \hat{F}^n(\hat{\Phi}) \quad \forall \hat{\Phi}$$

Gascoigne solves every problem with the Newton method, so the solutions are updated by solving linear problem in the variational formulation as (4.9) in each iteration step:

$$\hat{A}'(\hat{U}^{n,l})(\hat{W}^{n,l+1}, \hat{\Phi}) = \hat{F}^n(\hat{\Phi}) - \hat{A}(\hat{U}^{n,l})(\hat{\Phi}) \quad \forall \hat{\Phi}, \quad \hat{U}^{n,l+1} = \hat{U}^{n,l} + \hat{W}^{n,l+1}$$

where the initial guess $\hat{U}^{n,0}$ can be given by the solution in the last time step \hat{U}^{n-1} or the linear extension of the solutions \hat{U}^{n-1} and \hat{U}^{n-2} . The directional derivative of the mapping \hat{A} is defined as (4.12). So to solve the equations, Gascoigne needs to know about the right hand side $\hat{F}(\hat{\Phi})$, the form $\hat{A}(\hat{U})(\hat{\Phi})$ and its derivative $\hat{A}'(\hat{U})(\hat{W}, \hat{\Phi})$ ^[54]. $\hat{F}(\hat{\Phi})$ and $\hat{A}(\hat{U})(\hat{\Phi})$ can be easily derived from variational formulation (3.33) or (3.41), while the calculation of the matrix $\hat{A}'(\hat{U})(\cdot, \cdot)$ is cumbersome because of the strongly nonlinear behavior of the problem. Some literatures illustrate how to derive the directional derivative of the fluid-structure interaction problem^[55;78]. To overcome the difficulty of deriving its exact form we can also get an approximated form of $\hat{A}'(\hat{U})(\hat{W}, \hat{\Phi})$ and each component of the matrix is approximated as

$$\hat{A}'(\hat{U})_{ij}(\hat{W}, \hat{\Phi}) \approx \frac{1}{\epsilon} (\hat{A}(\hat{U} + \epsilon \hat{W}_j)_i(\hat{\Phi}) - \hat{A}(\hat{U})_i(\hat{\Phi}))$$

where \hat{W}_j and $\hat{A}(\hat{U})_i(\cdot)$ are the j -th and i -th components of \hat{W} and $\hat{A}(\hat{U})(\cdot)$. After inputting the information of the right hand side, the form and its derivative we derive above, with the initial and boundary data into the program, we can use Gascoigne to solve the problem. In each time step the information of the current mesh, solver, discretization and problem data is printed out in the output, which looks like Table 4.1.

In the first line of Table 4.1, the current time step (2), the number of mesh-refinement levels (5), the number of mesh nodes (1089) and the number of

```

...
===== 2 ===== [1,n,c] 5 1089 1024
  0: 9.77e-04
M  1: 7.73e-09 [0.00 0.00] - 6.26e-08 [0.012] {3}
[u.00002.vtk]
...

```

Table 4.1: Output of computational information in the 2-nd time step. From T. Richter^[54]

mesh elements (quads) (1024) are given. Below it the convergence history of the Newton method is printed on the left side. Here only one Newton iteration is used. Before this step, the residual of the equation is $9.77e - 04$, and after Newton iteration the residual is reduced to $7.73e - 09$. The letter M in the table indicates that in this step a new matrix $\hat{A}'(\hat{U})(\cdot, \cdot)$ is assembled with the solution in the last step as \hat{U} . The following two numbers [0.00 0.00] indicate the convergence rates of Newton iteration, where the first number is the reduction rate in the current step, and the second number is the average reduction rate over all steps. Since the convergence is very good after one iteration, and only the first 2 digits of the reduction rate are printed, in the table the numbers of the convergence rates are both 0. The computation in the second time step stops after one iteration, and if the computation is continued and the current convergence reduction rate is very small, Gascoigne will use the old matrix again instead of assembling a new matrix in the next iteration. On the right side, the convergence history of the linear multigrid solver is printed. In the numerical simulations of our model we do not use the multigrid solver, so all the numbers will be 0 on the right side. Finally the output file is printed out by Gascoigne with the name of *u.00002.vtk*, which can be visualized by the scientific visualization software *ParaView*.

4.2 Numerical results

In this section we present the results of numerical simulations of the model by using Gascoigne, and the numerical methods we've discussed before are used. Since the formation and evolution of plaques is a process with long time period, we need to choose a large time step k for temporal discretization. In such a long term the time differences of the quantities in the fluid domain, such as the velocity v_f and the concentration c_f , can be neglected because the motion of fluid has a different time scale from the motion of interface due to plaque growth. Therefore to reduce the complexity of computation, we remove the time differential terms in equations (2.97) to get a simplified model in the fluid domain:

$$\begin{aligned}
\rho_f v_f \cdot \nabla v_f - \rho_f \nu \Delta v_f + \nabla p_f &= \rho_f f_f^b \\
div v_f &= 0 \\
v_f \cdot \nabla c_f - D_f \Delta c_f &= 0
\end{aligned} \tag{4.14}$$

Numerical simulations are performed with the equations above and (2.104), and two examples are presented. Example I has a simple computational domain, being a test case to show good behavior of plaque formation, while in Example II the configuration is closer to a real artery. In both of these examples, the computational domains are in two-dimensional space, and all the parameters are obtained by considering the literatures about medicine, biodynamics and cardiovascular mathematics^[4;20;36;48;60;70;86]. We try different time step sizes and mesh refinement levels to investigate the convergence of numerical solutions as k and \hat{h} turn to zero, and use local mesh refinement and stabilization techniques to get more stable and accurate solutions. All pictures of the numerical results are made by the visualization softwares Gnuplot and Paraview.

4.2.1 Example I

In Example I we consider a simple computational domain in Figure 4.1. Like the general computational domain in Figure 2.1, it consists of two parts, the fluid part Ω_f^t and the solid part Ω_s^t , and has a length of $5.0mm$. Ω_f^t has a width of $2.0mm$ and Ω_s^t has a width of $1.0mm$. The upper dashed line denotes the interface $\Gamma_1^t \cup \Gamma_2^t$, and the red part denotes the interface Γ_1^t which is permeable for the monocytes, having a length of $0.5mm$. The lesion of the permeable interface can extend with the plaque growth, so we can assume that this length is not fixed and can be dependent on the displacement of the interface. Additionally, there is another blue dashed line in Ω_s^t , and we consider the layer between two dashed lines as endothelial cells and smooth muscle cells which are not effected a lot by plaque formation. In this layer, which has a width of $0.125mm$, chemical reactions rarely take place, so the monocytes will not be converted to foam cells. This fact is reasonable from physiological point of view, since when the monocytes are attracted, they will migrate through the endothelial cells into the vessel wall, but don't react in the endothelial-cell layer. When a plaque is formed, this layer can also be considered as the fibrous cap over the lipid core, in which there are few foam cells.

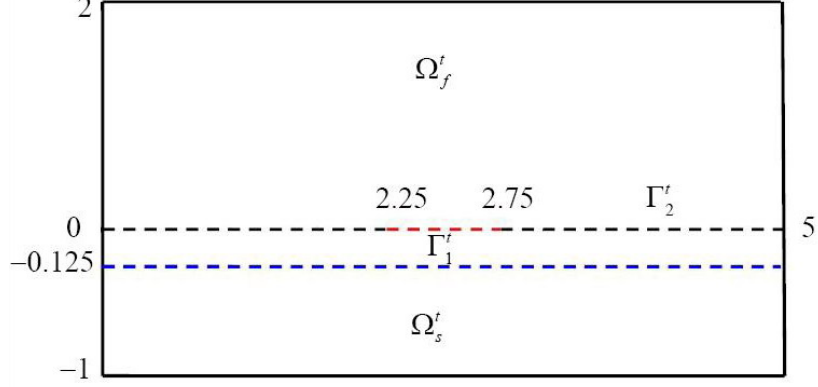


Figure 4.1: Configuration of the computational domain in Example I

In Ω_f^t , we set the density $\rho_f = 0.00106g/mm^3$, the kinematic viscosity $\nu = 3.0mm^2/s$, and the diffusion coefficient $D_f = 1.0 \times 10^{-7}mm^2/s$. The parameter setting is more complicated in Ω_s^t . First we set the density $\rho_s = 0.00106g/mm^3$ and the growth coefficient $\gamma = 1.0 \times 10^{-6}g$. As the shear modulus is defined as (2.79) in the constitutive equations of the incompressible neo-Hookean material, we set $\mu_{s,h} = 1.0 \times 10^5g/mm \cdot s^2$ in the healthy vessel wall and $\mu_{s,d} = 0.05 \times \mu_{s,h}$ in the diseased vessel wall. Similarly we set the coefficients $C_{i,h} = 1.0 \times 10^5g/mm \cdot s^2$ and $C_{i,d} = 0.05 \times C_{i,h}$ in the constitutive equations of the incompressible Mooney-Rivlin material, and the diffusion coefficient $D_{s,h} = 1.0 \times 10^{-7}mm^2/s$ and $D_{s,d} = 5.0 \times D_{s,h}$. The elastic coefficients decrease and the diffusion coefficient increases in the diseased vessel wall because as the plaque is formed, the diseased tissue becomes softer and easier for molecules to diffuse. Concerning the reaction coefficient, we set $\beta = 1.0 \times 10^{-6}/s$ under the lower dashed line and choose a much smaller amount between two dashed lines, so the reaction can be neglected in this upper layer of Ω_s^t . Finally on the interface, we set $\zeta = 1.0 \times 10^{-4}mm/s$ on Γ_1^t and $\zeta = 0$ on Γ_2^t . The corresponding initial and boundary conditions are given as (2.100) and (2.101). Especially the velocity profile of the blood flow is parabolic^[20], and we set the initial condition $v_f^0 = 100x(2-x)mm/s$. For the concentration of monocytes in Ω_f^t , we assume they are homogenized at the initial time, and the initial value $c_f^0 = 540.0/mm^3$.

Based on the configuration and parameter data we set before, numerical simulations of Example I are performed. Here we first consider INH material as the material of Ω_s^t . As is introduced in Section 4.1, the temporal discretization of the problem is achieved with finite difference schemes, and its spatial discretization is based on Galerkin finite element method. For finite

```

175
174000 -> 175000
  0: 3.89e-05
  1: 1.95e-07 [0.01 0.01] - 0.00e+00 [0.000] {0}
  2: 3.63e-08 [0.19 0.03] - 0.00e+00 [0.000] {0}
M 3: 1.16e-10 [0.00 0.01] - 0.00e+00 [0.000] {0}
  4: 6.41e-11 [0.55 0.04] 1 - 0.00e+00 [0.000] {0}
iteration 5.59

```

The implicit backward Euler scheme

```

175
174000 -> 175000
  0: 1.22e-01
  1: 3.98e-04 [0.00 0.00] - 0.00e+00 [0.000] {0}
  2: 7.76e-07 [0.00 0.00] - 0.00e+00 [0.000] {0}
  3: 3.57e-07 [0.46 0.01] - 0.00e+00 [0.000] {0}
M 4: 4.93e-09 [0.01 0.01] - 0.00e+00 [0.000] {0}
  5: 4.78e-09 [0.97 0.03] - 0.00e+00 [0.000] {0}
M 6: 3.99e-09 [0.84 0.06] 1 - 0.00e+00 [0.000] {0}
M 7: 3.57e-09 [0.90 0.08] - 0.00e+00 [0.000] {0}
M 8: 3.31e-09 [0.93 0.11] 1 - 0.00e+00 [0.000] {0}
M 9: 1.67e-09 [0.50 0.13] - 0.00e+00 [0.000] {0}
M 10: 1.44e-09 [0.87 0.16] 1 - 0.00e+00 [0.000] {0}
iteration 34.56

```

The Crank-Nicolson scheme

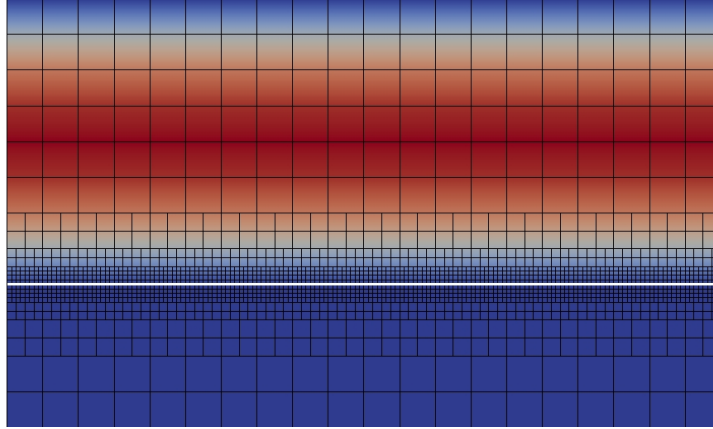
Table 4.2: Outputs of computational information by different temporal discretizations in the time step $[1.74 \times 10^5 s, 1.75 \times 10^5 s]$.

difference schemes we choose the time step size $k = 1000s$ and use both the implicit backward Euler scheme and the Crank-Nicolson scheme to compare the results. Table 4.2 shows the computational information by using both of them in the time step $[1.74 \times 10^5 s, 1.75 \times 10^5 s]$. In the implicit backward Euler scheme there is one iteration where a new matrix is assembled, and it takes 5.59 time units (here the unit is second) to finish computation in this time step. However in the Crank-Nicolson scheme there are ten Newton iterations and even six of them demand a new assembled matrix. It takes 34.56 seconds for computation in this time step, which is much longer than the former one. The table implies that the convergence of the Crank-Nicolson

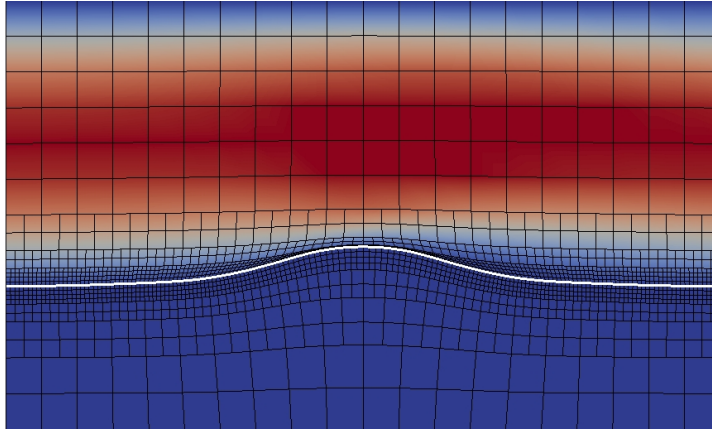
scheme is weaker in this problem, so we use the implicit backward Euler scheme for the following simulations.

Figure 4.2 shows the motion of the interface $\Gamma_1^t \cup \Gamma_2^t$ (indicated by the white line) and the distribution of velocity in x -direction in the whole domain $\Omega_f^t \cup \Omega_s^t$. The results are presented at different time points, and obtained on various meshes having 3 levels of local refinement near the interface. Additionally, the meshes are formed in the reference configuration as rectangles, so they will be deformed with the deformation of Ω_f^t and Ω_s^t . At initial time, the interface is parallel to the upper and lower boundary of the whole domain, and v_x defined in the whole domain is obtained by the initial value v_f in Ω_f^t and 0 in Ω_s^t . After 3.0×10^6 and 6.0×10^6 seconds, the interface has moved due to the formation and growth of the plaque in Ω_s^t and affected the value of v_x . This motion is also presented in Figure 4.3 with the distribution of displacement in y -direction in the solid domain Ω_s^t . We can see that after 6.0×10^6 seconds Ω_s^t has been deformed a lot to form a hump around the permeable interface Γ_1^t , where the displacement $u_{s,y}$ reaches the maximum value.

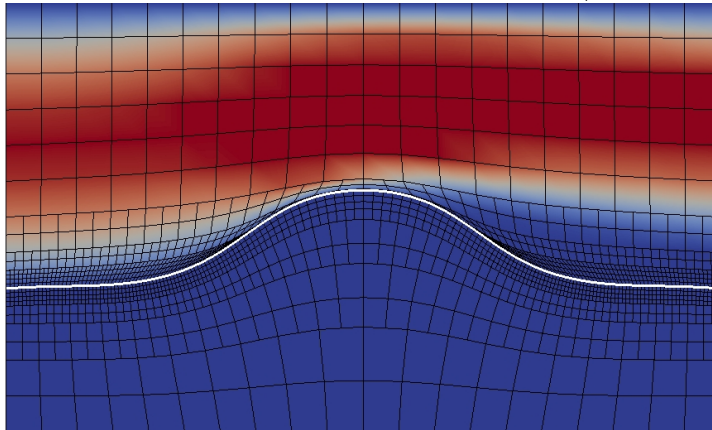
Figure 4.4 and Figure 4.5 show how plaque formation and growth are led to by the penetration of monocytes and the accumulation of foam cells. Figure 4.4 presents the distribution of concentration of monocytes in the fluid domain Ω_f^t . In the beginning the concentration c_f is homogenized as a constant initial value. When the plaque formation starts, the monocytes start to migrate through the permeable interface Γ_1^t into the solid domain Ω_s^t . Therefore their concentration will decrease after they move over Γ_1^t , which is significantly shown in Figure 4.4 at time $t = 6.0 \times 10^6 s$. As the monocytes differentiate into foam cells and accumulate in Ω_s^t , the concentration of foam cells c_s^* will increase from zero initial value. Figure 4.5 shows that the concentration of foam cells is very high at the place under a large deformation, which implies the fact that the accumulation of foam cells leads to the growth of plaques. Since the coefficient of permeability ζ is a constant, the penetration of monocytes is also at a constant speed, so the formed plaque has a symmetric structure. The region with high concentration of foam cells in Figure 4.5 is separated from the fluid domain Ω_f^t by a thin layer where the concentration of foam cells is low. That is because the reaction coefficient is very small in this layer and the monocytes can only be converted to foam cells after moving through the layer. So the region with high concentration of foam cells can be considered as the lipid core formed in the plaque, and the small layer can be considered as the fibrous cap, protecting the plaque from rupture.



$t = 0, \max v_x = 300\text{mm/s}$



$t = 3.0 \times 10^6\text{s}, \max v_x = 325.68\text{mm/s}$

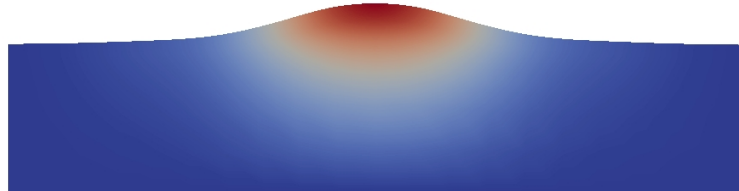


$t = 6.0 \times 10^6\text{s}, \max v_x = 419.28\text{mm/s}$

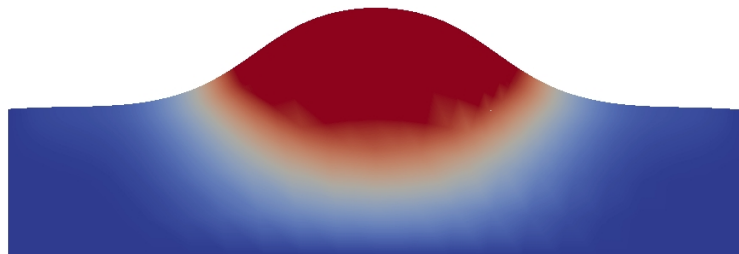
Figure 4.2: Motion of the interface and distribution of velocity in x -direction in the whole domain $\Omega_f^t \cup \Omega_s^t$. $k = 1000\text{s}$, mesh refinement level = 3. White line indicates the interface. Red color denotes high value, while blue color denotes low value.



$t = 0, \max u_{s,y} = 0mm$



$t = 3.0 \times 10^6 s, \max u_{s,y} = 0.28mm$



$t = 6.0 \times 10^6 s, \max u_{s,y} = 0.69mm$

Figure 4.3: Distribution of displacement in y -direction in the solid domain Ω_s^t . $k = 1000s$, mesh refinement level = 3. Red color denotes high value, while blue color denotes low value.

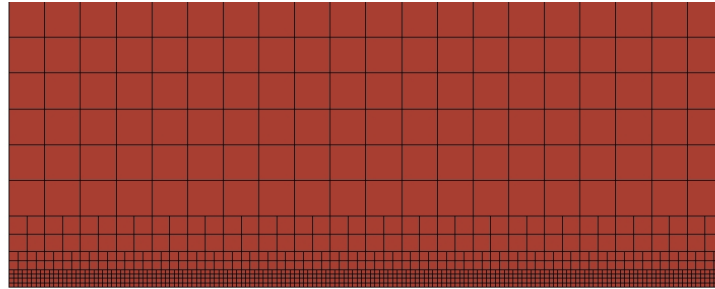
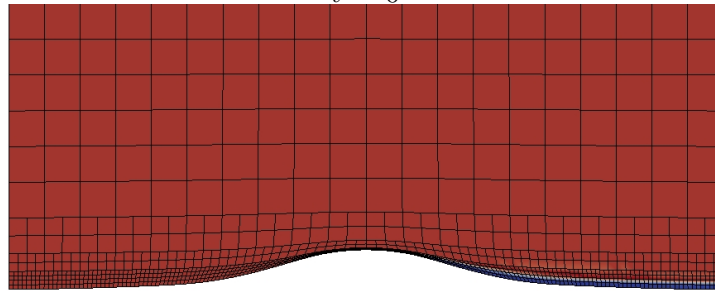
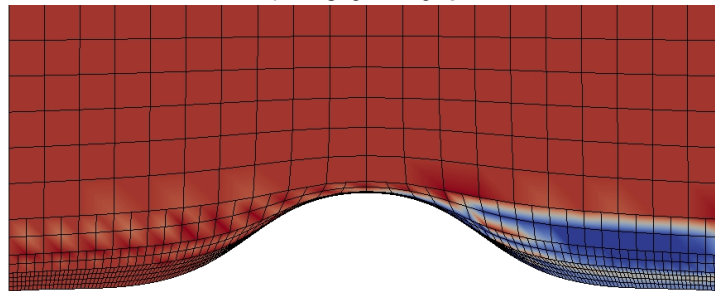
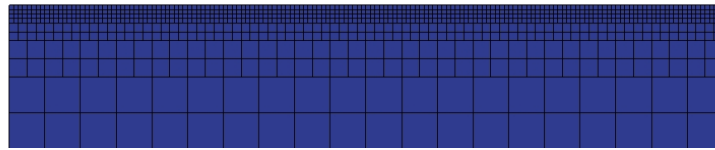
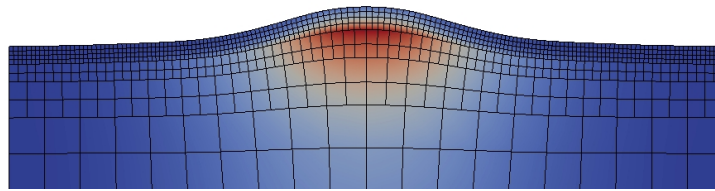
 $t = 0$  $t = 3.0 \times 10^6 s$  $t = 6.0 \times 10^6 s$

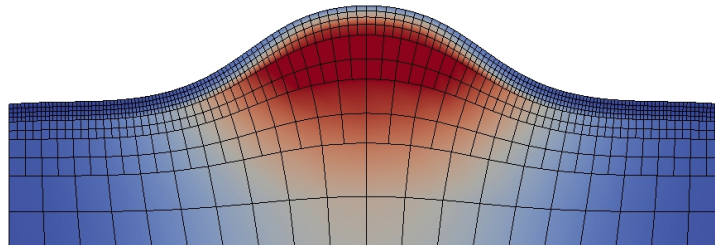
Figure 4.4: Distribution of concentration of monocytes in the fluid domain Ω_f^t . $k = 1000s$, mesh refinement level = 3. Red color denotes high value, while blue color denotes low value.



$$t = 0, \max c_s^* = 0/mm^3$$

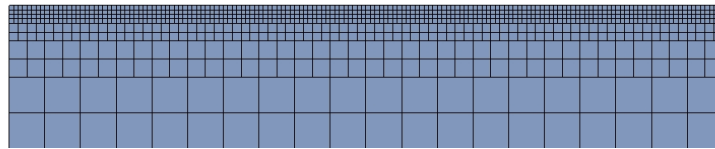


$$t = 3.0 \times 10^6 s, \max c_s^* = 788/mm^3$$

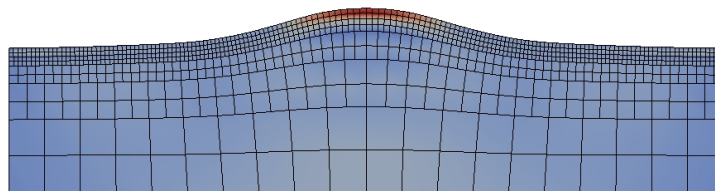


$$t = 6.0 \times 10^6 s, \max c_s^* = 1107/mm^3$$

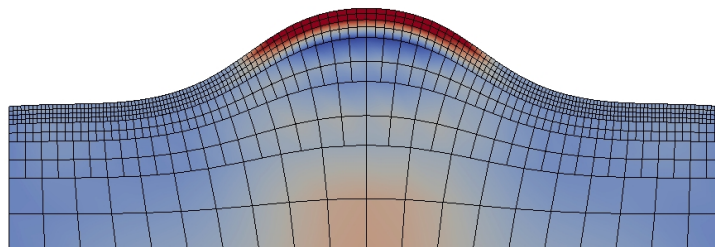
Figure 4.5: Distribution of concentration of foam cells in the solid domain Ω_s^t . $k = 1000s$, mesh refinement level = 3. Red color denotes high value, while blue color denotes low value.



$$t = 0, \max \sigma_{s,p} = 0g/mm \cdot s^2$$



$$t = 3.0 \times 10^6 s, \max \sigma_{s,p} = 2780.26g/mm \cdot s^2$$



$$t = 6.0 \times 10^6 s, \max \sigma_{s,p} = 9994.18g/mm \cdot s^2$$

Figure 4.6: Distribution of principal stress in the solid domain Ω_s^t . $k = 1000s$, mesh refinement level = 3. Red color denotes high value, while blue color denotes low value.

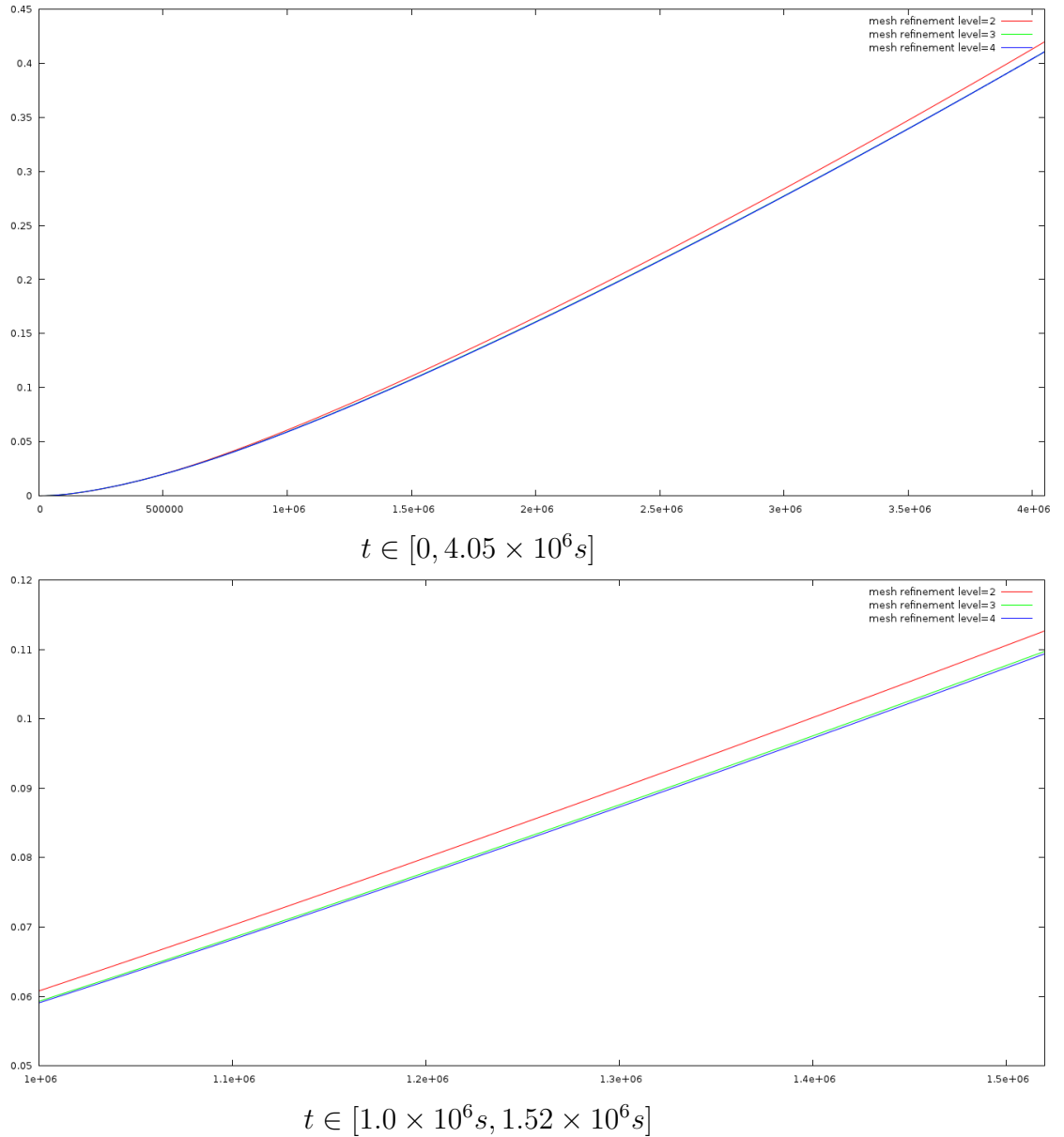


Figure 4.7: Evolution of displacement $u_{s,y}$ at the point $(2.5\text{mm}, 0)$ with different levels of mesh refinement, implying the convergence of numerical solutions as $\hat{h} \rightarrow 0$.

4.2. NUMERICAL RESULTS

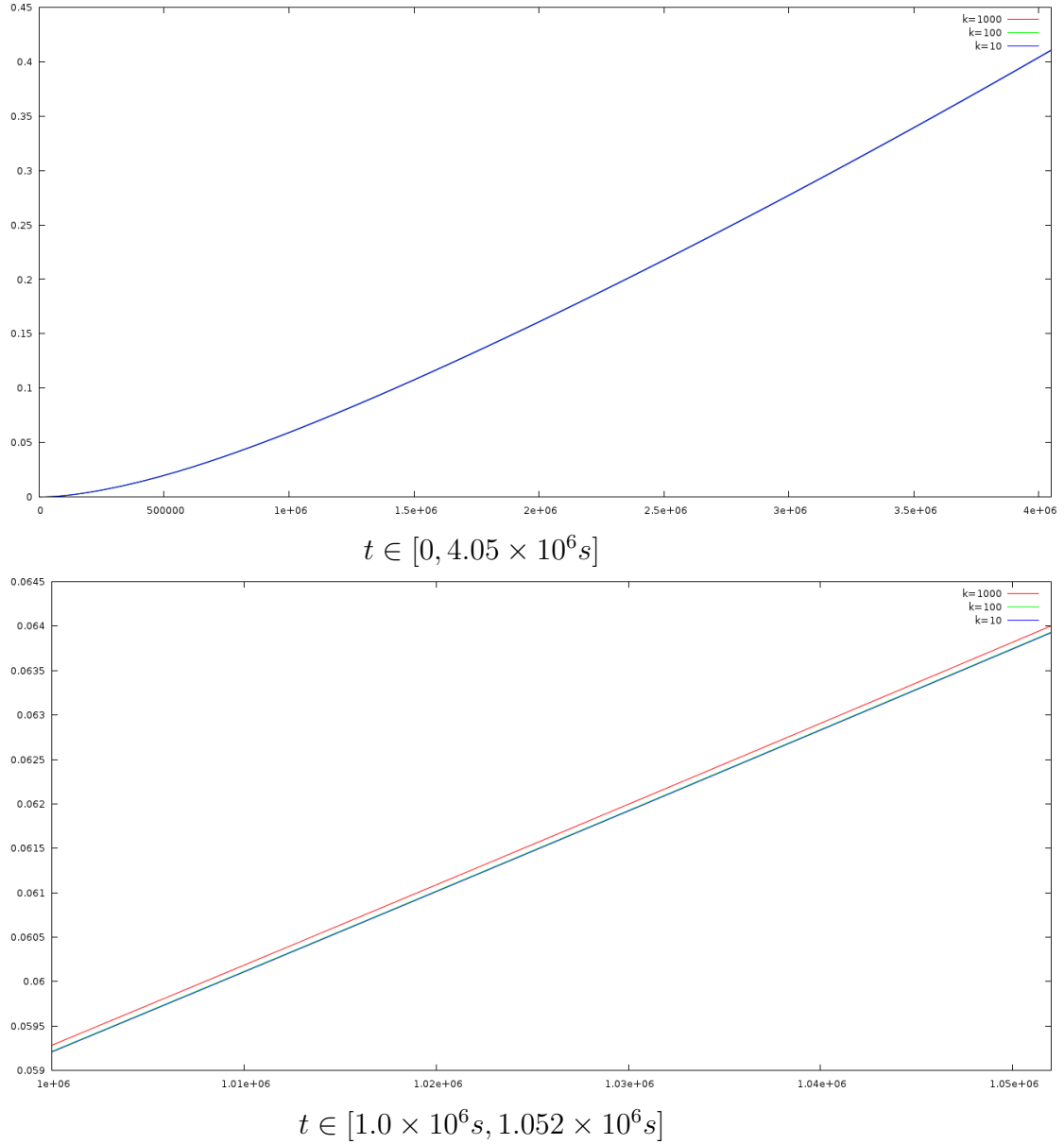
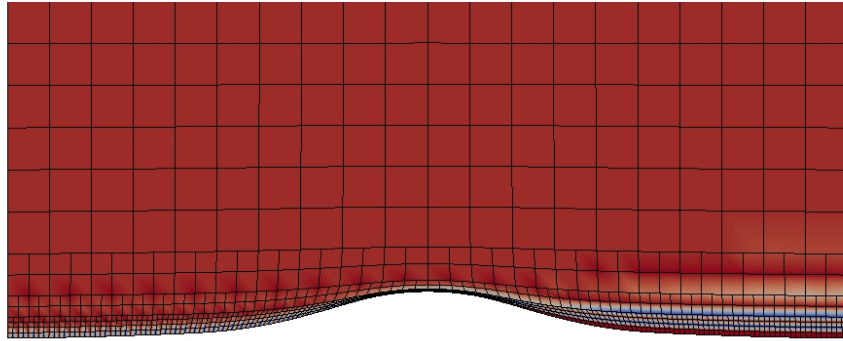
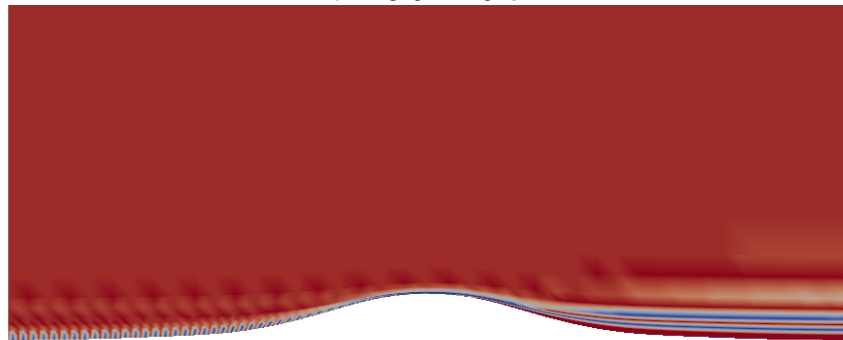


Figure 4.8: Evolution of displacement $u_{s,y}$ at the point $(2.5mm, 0)$ with different time step sizes, implying the convergence of numerical solutions as $k \rightarrow 0$.



$t = 3.0 \times 10^6 s$



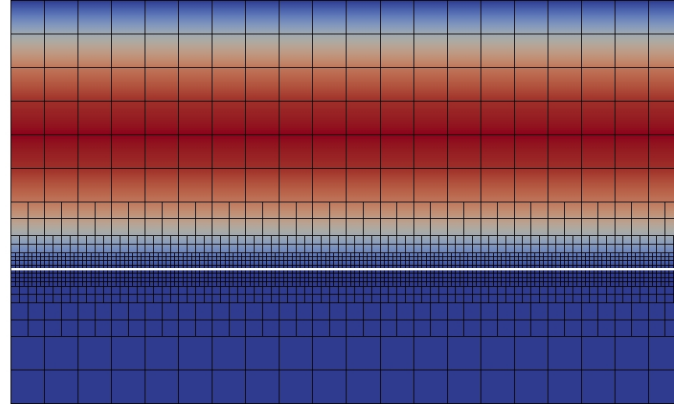
without grids

Figure 4.9: Distribution of concentration of monocytes c_f in the model without artificial diffusion term, implying necessity of this stabilization technique.

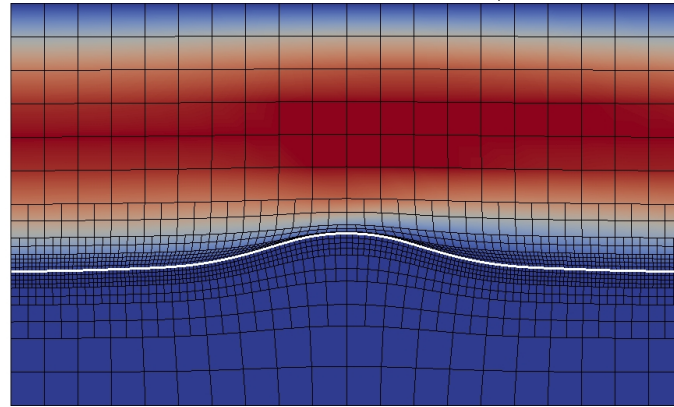
However this 'fibrous cap' will be easily disrupted by extrinsic stress applied on the plaque. As is shown in Figure 4.6, the principal stress $\sigma_{s,p}$, which is the eigenvalue of the stress tensor σ_s , is at a very high value around the hump of the interface, which is also a part of the 'fibrous cap'. In contrast, $\sigma_{s,p}$ is much smaller in the 'lipid core', even though this part is also under a large deformation. It is because the shear modulus μ_s is smaller in the region with high concentration of foam cells, and so is the stress value. The results in Figure 4.6 imply that as plaques are growing, the stresses in the vessel wall are increased, and the maximum value will be reached around the hump of the interface, where plaque rupture will possibly be induced.

In the numerical simulations of Example I, we also try different time step sizes and mesh refinement levels to compare the results. Figure 4.7 shows the comparison of solutions with different levels of mesh refinement. The x -axis indicates time and the y -axis denotes the displacement $u_{s,y}$ at the point $(2.5mm, 0)$. Comparing $u_{s,y}$ at this point with 2, 3, 4 levels of mesh refinement, especially in a local interval $[1.0 \times 10^6s, 1.52 \times 10^6s]$, we observe that the difference between solutions with adjacent levels of mesh refinement is decreasing as meshes are refined. The results imply that numerical solutions will converge if meshes keep being refined, which is also equivalent to that the error of numerical solutions will vanish if the element parameter $\hat{h} \rightarrow 0$. Similarly the comparison of solutions with different time step sizes is shown in Figure 4.8. The displacement $u_{s,y}$ at the point $(2.5mm, 0)$ is computed with time step sizes $k = 1000s, 100s, 10s$, and different solutions, especially solutions with $k = 100s, 10s$, almost coincide even if they are observed in a very local interval $[1.0 \times 10^6s, 1.052 \times 10^6s]$. It implies that numerical solutions will also converge if $k \rightarrow 0$.

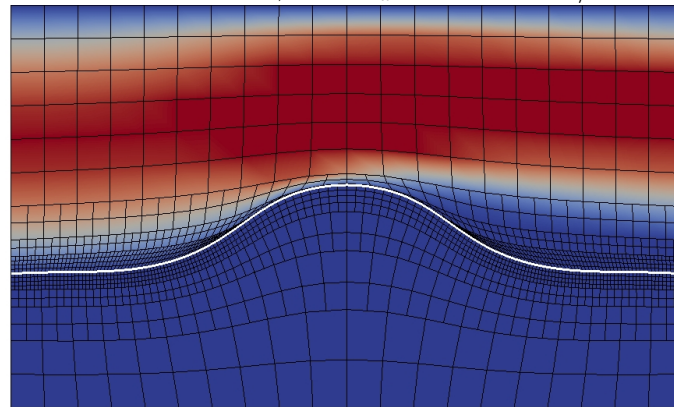
Figure 4.7 reveals the necessity of local mesh refinement near the interface, which obtains more stable and accurate solutions, and additionally, using stabilization techniques is also very necessary. Figure 4.9 shows the distribution of concentration of monocytes c_f in the fluid domain Ω_f^t if the artificial diffusion term in (4.7) is removed from the model. Without this additional stabilization term, the convection term in the convection-diffusion equation for c_f gets dominant over the diffusion term, so after 3.0×10^6 seconds we can see that even though the meshes are locally refined and maintained, the numerical solution of c_f is still very unstable and has large oscillations near the interface, which is more clearly observed if we remove grids in Ω_f^t . Solutions with such a large oscillation will not be accurate, and the crash of computation will possibly happen. So in the following numerical simulations we will always add the artificial diffusion term to keep solutions stable.



$t = 0, \max v_x = 300\text{mm/s}$



$t = 3.0 \times 10^6\text{s}, \max v_x = 326.51\text{mm/s}$

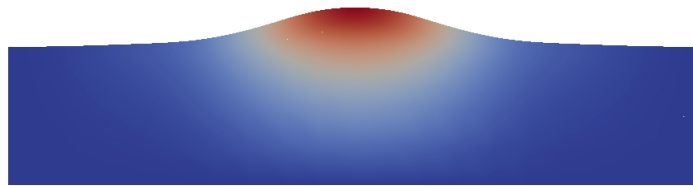


$t = 5.5 \times 10^6\text{s}, \max v_x = 404.59\text{mm/s}$

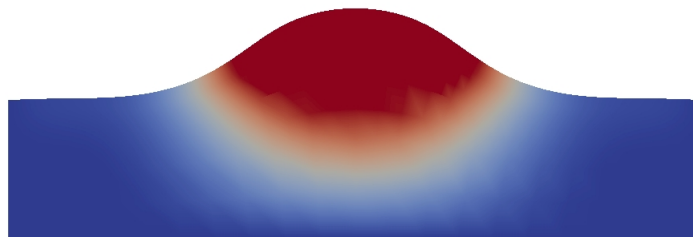
Figure 4.10: Motion of the interface and distribution of velocity in x -direction in the whole domain $\Omega_f^t \cup \Omega_s^t$ if the incompressible Mooney-Rivlin material is considered. $k = 1000\text{s}$, mesh refinement level = 3. White line indicates the interface. Red color denotes high value, while blue color denotes low value.



$t = 0, \max u_{s,y} = 0mm$



$t = 3.0 \times 10^6 s, \max u_{s,y} = 0.28mm$



$t = 5.5 \times 10^6 s, \max u_{s,y} = 0.66mm$

Figure 4.11: Distribution of displacement in y -direction in the solid domain Ω_s^t if the incompressible Mooney-Rivlin material is considered. $k = 1000s$, mesh refinement level = 3. Red color denotes high value, while blue color denotes low value.

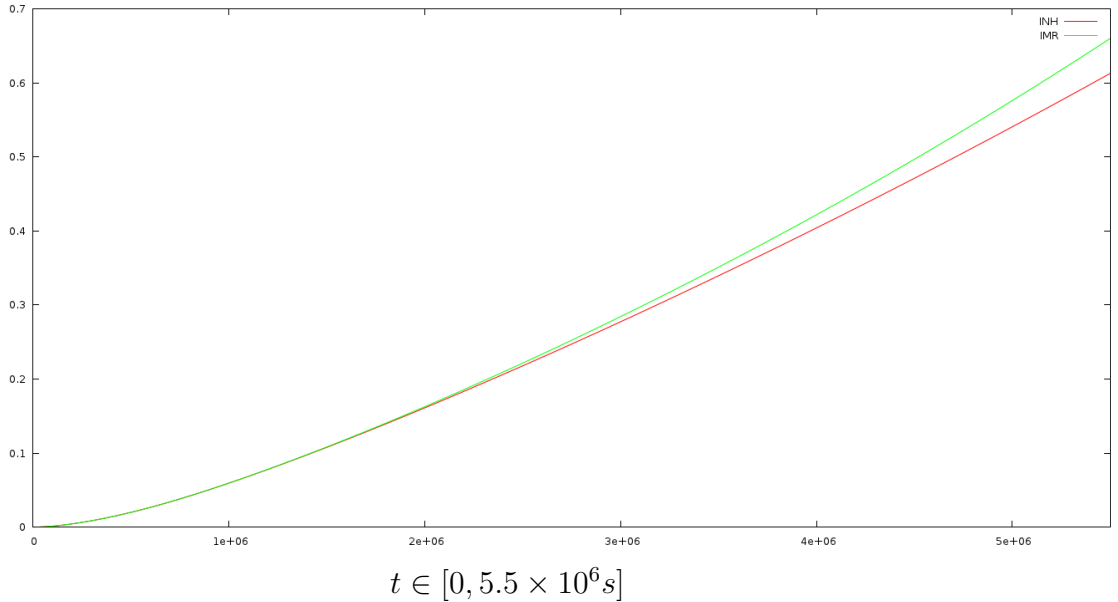


Figure 4.12: Comparison of displacements $u_{s,y}$ at the point $(2.5\text{mm}, 0)$ in the incompressible neo-Hookean material (INH) and the incompressible Mooney-Rivlin material (IMR).

Finally we consider the IMR material as the material of Ω_s^t and perform numerical simulations of Example I. Figure 4.10 shows the motion of the interface and the distribution of velocity in x -direction in the whole domain $\Omega_f^t \cup \Omega_s^t$, and in Figure 4.11 the distribution of displacement in y -direction in the solid domain Ω_s^t is observed. The results are quite similar to the ones in Figure 4.2 and Figure 4.3. Especially in Figure 4.12 the evolutions of displacements $u_{s,y}$ at the point $(2.5\text{mm}, 0)$ in the INH material and the IMR material are compared, and for this quantity the INH and the IMR models exhibit similar behavior. Since there is not any significant difference between these two models, we suggest to work with the INH model in this test case because it is the simplest material model. And the obtained results of the INH model from Figure 4.2 to Figure 4.6 show good behavior in how the penetration of monocytes and the accumulation of foam cells lead to the formation and growth of plaque, and the evolution of plaques induces the increase of stresses in the vessel wall, which may cause plaque rupture.

4.2.2 Example II

In Example II, we consider the computational domain in Figure 4.13, having a similar structure as the domain in Example I, but the configuration is more complicated, determined from literatures of medicine and biodynamics so that it is closer to a real artery such as the carotid^[4;20;60]. The whole domain $\Omega_f^t \cup \Omega_s^t$ has a length of $35.0mm$, while the fluid domain Ω_f^t has a width of $5.0mm$ and the solid domain Ω_s^t has a width of $0.5mm$. The permeable interface Γ_1^t has a length of $2.5mm$, and the layer between two dashed lines, representing the endothelial-cell layer or the fibrous cap, has a width of $0.0625mm$. The parameters in Example II are similar to the ones in Example I. For the fluid domain Ω_f^t , we set $\rho_f = 0.00106g/mm^3$, $\nu = 3.0mm^2/s$, and $D_f = 1.0 \times 10^{-7}mm^2/s$. The solid domain Ω_s^t is characterized by $\rho_s = 0.00106g/mm^3$, $\gamma = 1.0 \times 10^{-6}g$, $\mu_{s,h} = 1.0 \times 10^5g/mm \cdot s^2$, $\mu_{s,d} = 0.05 \times \mu_{s,h}$, $C_{i,h} = 1.0 \times 10^5g/mm \cdot s^2$, $C_{i,d} = 0.05 \times C_{i,h}$, $D_{s,h} = 1.0 \times 10^{-7}mm^2/s$ and $D_{s,d} = 5.0 \times D_{s,h}$. We set $\beta = 1.0 \times 10^{-7}/s$ under the lower dashed line and also choose a much smaller amount between two dashed lines. On the interface $\Gamma_1^t \cup \Gamma_2^t$, $\zeta = 1.0 \times 10^{-4}mm/s$ on Γ_1^t and is equal to zero on Γ_2^t .

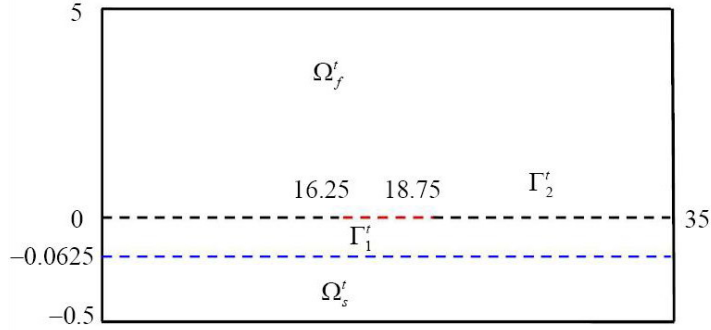
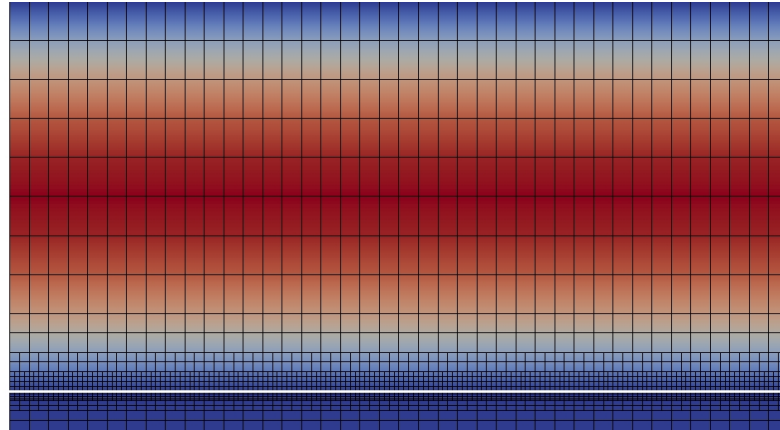
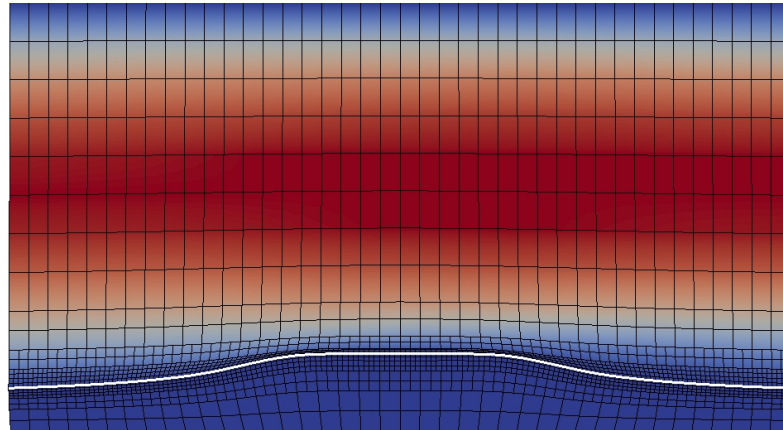


Figure 4.13: Configuration of the computational domain in Example II

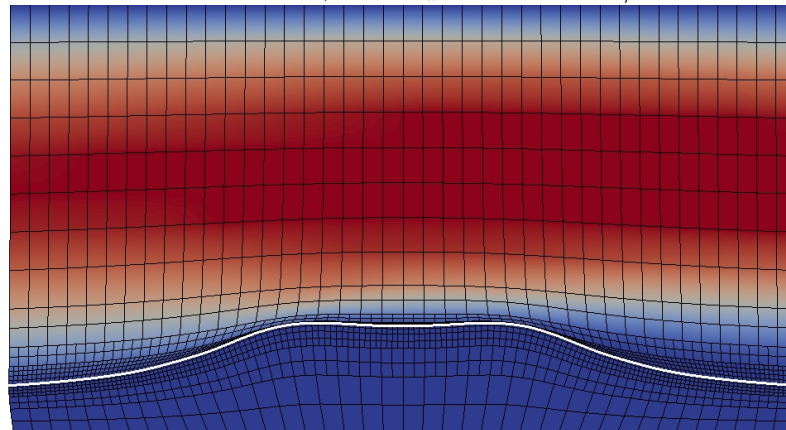
In the same way as Example I, numerical simulations of Example II are performed. We first choose time step size $k = 1000s$ and 2 levels of local refinement near the interface, and as the region with plaque formation is most interesting, all the numerical results are presented in the segmentation from $12.5mm$ to $22.5mm$ in the computational domain. Figure 4.14 and Figure 4.15 show the motion of the interface $\Gamma_1^t \cup \Gamma_2^t$, the distribution of velocity in x -direction in the whole domain $\Omega_f^t \cup \Omega_s^t$, and the distribution of displacement in y -direction in the solid domain Ω_s^t . From the results shown at time $t = 3.0 \times 10^7s$ and $t = 4.5 \times 10^7s$, it is observed that the interface



$$t = 0, \max v_x = 300\text{mm/s}$$



$$t = 3.0 \times 10^7\text{s}, \max v_x = 315.04\text{mm/s}$$



$$t = 4.5 \times 10^7\text{s}, \max v_x = 334.51\text{mm/s}$$

Figure 4.14: Motion of the interface and distribution of velocity in x -direction in the whole domain $\Omega_f^t \cup \Omega_s^t$. $k = 1000\text{s}$, mesh refinement level = 2. White line indicates the interface. Red color denotes high value, while blue color denotes low value.

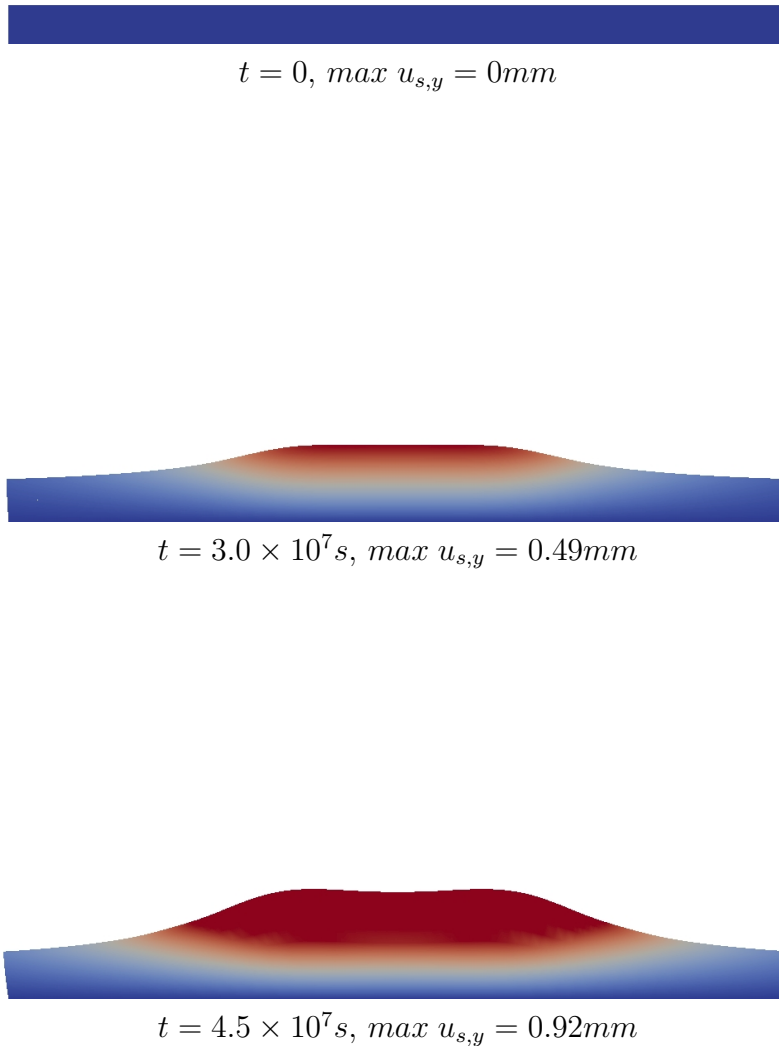


Figure 4.15: Distribution of displacement in y -direction in the solid domain Ω_s^t . $k = 1000s$, mesh refinement level = 2. Red color denotes high value, while blue color denotes low value.

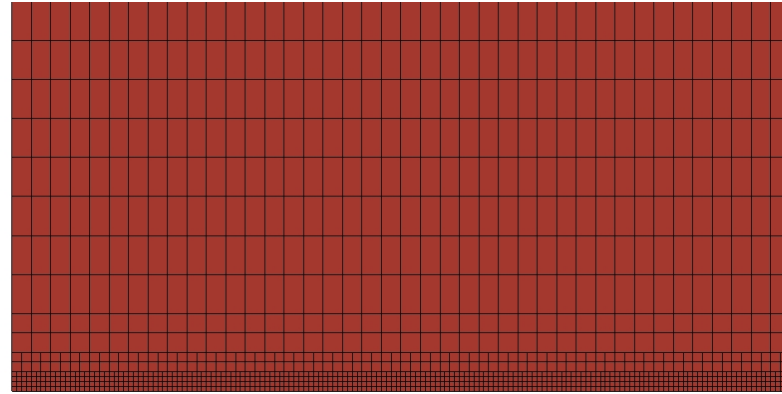
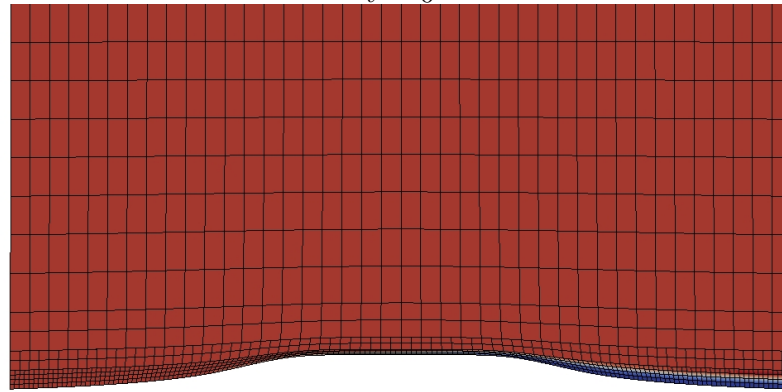
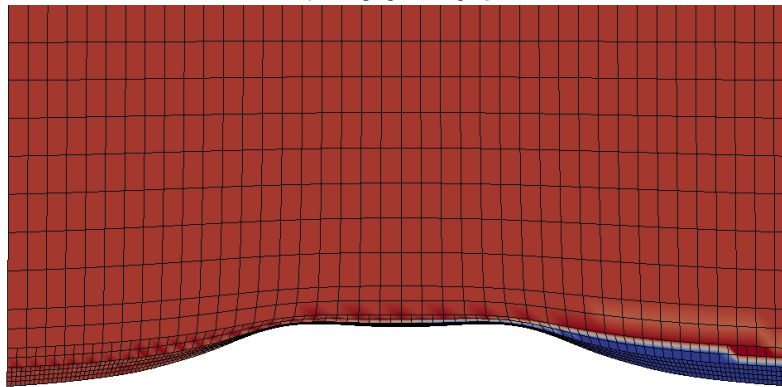
 $t = 0$  $t = 3.0 \times 10^7 s$  $t = 4.5 \times 10^7 s$

Figure 4.16: Distribution of concentration of monocytes in the fluid domain Ω_f^t . $k = 1000s$, mesh refinement level = 2. Red color denotes high value, while blue color denotes low value.



$$t = 0, \max c_s^* = 0/mm^3$$



$$t = 3.0 \times 10^7 s, \max c_s^* = 1089/mm^3$$



$$t = 4.5 \times 10^7 s, \max c_s^* = 1393/mm^3$$

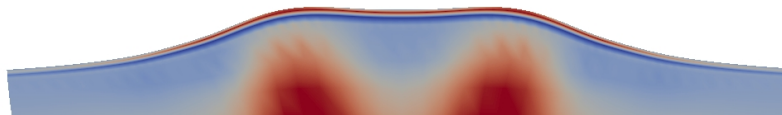
Figure 4.17: Distribution of concentration of foam cells in the solid domain Ω_s^t , with low concentration close to the interface. $k = 1000s$, mesh refinement level = 2. Red color denotes high value, while blue color denotes low value.



$$t = 0, \max \sigma_{s,p} = 0g/mm \cdot s^2$$



$$t = 3.0 \times 10^7 s, \max \sigma_{s,p} = 1099.16g/mm \cdot s^2$$



$$t = 4.5 \times 10^7 s, \max \sigma_{s,p} = 2662.98g/mm \cdot s^2$$

Figure 4.18: Distribution of principal stress in the solid domain Ω_s^t , with high stress value close to the humps of the interface. $k = 1000s$, mesh refinement level = 2. Red color denotes high value, while blue color denotes low value.

4.2. NUMERICAL RESULTS

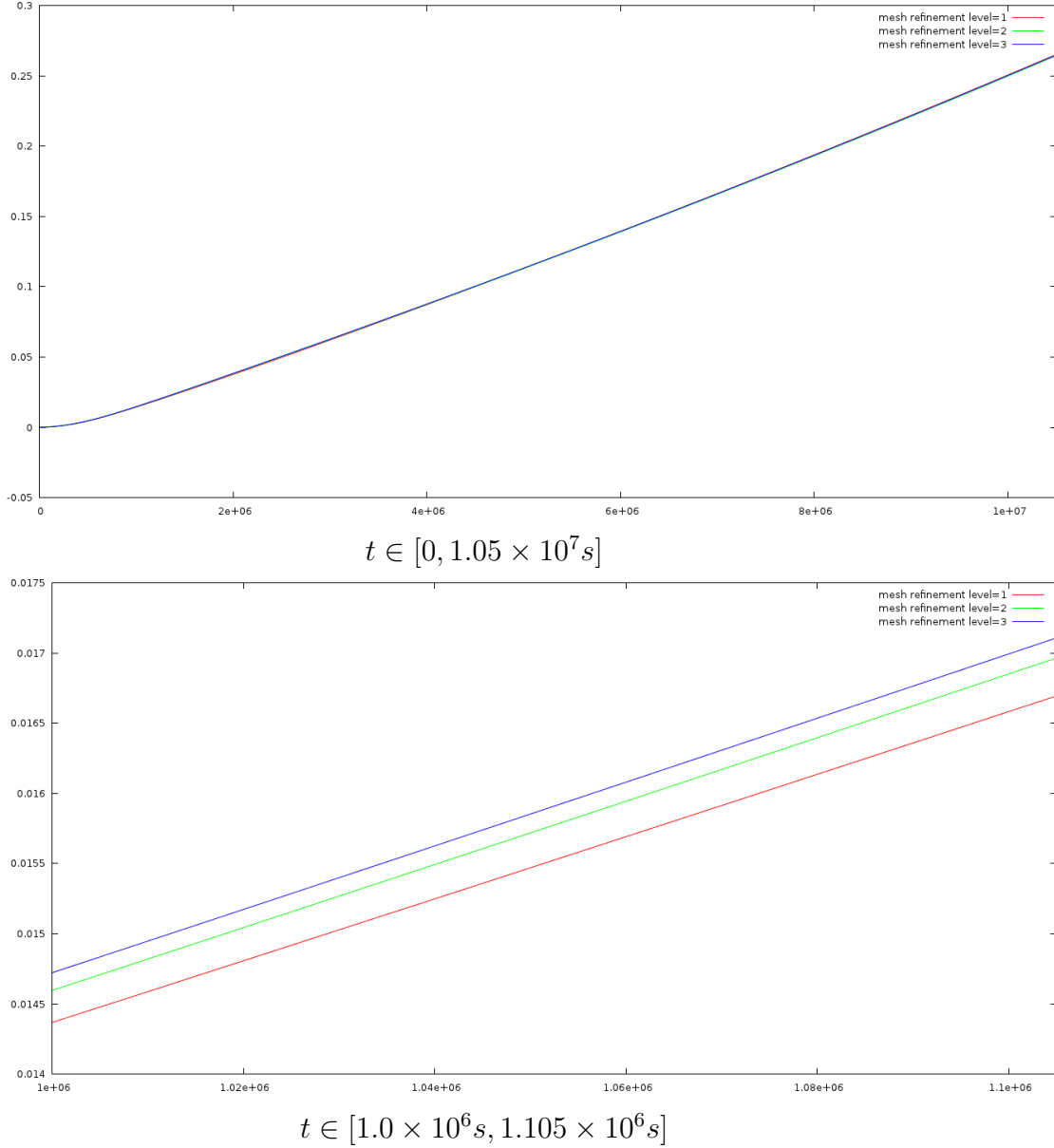


Figure 4.19: Evolution of displacement $u_{s,y}$ at the point $(17.5\text{mm}, 0)$ with different levels of mesh refinement, implying the convergence of numerical solutions as $\hat{h} \rightarrow 0$.

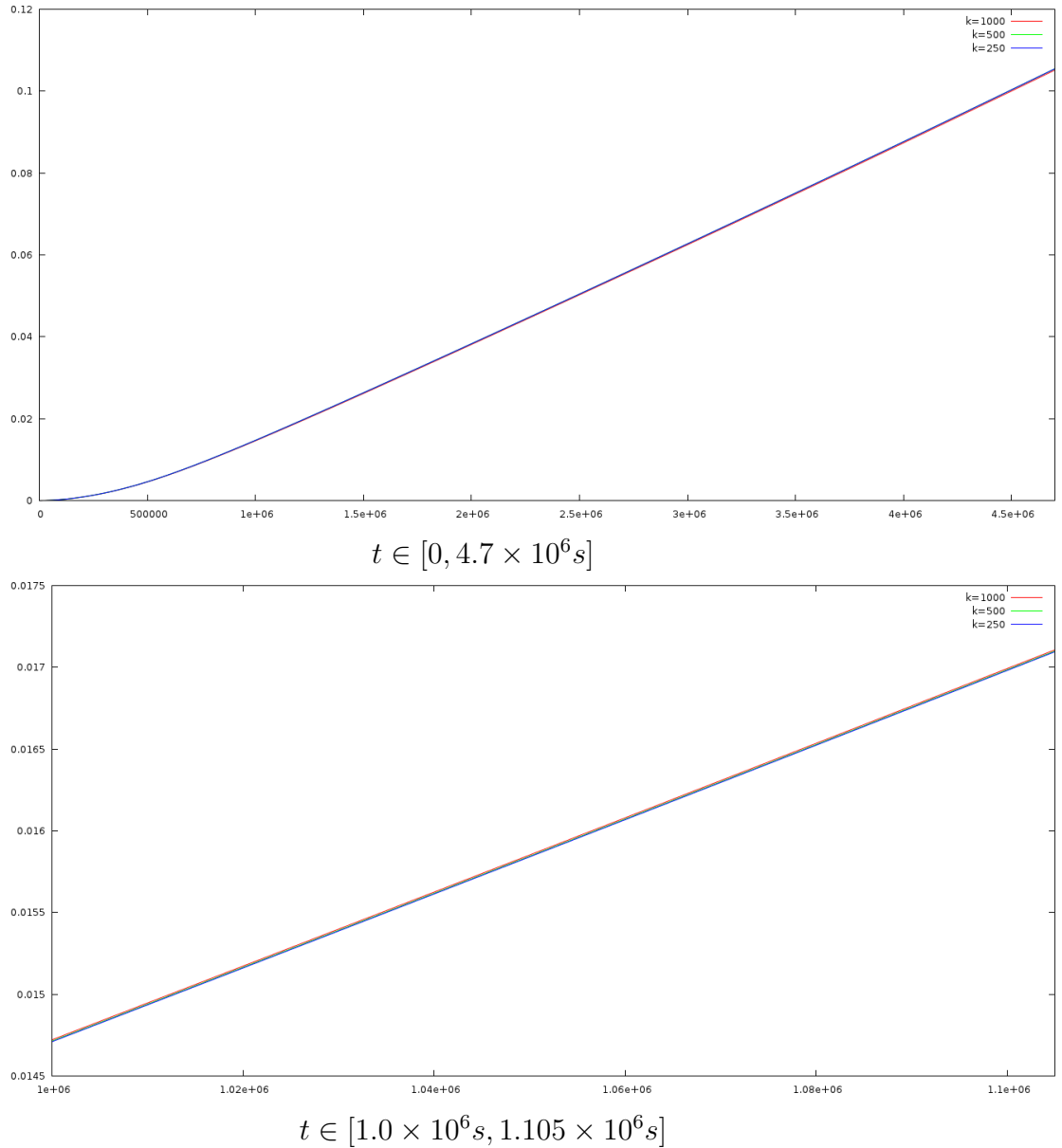
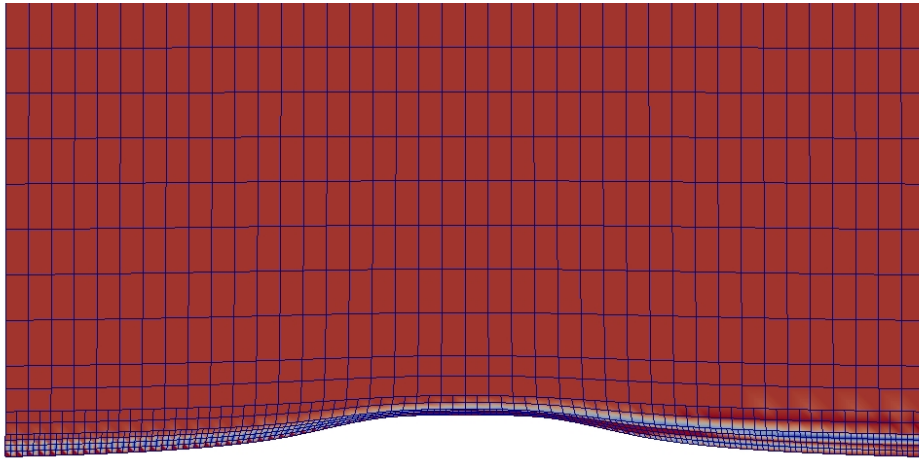


Figure 4.20: Evolution of displacement $u_{s,y}$ at the point $(17.5\text{mm}, 0)$ with different time step sizes, implying the convergence of numerical solutions as $k \rightarrow 0$.



$$t = 3.0 \times 10^7 s$$



without grids

Figure 4.21: Distribution of concentration of monocytes c_f in the model without artificial diffusion term, implying necessity of this stabilization technique.

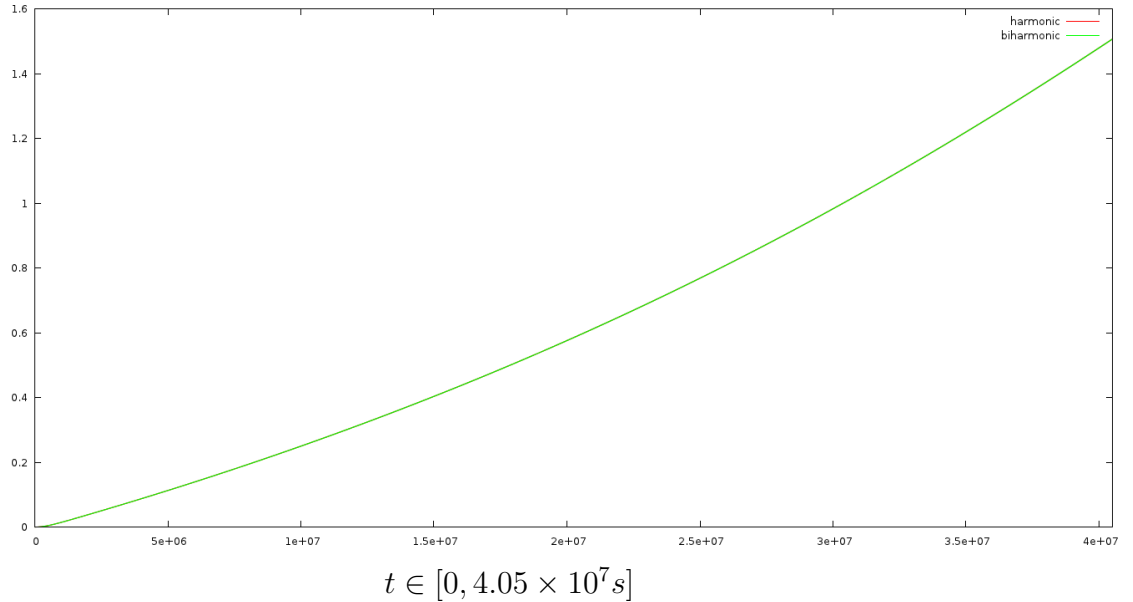


Figure 4.22: Comparison of displacements $u_{s,y}$ at the point $(17.5mm, 0)$ in harmonic and biharmonic extensions.

also moves as the plaque is formed and grows. Especially compared with the results in Example I, after 4.5×10^7 seconds there are two humps on the interface. This is possible from medical point of view because if the diseased part of the vessel wall is long enough there could be more than one specific point of maximum interruption of the blood flow. From the distribution of concentration of monocytes in the fluid domain Ω_f^t in Figure 4.16 and the distribution of concentration of foam cells in the solid domain Ω_s^t in Figure 4.17, we can also get the similar results as in Example I, implying that the penetration of monocytes and the accumulation of foam cells lead to plaque formation and growth. And in Figure 4.17 at time $t = 4.5 \times 10^7 s$, there also exists a thin layer with low concentration of foam cells covering the high concentration region. The distribution of principal stress in the solid domain Ω_s^t is shown in Figure 4.18, where grids are removed to get a clearer observation, and the maximum value is also reached around the humps of the interface especially at time $t = 4.5 \times 10^7 s$. We also try different time step sizes and mesh refinement levels to compare the results, and both Figure 4.19 and Figure 4.20 imply that numerical solutions will converge as $\hat{h} \rightarrow 0$ and $k \rightarrow 0$. Finally Figure 4.21 emphasizes the necessity to add the artificial diffusion term to stabilize the problem.

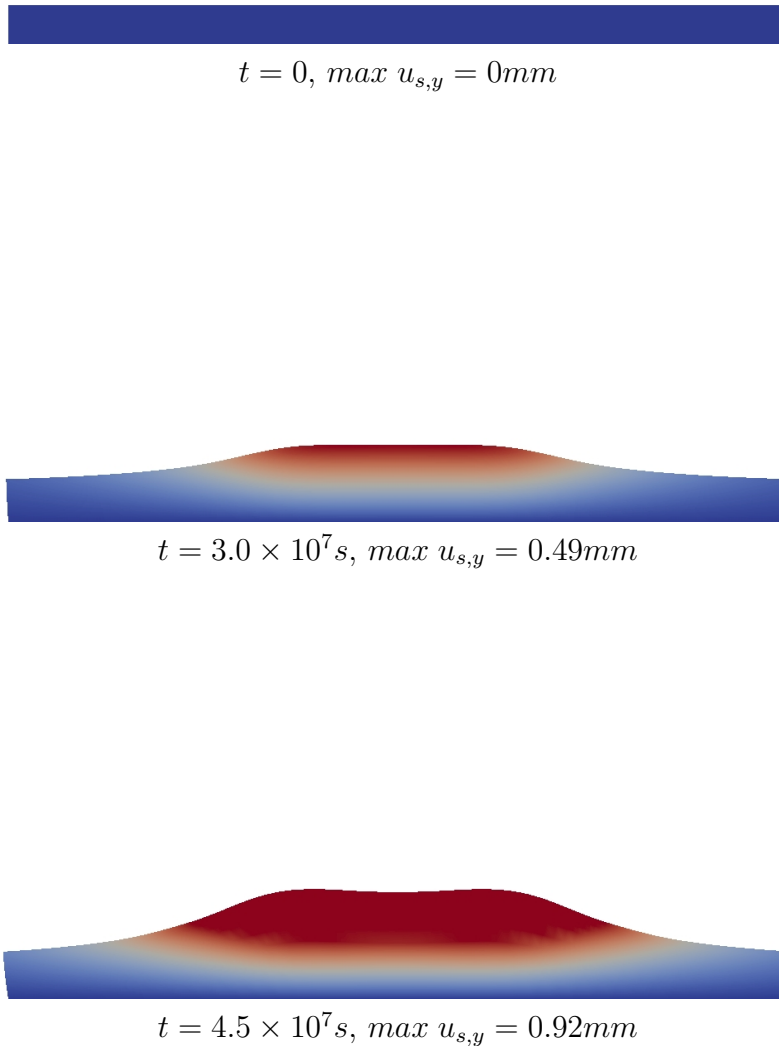
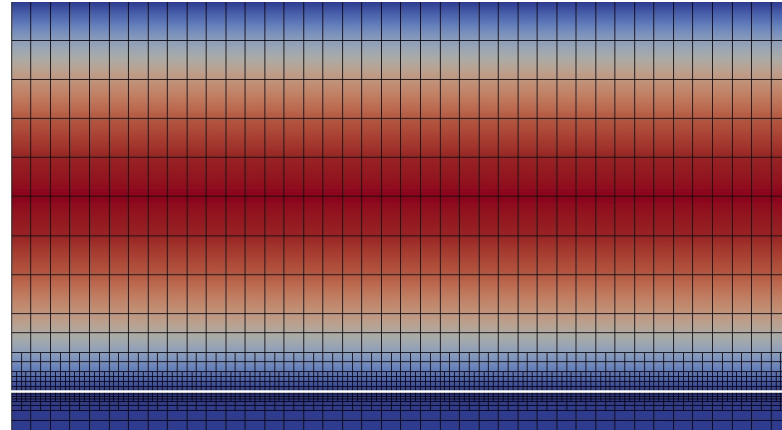
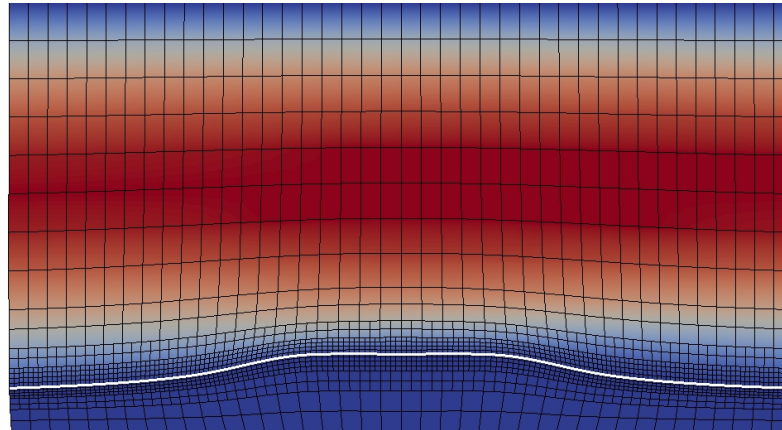


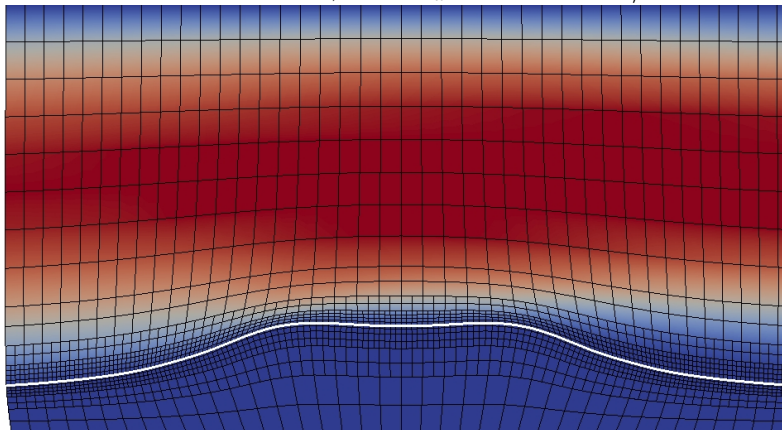
Figure 4.23: Distribution of displacement in y -direction in the solid domain Ω_s^t if biharmonic mesh model is used. $k = 1000s$, mesh refinement level = 2. Red color denotes high value, while blue color denotes low value.



$$t = 0, \max v_x = 300\text{mm/s}$$

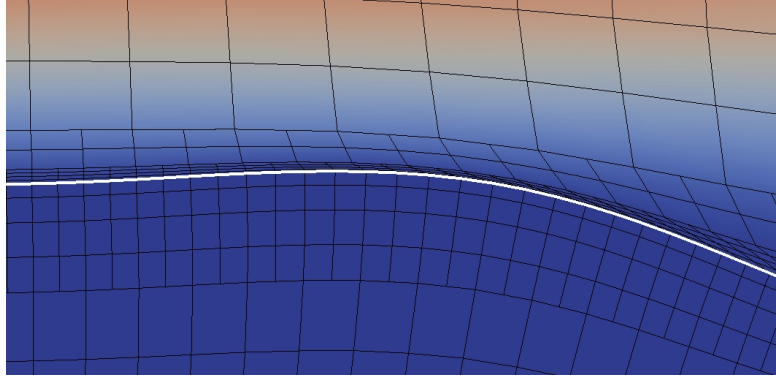


$$t = 3.0 \times 10^7\text{s}, \max v_x = 314.95\text{mm/s}$$

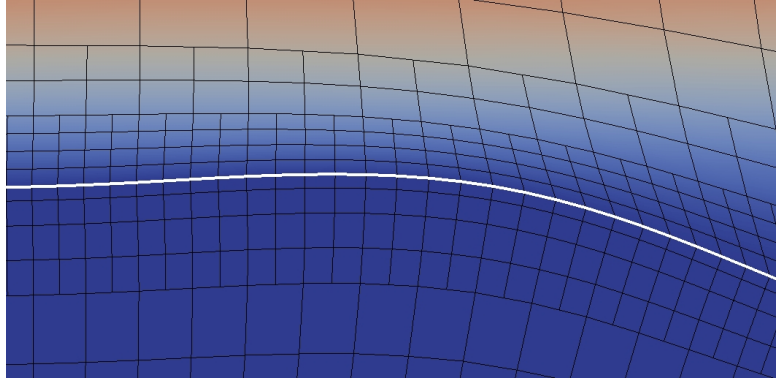


$$t = 4.5 \times 10^7\text{s}, \max v_x = 335.01\text{mm/s}$$

Figure 4.24: Motion of the interface and distribution of velocity in x -direction in the whole domain $\Omega_f^t \cup \Omega_s^t$ if biharmonic mesh model is used. $k = 1000\text{s}$, mesh refinement level = 2. White line indicates the interface. Red color denotes high value, while blue color denotes low value.



Harmonic extension



Biharmonic extension

Figure 4.25: Motion of the interface and distribution of velocity in x -direction v_x near the hump of the interface $\Gamma_1^t \cup \Gamma_2^t$ at $t = 4.5 \times 10^7 s$. Both harmonic and biharmonic mesh models are used, and results are compared, showing better quality of fluid meshes in biharmonic extension. $k = 1000s$, mesh refinement level = 2. White line indicates the interface. Red color denotes high value, while blue color denotes low value.

Remark 4.2.1 (Numerical results of the model with biharmonic mesh model). In Figure 4.14 we can see that under a large deformation, the quality of fluid meshes near the interface is not maintained so well. These meshes are distorted a lot and may be broken quite soon. So it is necessary to use a better mesh model to maintain the fluid mesh quality if we need the numerical results under a larger deformation. Here we try biharmonic model (3.25), and numerical simulations are performed based on the variational formulation derived in Remark 3.2.1. Figure 4.22 and Figure 4.23 show that numerical solutions, especially the displacements $u_{s,y}$ in harmonic and biharmonic extensions, are very close with each other. Comparing Figure 4.24 with Figure 4.14, we can see that the quality of fluid meshes near the interface becomes

much better in biharmonic extension even under a large deformation at time $t = 4.5 \times 10^7 s$. This improvement is observed more clearly in Figure 4.25. Therefore if we need to investigate the evolution of plaques in a longer term, it is better to replace harmonic extension with biharmonic one for numerical simulations.

Chapter 5

Conclusions and outlook

Conclusions

In this thesis, we derived a model describing the formation and evolution of plaques in blood vessels. This physiological process is induced by the penetration of monocytes, which are converted to foam cells in the vessel wall. As the plaque grows due to the accumulation of foam cells, the stresses applied on the vessel wall are increased, and plaque rupture will happen when the critical stress value is reached.

The mathematical model consists of two main parts. To describe the biochemical reaction of monocytes inducing plaque formation we use the convection-diffusion-reaction equation, coupled with an equation for the accumulation of foam cells. For the description of the biomechanical interaction between the blood flow and the vessel wall we use the fluid-structure interaction problem with the Navier-Stokes equations for fluids and the elastic structure equations for solids. These two problems are coupled with growth modeling. The equation for the metric of growth is related to the growth and reaction functions in solids, and the stress tensor in the elastic structure equations is obtained by this variable and the constitutive equations. Moreover the model presents that the increase of the concentration of foam cells not only lets the volume of solid phase grow, but also changes its mechanical properties.

For numerical simulations of this model, the main difficulty is that the interface between the fluid and the solid phase moves due to the growth of plaques, so different meshes are needed for each time step. To treat this problem we formulate the whole system in the ALE framework, so that all the equations are rewritten in the fixed fluid or solid domain. The extension of the displacement to the fluid domain, which is used to define the ALE

mapping, can be obtained by different mesh models. Theoretically, the numerical stability of the system is an open question, but the energy estimate is achieved in a simplified model.

Based on the variational formulation of the model derived in the ALE framework, numerical simulations are performed by using the finite element library Gascoigne. Temporal discretization is achieved with the implicit backward Euler scheme, and spatial discretization is based on the Galerkin finite element method. The nonlinear problems are linearized and solved by the Newton method. We present numerical results in two examples. Example I has a simple computational domain and is considered a test of the model. Example II has a configuration which is much closer to a real artery. In both of the two examples the distribution of the velocity, displacement, concentrations and stress value are visualized. The obtained numerical results show that the concentration of foam cells is very high at the place under a large deformation, implying that the accumulation of foam cells leads to the formation and growth of plaques. We also observe that the stresses reach the maximum value around the hump of the interface, confirming that the evolution of plaques induces the increase of stresses in the vessel wall, which is a possible indicator of plaque rupture. We try different time step sizes and mesh refinement levels to show the convergence of numerical solutions. Comparing the results also shows that the local mesh refinement near the interface and the artificial stabilization techniques are necessary in order to get more stable and accurate solutions.

Outlook

First, both the modeling and simulation of our problem should be improved to study the behavior of plaque formation in more realistic environments. Some possible future research ideas follow here:

- Since the plaque formation also happens in blood vessels with small diameter, the non-Newtonian fluid should also be considered for fluid dynamics^[21;45].
- Periodic heart beats, inducing the motion of blood in arteries and letting the velocity of the blood flow have periodic oscillations^[46], should also be taken into account. Since simulations are performed over a long-time period, this short oscillation can not be numerically resolved because of different time scales. The methods of asymptotic analysis are used to determine an efficient model by averaging oscillations induced by heart beats.

-
- More realistic description of the vessel wall including the fibrous structure and orientation should be considered in structure modeling^[34]. And more information about the change of its mechanical properties during the dynamics of the process is also needed.
 - More efficient modeling and simulation should be supported by more accurate experimental data. Let the biochemical reaction be an example, and based on sufficient experimentally determined values of the concentration of foam cells, the width of the diseased vessel wall, etc., we can estimate the parameters such as the reaction and growth coefficients by implementing optimization strategies. Furthermore we may also be able to improve the reaction function by replacing the linear reaction rate with a nonlinear one, or even by adding more biochemical properties, e.g. the concentrations of LDLs and HDLs. The former ones carry lipids into macrophages and the other ones carry them away from these cells, playing important but opposite roles in plaque formation^[23]. In this situation, numerical simulations permit not just the formation and growth, but also the regression and disappearance of plaques, which have wider applications to atherosclerosis.

Moreover the model derived in this thesis is not only supposed to be used to describe the physiological processes of plaque evolution, but can also be considered as a model describing the interaction of reactive flow with solid phase in general, which is an important aspect of various applications.

Second, from the numerical point of view, it has been shown from recent numerical results that simulations with harmonic extension have some limits because fluid meshes have a large distortion near the interface under a large deformation. As is shown in Remark 4.2.1, the quality of fluid meshes near the interface is maintained much better in biharmonic extension, so that in order to investigate the evolution of plaques for a longer period, it is necessary to perform numerical simulations based on biharmonic mesh model. Furthermore, a new variational formulation called the Fully Eulerian formulation of our model can also be taken into account. The whole system is formulated in the Fully Eulerian framework, where the meshes are all fixed, while the interface is movable and is determined implicitly by solutions. Therefore there is no mesh distortion under a large deformation of the interface^[57;58;80]. This is the main advantage of the Fully Eulerian formulation compared to the ALE, and if we can overcome the main problem about how to determine the interface, long-term numerical simulations can also be performed with the help of the Fully Eulerian approach. In addition, developing a three-dimensional simulation tool is also very important to get numerical results

in a configuration much closer to a real artery.

Last but not least, there are still many interesting theoretical questions which have arisen from the model. The well-posedness of the model is a point of great interest. Moreover in the general formula of the energy estimate of our model (3.65), the existence of several so far noncontrollable terms makes the stability of the system unclear, so it is possible for the solution of our model to be singular at a finite time. Singularities of the solution have to be expected, because it can be considered as an evidence of plaque rupture when plaques are formed and growing without any control, and it should be not just analyzed but also validated by numerical simulations for a longer period.

Acknowledgements

At first, I would like to express my deepest gratitude to my supervisors Prof. Willi Jäger, Prof. Maria Neuss-Radu and Prof. Thomas Richter. I would like to thank Prof. Willi Jäger for guiding me into this interesting and challenging research field, for providing a lot of suggestions and help for my project, and for giving me the opportunity to present my research at international conferences (especially for writing several letters of recommendation for travel grants from the HGS and the Graduate Academy). I also would like to thank Prof. Maria Neuss-Radu for many valuable discussions and suggestions concerning my work, especially a wealth of details in my PhD project such as deriving models, writing papers, giving presentations, and not least for taking an active interest in both my work and life even after she left Heidelberg. Furthermore, I would like to thank Prof. Thomas Richter for invaluable help about numerics in my work, from a basic course of the finite element library Gascoigne, to various questions about computation and visualization, as well as for spending a lot of time in helping me to perform numerical simulations in his office.

Secondly, I would like to acknowledge Prof. Michael Hennerici from the Faculty of Medicine, University of Heidelberg for discussions on plaque formation from the medical point of view. I also would like to thank Dr. Jeremi Mizerski from the University of Warsaw for suggestions about configuration and parameter determination for numerical simulations. Furthermore, I would like to thank Prof. Peter Bastian (who was also my second supervisor in the first year of my PhD) for his care, especially for supporting me in attending the 2013 SIAM Conference on Mathematical and Computational Issues in the Geosciences in Padua. Last, I would like to thank Dr. Thomas Wick from The University of Texas at Austin for fruitful discussions on our works, from which I've got many useful details for the thesis and new ideas for the future work.

Additionally, I acknowledge the funding of my PhD at the Faculty of Math-

CHAPTER 5. CONCLUSIONS AND OUTLOOK

ematics and Computer Science of Heidelberg University through the Heidelberg Graduate School of Mathematical and Computational Methods for the Sciences (HGS) from the state of Baden-Württemberg and the German Research Foundation (DFG). I am also grateful for having become a member of the HGS.

Moreover, I wish to thank all my colleagues in the Applied Analysis Group, no matter whether they have left or are still in Heidelberg, for the nice time we have spent together. And I also would like to thank everyone who has given me help during my study, research and daily life in Heidelberg for the past four years.

Last but not least, I would like to thank my parents for their ongoing support and deep love in various forms, even with a distance of more than 7 thousand kilometers between us.

List of Figures

1.1	Vascular bifurcation and flow patterns. From C. Hahn and M. A. Schwartz ^[23]	6
1.2	Formation of an atherosclerotic plaque. From C. Hahn and M. A. Schwartz ^[23]	7
1.3	Histology of an eccentric, fatty, coronary plaque. From A. Sambola et al. ^[62]	9
1.4	A thrombus superimposed on a lipid-rich atherosclerotic plaque. From G. K. Hansson ^[24]	10
2.1	Computational domain	17
2.2	Deformation and displacement in the Lagrangian framework. Modified from A. Quarteroni and L. Formaggia ^[45]	19
2.3	A thought experiment to show how growth may falsify the usual way of quantifying the deformation. From I. Doktorski ^[11]	39
2.4	Decomposition of deformation gradient. Modified from I. Doktorski ^[11]	39
4.1	Configuration of the computational domain in Example I	96
4.2	Motion of the interface and distribution of velocity in x -direction in the whole domain $\Omega_f^t \cup \Omega_s^t$. $k = 1000s$, mesh refinement level = 3. White line indicates the interface. Red color denotes high value, while blue color denotes low value.	99
4.3	Distribution of displacement in y -direction in the solid domain Ω_s^t . $k = 1000s$, mesh refinement level = 3. Red color denotes high value, while blue color denotes low value.	100
4.4	Distribution of concentration of monocytes in the fluid domain Ω_f^t . $k = 1000s$, mesh refinement level = 3. Red color denotes high value, while blue color denotes low value.	101
4.5	Distribution of concentration of foam cells in the solid domain Ω_s^t . $k = 1000s$, mesh refinement level = 3. Red color denotes high value, while blue color denotes low value.	102

4.6	Distribution of principal stress in the solid domain Ω_s^t . $k = 1000s$, mesh refinement level = 3. Red color denotes high value, while blue color denotes low value.	103
4.7	Evolution of displacement $u_{s,y}$ at the point $(2.5mm, 0)$ with different levels of mesh refinement, implying the convergence of numerical solutions as $\hat{h} \rightarrow 0$	104
4.8	Evolution of displacement $u_{s,y}$ at the point $(2.5mm, 0)$ with different time step sizes, implying the convergence of numerical solutions as $k \rightarrow 0$	105
4.9	Distribution of concentration of monocytes c_f in the model without artificial diffusion term, implying necessity of this stabilization technique.	106
4.10	Motion of the interface and distribution of velocity in x -direction in the whole domain $\Omega_f^t \cup \Omega_s^t$ if the incompressible Mooney-Rivlin material is considered. $k = 1000s$, mesh refinement level = 3. White line indicates the interface. Red color denotes high value, while blue color denotes low value.	108
4.11	Distribution of displacement in y -direction in the solid domain Ω_s^t if the incompressible Mooney-Rivlin material is considered. $k = 1000s$, mesh refinement level = 3. Red color denotes high value, while blue color denotes low value.	109
4.12	Comparison of displacements $u_{s,y}$ at the point $(2.5mm, 0)$ in the incompressible neo-Hookean material (INH) and the incompressible Mooney-Rivlin material (IMR).	110
4.13	Configuration of the computational domain in Example II	111
4.14	Motion of the interface and distribution of velocity in x -direction in the whole domain $\Omega_f^t \cup \Omega_s^t$. $k = 1000s$, mesh refinement level = 2. White line indicates the interface. Red color denotes high value, while blue color denotes low value.	112
4.15	Distribution of displacement in y -direction in the solid domain Ω_s^t . $k = 1000s$, mesh refinement level = 2. Red color denotes high value, while blue color denotes low value.	113
4.16	Distribution of concentration of monocytes in the fluid domain Ω_f^t . $k = 1000s$, mesh refinement level = 2. Red color denotes high value, while blue color denotes low value.	114
4.17	Distribution of concentration of foam cells in the solid domain Ω_s^t , with low concentration close to the interface. $k = 1000s$, mesh refinement level = 2. Red color denotes high value, while blue color denotes low value.	115

4.18	Distribution of principal stress in the solid domain Ω_s^t , with high stress value close to the humps of the interface. $k = 1000s$, mesh refinement level = 2. Red color denotes high value, while blue color denotes low value.	116
4.19	Evolution of displacement $u_{s,y}$ at the point $(17.5mm, 0)$ with different levels of mesh refinement, implying the convergence of numerical solutions as $\hat{h} \rightarrow 0$	117
4.20	Evolution of displacement $u_{s,y}$ at the point $(17.5mm, 0)$ with different time step sizes, implying the convergence of numerical solutions as $k \rightarrow 0$	118
4.21	Distribution of concentration of monocytes c_f in the model without artificial diffusion term, implying necessity of this stabilization technique.	119
4.22	Comparison of displacements $u_{s,y}$ at the point $(17.5mm, 0)$ in harmonic and biharmonic extensions.	120
4.23	Distribution of displacement in y -direction in the solid domain Ω_s^t if biharmonic mesh model is used. $k = 1000s$, mesh refinement level = 2. Red color denotes high value, while blue color denotes low value.	121
4.24	Motion of the interface and distribution of velocity in x -direction in the whole domain $\Omega_f^t \cup \Omega_s^t$ if biharmonic mesh model is used. $k = 1000s$, mesh refinement level = 2. White line indicates the interface. Red color denotes high value, while blue color denotes low value.	122
4.25	Motion of the interface and distribution of velocity in x -direction v_x near the hump of the interface $\Gamma_1^t \cup \Gamma_2^t$ at $t = 4.5 \times 10^7s$. Both harmonic and biharmonic mesh models are used, and results are compared, showing better quality of fluid meshes in biharmonic extension. $k = 1000s$, mesh refinement level = 2. White line indicates the interface. Red color denotes high value, while blue color denotes low value.	123

LIST OF FIGURES

List of Tables

4.1	Output of computational information in the 2-nd time step. From T. Richter ^[54]	94
4.2	Outputs of computational information by different temporal discretizations in the time step $[1.74 \times 10^5 s, 1.75 \times 10^5 s]$	97

LIST OF TABLES

Bibliography

- [1] R. A. Adams. *Sobolev Spaces*. Academic Press, 1975.
- [2] L. Ai and K. Vafai. A coupling model for macromolecule transport in a stenosed arterial wall. *International Journal of Heat and Mass Transfer*, 49:1568 – 1591, 2006.
- [3] D. Ambrosi and F. Mollica. On the mechanics of a growing tumor. *International Journal of Engineering Science*, 40(12):1297 – 1316, 2002.
- [4] K. E. Barrett, S. Boitano, S. M. Barman, and H. L. Brooks. *Ganongs Review of Medical Physiology, 23rd Edition*. McGraw Hill Professional, 2010.
- [5] K. J. Bathe. *Finite Element Procedures*. New Jersey: Prentice Hall, 1996.
- [6] Y. Bazilevs, V. Calo, T. Hughes, and Y. Zhang. Isogeometric fluid-structure interaction: theory, algorithms, and computations. *Computational Mechanics*, 43:3–37, 2008.
- [7] J. Boyd, J. M. Buick, and S. Green. Analysis of the Casson and Carreau-Yasuda non-Newtonian blood models in steady and oscillatory flows using the lattice Boltzmann method. *Physics of Fluids*, 19(9):093103, 2007.
- [8] A. N. Brooks and T. J. Hughes. Streamline upwind/Petrov-Galerkin formulations for convection dominated flows with particular emphasis on the incompressible Navier-Stokes equations. *Computer Methods in Applied Mechanics and Engineering*, 32(1):199 – 259, 1982.
- [9] P. G. Ciarlet. *Mathematical Elasticity, Vol.I: Three-Dimensional Elasticity*. North-Holland, Amsterdam, 1988.

BIBLIOGRAPHY

- [10] D. Coutand and S. Shkoller. Motion of an elastic solid inside an incompressible viscous fluid. *Archive for Rational Mechanics and Analysis*, 176:25–102, 2005.
- [11] I. Doktorski. Mechanical Model for Biofilm Growth Phase. Dissertation, University of Heidelberg, 2007.
- [12] T. Dunne, R. Rannacher, and T. Richter. Numerical simulation of fluid-structure interaction based on monolithic variational formulations. In G. P. Galdi and R. Rannacher, editors, *Fundamental Trends in Fluid-Structure Interaction*, volume 1 of *Contemporary Challenges in Mathematical Fluid Dynamics and Its Applications*, pages 1–75. World Scientific, 2010.
- [13] C. R. Ethier. Computational modeling of mass transfer and links to atherosclerosis. *Annals of Biomedical Engineering*, 30:461–471, 2002.
- [14] L. C. Evans. *Partial Differential Equations*. American Mathematical Society, 1998.
- [15] E. Falk, P. K. Shah, and V. Fuster. Coronary plaque disruption. *Circulation*, 92(3):657–671, 1995.
- [16] M. A. Fernández, L. Formaggia, J.-F. Gerbeau, and A. Quarteroni. The derivation of the equations for fluids and structure. In L. Formaggia, A. Quarteroni, A. Veneziani, A. Quarteroni, T. Hou, C. Bris, A. T. Patera, and E. Zuazua, editors, *Cardiovascular Mathematics*, volume 1, pages 77–121. Springer Milan, 2009.
- [17] A. L. Fogelson. Continuum models of platelet aggregation: Formulation and mechanical properties. *SIAM Journal on Applied Mathematics*, 52(4):pp. 1089–1110, 1992.
- [18] L. Formaggia, A. Moura, and F. Nobile. On the stability of the coupling of 3D and 1D fluid-structure interaction models for blood flow simulations. *ESAIM: Mathematical Modelling and Numerical Analysis*, 41(04):743–769, 2007.
- [19] L. Formaggia and F. Nobile. A stability analysis for the arbitrary Lagrangian Eulerian formulation with finite elements,. *East-West Journal of Numerical Mathematics*, 7(2):105–131, 1999.
- [20] Y.-c. Fung. *Biodynamics: Circulation*. Springer-Verlag, 1984.

-
- [21] G. P. Galdi. Mathematical problems in classical and non-Newtonian fluid mechanics. In G. Galdi, R. Rannacher, A. Robertson, and S. Turek, editors, *Hemodynamical Flows: Modeling, Analysis and Simulation*, volume 37 of *Oberwolfach Seminars*, pages 121–273. Springer, 2008.
- [22] M. E. Gurtin. *An Introduction to Continuum Mechanics*. Academic Press, 1981.
- [23] C. Hahn and M. A. Schwartz. Mechanotransduction in vascular physiology and atherogenesis. *Nat Rev Mol Cell Biol*, 10:53–62, 2009.
- [24] G. K. Hansson. Inflammation, atherosclerosis, and coronary artery disease. *New England Journal of Medicine*, 352(16):1685–1695, 2005. PMID: 15843671.
- [25] G. Holzapfel. *Nonlinear Solid Mechanics. A Continuum Approach for Engineering*. John Wiley & Sons, Chichester, 2000.
- [26] G. Holzapfel, T. Gasser, and R. Ogden. A new constitutive framework for arterial wall mechanics and a comparative study of material models. *Journal of Elasticity*, 61:1–48, 2000.
- [27] G. A. Holzapfel and R. W. Ogden. Constitutive modelling of arteries. *Proceedings of the Royal Society A: Mathematical, Physical and Engineering Science*, 466(2118):1551–1597, 2010.
- [28] G. A. Holzapfel, M. Stadler, and C. A. J. Schulze-Bauer. A layer-specific three-dimensional model for the simulation of balloon angioplasty using magnetic resonance imaging and mechanical testing. *Annals of Biomedical Engineering*, 30:753–767, 2002.
- [29] J. Hron and S. Turek. A monolithic FEM/multigrid solver for an ALE formulation of fluid-structure interaction with applications in biomechanics. In H.-J. Bungartz and M. Schäfer, editors, *Fluid-Structure Interaction: Modelling, Simulation, Optimisation*, volume 53 of *Lecture Notes in Computational Science and Engineering*, pages 146–170. Springer, 2006.
- [30] J. D. Humphrey. *Cardiovascular Solid Mechanics: Cells, Tissues, and Organs*. Springer, 2002.
- [31] A. I. Ibragimov, C. J. McNeal, L. R. Ritter, and J. R. Walton. A mathematical model of atherogenesis as an inflammatory response. *Mathematical Medicine and Biology*, 22(4):305–333, December 2005.

BIBLIOGRAPHY

- [32] J. Janela, A. Moura, and A. Sequeira. A 3D non-Newtonian fluid-structure interaction model for blood flow in arteries. *Journal of Computational and Applied Mathematics*, 234(9):2783 – 2791, 2010.
- [33] C. Johnson. *Numerical Solution of Partial Differential Equations by the Finite Element Method*. Cambridge University Press, 1987.
- [34] P. Kalita and R. Schaefer. Mechanical models of artery walls. *Archives of Computational Methods in Engineering*, 15(1):1–36, 2007.
- [35] C. L. Lendon, M. Davies, G. Born, and P. Richardson. Atherosclerotic plaque caps are locally weakened when macrophages density is increased. *Stroke*, 87:87–90, 1991.
- [36] Z.-Y. Li, S. P. Howarth, T. Tang, and J. H. Gillard. How critical is fibrous cap thickness to carotid plaque stability? *Stroke*, 37(5):1195–1199, 2006.
- [37] V. Lubarda and A. Hoger. On the mechanics of solids with a growing mass. *International Journal of Solids and Structures*, 39(18):4627 – 4664, 2002.
- [38] A. Moura. The Geometrical Multiscale Modelling of the Cardiovascular System: Coupling 3D FSI and 1D Models. PhD thesis, Instituto Superior Técnico, Technical University of Lisbon, 2007.
- [39] F. Nobile. Numerical Approximation of Fluid-Structure Interaction Problems with Applications to Haemodynamics. PhD thesis, École Polytechnique Fédérale de Lausanne, 2001.
- [40] R. W. Ogden. Anisotropy and nonlinear elasticity in arterial wall mechanics. In G. A. Holzapfel and R. W. Ogden, editors, *Biomechanical Modelling at the Molecular, Cellular and Tissue Levels*, volume 508 of *CISM Courses and Lectures*, pages 179–258. Springer Vienna, 2009.
- [41] A. Ougrinovskaia, R. Thompson, and M. Myerscough. An ODE model of early stages of atherosclerosis: Mechanisms of the inflammatory response. *Bulletin of Mathematical Biology*, 72:1534–1561, 2010.
- [42] G. Pasterkamp and E. Falk. Atherosclerotic plaque rupture: an overview. *Journal of Clinical and Basic Cardiology*, 3:81–86, 2000.
- [43] M. Prosi, P. Zunino, K. Perktold, and A. Quarteroni. Mathematical and numerical models for transfer of low-density lipoproteins through

- the arterial walls: a new methodology for the model set up with applications to the study of disturbed luminal flow. *Journal of Biomechanics*, 38(4):903 – 917, 2005.
- [44] A. Quarteroni. Fluid-structure interaction between blood and arterial walls. In G. P. Galdi and R. Rannacher, editors, *Fundamental Trends in Fluid-Structure Interaction*, volume 1 of *Contemporary Challenges in Mathematical Fluid Dynamics and Its Applications*, pages 261–289. World Scientific, 2010.
- [45] A. Quarteroni and L. Formaggia. Mathematical modelling and numerical simulation of the cardiovascular system. *Handbook of numerical analysis*, 12:3C127, 2004.
- [46] A. Quarteroni, M. Tuveri, and A. Veneziani. Computational vascular fluid dynamics: problems, models and methods. *Computing and Visualization in Science*, 2(4):163–97, 2000.
- [47] A. Quarteroni and A. Valli. *Numerical approximation of partial differential equations*. Springer-Verlag, Berlin, 1994.
- [48] A. Quarteroni, A. Veneziani, and P. Zunino. Mathematical and numerical modeling of solute dynamics in blood flow and arterial walls. *SIAM J. Numer. Anal.*, 39(5):1488–1511, May 2001.
- [49] K. Rajagopal and A. Srinivasa. Mechanics of the inelastic behavior of materials. part 1, theoretical underpinnings. *International Journal of Plasticity*, 14(10, 11):945 – 967, 1998.
- [50] K. Rajagopal and A. Srinivasa. Mechanics of the inelastic behavior of materials. part II: inelastic response. *International Journal of Plasticity*, 14(10, 11):969 – 995, 1998.
- [51] R. Rannacher. Numerische Methoden fuer Probleme der Kontinuumsmechanik. Heidelberg, <http://numerik.uni-hd.de/lehre/notes/>, 2008, Vorlesungsskriptum.
- [52] H. B. Ravn and E. Falk. Histopathology of Plaque Rupture. *Cardiology Clinics*, 17(2):263 – 270, 1999.
- [53] T. Richter. Numerical methods for fluid-structure interaction problems. Heidelberg, <http://numerik.uni-hd.de/richter/SS10/fsi/>, 2010, Vorlesungsskriptum.

BIBLIOGRAPHY

- [54] T. Richter. Gascoigne. Heidelberg, <http://numerik.uni-hd.de/richter/SS11/gascoigne/index.html>, 2011, Vorlesungsskriptum.
- [55] T. Richter. Numerical methods for fluid-structure interactions. Heidelberg, <http://numerik.uni-hd.de/richter/WS12/fsi/index.html>, 2012, Vorlesungsskriptum.
- [56] T. Richter. Numerische Methoden der Stroemungsmechanik. Heidelberg, <http://numerik.uni-hd.de/richter/WS11/numerik3/index.html>, 2012, Vorlesungsskriptum.
- [57] T. Richter. A fully Eulerian formulation for fluid-structure-interaction problems. *Journal of Computational Physics*, 233(0):227 – 240, 2013.
- [58] T. Richter and T. Wick. Finite elements for fluid-structure interaction in ALE and fully Eulerian coordinates. *Computer Methods in Applied Mechanics and Engineering*, 199(41-44):2633 – 2642, 2010.
- [59] A. M. Robertson. Review of relevant continuum mechanics. In G. Galdi, R. Rannacher, A. Robertson, and S. Turek, editors, *Hemodynamical Flows: Modeling, Analysis and Simulation*, volume 37 of *Oberwolfach Seminars*, pages 1–62. Springer, 2008.
- [60] A. M. Robertson, A. Sequeira, and M. V. Kameneva. Hemorheology. In G. Galdi, R. Rannacher, A. Robertson, and S. Turek, editors, *Hemodynamical Flows: Modeling, Analysis and Simulation*, volume 37 of *Oberwolfach Seminars*, pages 63–120. Springer, 2008.
- [61] R. Ross. The pathogenesis of atherosclerosis: a perspective for the 1990s. *Nature*, 362:801 – 809, 1993.
- [62] A. Sambola, V. Fuster, and J. J. Badimon. Role of coronary risk factors in blood thrombogenicity and acute coronary syndromes. *Rev Esp Cardiol*, 56(10):1001 – 1009, 2003.
- [63] D. M. Small. George Lyman Duff memorial lecture. Progression and regression of atherosclerotic lesions. Insights from lipid physical biochemistry. *Arteriosclerosis, Thrombosis, and Vascular Biology*, 8(2):103–29, 1988.
- [64] H. C. Stary. Lipid and macrophage accumulations in arteries of children and the development of atherosclerosis. *The American Journal of Clinical Nutrition*, 72:1297S–1306S, 2000.

- [65] K. Stein, T. Tezduyar, and R. Benney. Mesh moving techniques for fluid-structure interactions with large displacements. *Journal of Applied Mechanics*, 70(January):58–63, 2003.
- [66] D. Steinberg. Low density lipoprotein oxidation and its pathobiological significance. *Journal of Biological Chemistry*, 272(34):20963–20966, 1997.
- [67] D. Tang, C. Yang, S. Kobayashi, and D. N. Ku. Effect of a lipid pool on stress/strain distributions in stenotic arteries: 3-D fluid-structure interactions (FSI) models. *Journal of Biomechanical Engineering*, 126(3):363–370, 2004.
- [68] D. Tang, C. Yang, S. Kobayashi, J. Zheng, P. K. Woodard, Z. Teng, K. Billiar, R. Bach, and D. N. Ku. 3D MRI-based anisotropic FSI models with cyclic bending for human coronary atherosclerotic plaque mechanical analysis. *Journal of Biomechanical Engineering*, 131(6):061010, 2009.
- [69] D. Tang, C. Yang, S. Mondal, F. Liu, G. Canton, T. S. Hatsukami, and C. Yuan. A negative correlation between human carotid atherosclerotic plaque progression and plaque wall stress: In vivo MRI-based 2D/3D FSI models. *Journal of Biomechanics*, 41(4):727 – 736, 2008.
- [70] D. Tang, C. Yang, J. Zheng, P. K. Woodard, G. A. Sicard, J. E. Saffitz, and C. Yuan. 3D MRI-based multicomponent FSI models for atherosclerotic plaques. *Annals of Biomedical Engineering*, 32:947–960, 2004.
- [71] R. Temam. *Navier-Stokes Equations, Theory And Numerical Analysis*. North-Holland, Amsterdam, 2 edition edition, 1979.
- [72] T. E. Tezduyar, M. Behr, S. Mittal, and A. A. Johnson. Computation of unsteady incompressible flows with the stabilized finite element methods: Space-time formulations, iterative strategies and massively parallel implementations. *ASME*, 246:7–24, 1992.
- [73] J. S. VanEpps and D. A. Vorp. Mechanopathobiology of atherogenesis: A review. *Journal of Surgical Research*, 142(1):202 – 217, 2007.
- [74] F. Weller. Modeling, Analysis, and Simulation of Thrombosis and Hemostasis. PhD thesis, University of Heidelberg, 2008.
- [75] F. Weller. Platelet deposition in non-parallel flow. *Journal of Mathematical Biology*, 57:333–359, 2008.

BIBLIOGRAPHY

- [76] F. Weller. A free boundary problem modeling thrombus growth. *Journal of Mathematical Biology*, 61:805–818, 2010.
- [77] F. Weller, M. Neuss-Radu, and W. Jäger. Analysis of a free boundary problem modeling thrombus growth. *SIAM Journal on Mathematical Analysis*, 45(2):809–833, 2013.
- [78] T. Wick. Adaptive Finite Element Simulation of Fluid-Structure Interaction with Application to Heart-Valve Dynamics. PhD thesis, University of Heidelberg, 2011.
- [79] T. Wick. Fluid-structure interactions using different mesh motion techniques. *Computers and Structures*, 89(13-14):1456–1467, 2011.
- [80] T. Wick. Fully Eulerian fluid-structure interaction for time-dependent problems. *Computer Methods in Applied Mechanics and Engineering*, 255(0):14 – 26, 2013.
- [81] K. J. Williams, J. E. Feig, and E. A. Fisher. Rapid regression of atherosclerosis: insights from the clinical and experimental literature. *Nat Clin Pract Cardiovasc Med*, 5:91–102, 2008.
- [82] C. Yang, R. Bach, J. Zheng, I. Ei Naqa, P. Woodard, Z. Teng, K. Biliar, and D. Tang. In vivo IVUS-based 3-D fluid-structure interaction models with cyclic bending and anisotropic vessel properties for human atherosclerotic coronary plaque mechanical analysis. *Biomedical Engineering, IEEE Transactions on*, 56(10):2420 –2428, oct. 2009.
- [83] Y. Yang and M. Neuss-Radu. Interaction of reactive flow with solid phase, leading to changes in volume and mechanical properties – mathematical modeling and simulation. In *reports on the invitation of international meetings, SIAM Conference on Mathematical and Computational Issues in the Geosciences, Padua, Italy, 2013*.
- [84] Y. Yang and M. Neuss-Radu. Mathematical modeling and simulation of the formation and evolution of plaques in blood vessels. In *reports on the invitation of international meetings, COMPLAS XI: Novel Computational Approaches in Biomechanics at Different Length Scales, Barcelona, Spain, 2011*.
- [85] Y. Yang and M. Neuss-Radu. Mathematical modeling and simulation of the formation and evolution of plaques in blood vessels. In *reports on the invitation of international meetings, 8th European Solid Mechanics Conference, Graz, Austria, 2012*.

- [86] M. Zamir. *The Physics of Coronary Blood Flow*. Biological and Medical Physics, Biomedical Engineering. Springer, 2005.
- [87] T. Zohdi, G. Holzapfel, and S. Berger. A phenomenological model for atherosclerotic plaque growth and rupture. *Journal of Theoretical Biology*, 227(3):437 – 443, 2004.

Index

- anisotropic materials, 50
- arbitrary Lagrangian-Eulerian, 62
- artificial diffusion term, 91

- balance of force, 51
- biharmonic equation, 71
- body forces, 23
- Brownian motion, 34

- Cauchy stress tensor, 23
- conservation equation of mass, 23
- conservation equations, 22
- conservation equations of momentum, 24
- continuity of velocity, 51
- convection, 34
- convection-diffusion equation, 34
- Crank-Nicolson scheme, 88
- current configuration, 18

- deformation, 18
- deformation gradient, 19
- density, 22
- differential elements, 32
- differential form, 32
- diffusion, 34
- diffusion coefficient, 34
- Dirichlet boundary conditions, 51
- displacement, 18
- do nothing boundary conditions, 52
- dynamic viscosity, 25

- elastic, 38
- endothelial cells, 6
- energy estimate, 76
- Eulerian, 18
- explicit forward Euler scheme, 88

- fibrous cap, 8
- finite element mesh, 89
- first Piola-Kirchhoff stress tensor, 29
- flow patterns, 6
- fluid dynamics, 18
- fluid-structure interaction problem, 16
- foam cells, 8

- Galerkin finite element method, 89
- Gascoigne, 93
- generic particles, 40
- Green-Lagrange tensor, 78
- growth function, 27
- growth matrix, 41

- hanging nodes, 90
- harmonic extension, 70
- high density lipoproteins, 8
- homogeneous, 38
- hydrostatic pressure, 25
- hyperelastic, 43

- implicit backward Euler scheme, 88
- incompressibility constraint, 24
- incompressible flow, 24
- incompressible Mooney-Rivlin material, 48
- incompressible neo-Hookean material, 48
- indeterminate Lagrange multiplier, 47
- inf-sup condition, 90
- isothermal conditions, 24
- isotropy, 44

- kinematic viscosity, 26
- kinematics, 18

- Lagrangian, 18
- Lebesgue space, 58
- left Cauchy-Green tensor, 44
- linear elastic equation, 72
- lipid core, 8
- low-density lipoproteins, 6

- macrophages, 7
- material derivative, 19
- metric of growth, 43
- monocytes, 6

- natural configuration, 40
- natural state, 40
- Navier-Stokes equations, 26
- Neumann boundary conditions, 52

Newton method, 92
non-dimensional form, 55
non-Newtonian fluid, 26

objectivity, 44
one-step- θ scheme, 88
orientation preserving, 20

ParaView, 94
permeability, 51
Piola transformation, 29
polynomial functions, 89
principal invariants, 45

reaction function, 36
reference configuration, 18
Reynolds transport theorem, 21
right Cauchy-Green tensor, 44
Rothe's method, 88

second Piola-Kirchhoff stress tensor,
33
shear modulus, 48
shear rate, 35
Sobolev space, 58
stored energy function, 43
strain rate tensor, 26
structural mechanics, 18
surface forces, 23

thrombus, 10
transmission conditions, 51

velocity, 18